Msc Thesis Report

Heat Management and Performance Increase of an Engine Cycle Using Liquid Hydrogen in Aircraft

Haroun Saâïd

Delft University of Technology

Heat management and performance increase of an engine cycle using liquid hydrogen in aircraft

Master thesis

Version 1.1
Publication Date: December 13, 2024

by

Haroun Saâïd

To obtain the degree of

Master of Science
in Aerospace Engineering

At the Delft University of Technology

To be defended on: 16-12-2024

Student number: 4292154
Supervisor: Dr.-Ing. Alexander Heidebrecht
Thesis Committee: A. Heidebrecht, F. Yin, C. Falsetti

TU Delft

Preface

This thesis delineates my thesis as part of my graduation for the Master of Science in Aerospace Engineering. This graduation project has taught me to be critical of my own work and how to research independently. I enjoyed studying at the Delft University of Technology and loved learning about new ideas and problem solving. I learned that succeeding courses and projects that are commonly described as 'difficult' are in fact easy, or at least achievable when you decide to set your mind to it completely. Nevertheless, my time at the Delft University of Technology hasn't always been the easiest; personal struggles, and other occupations such as pursuing a secondary study and taking on a job in education all while conducting research for this thesis have effectively delayed the closure of this project.

First and foremost, I want to thank God Almighty, without Whose Will, nothing is possible. Secondly, I want to thank my family who have been supporting me financially and with my health. Thirdly, I want to thank Dr.-Ing Alexander Heidebrecht for his patience, advice and input.

I want to conclude by saying to any student who might read this: if you don't necessarily need to use Dymola in your project, please find an alternative, as the resources are very limited as well as the experts that might help you. I furthermore hope that my research can be built upon by other researchers and students such that we can develop a world that is more sustainable and in which people can live in comfort and well-being.

Executive Summary

As the climate is changing, and people are becoming more aware of the consequences or pollutant emissions, there is a higher demand for more efficient and less polluting aircraft. There have been proposals to design aircraft that fully work on cryogenic hydrogen, but this requires a radical new design, which is both costly and time consuming. As an intermediate step, efforts are made to design semi-radical aircraft, in which certain components of an existing design are changed, which subsequently would be less time consuming and thus could be able to enter into service in the near future.
The A321 APPU (which is a modification of the A321neo) is such a concept, in which the auxiliary power unit (APU) of the A321neo is replaced by a novel hydrogen powered turboshaft system that includes a propulsor and boundary-layer-ingestion (BLI) to alleviate the main engines, named the 'Auxiliary Power and Propulsion Unit' (APPU). The hydrogen is stored in cryogenic form in a separate tank. The boundary-layer-ingestion propulsor is able to alleviate the main engine by 14.5%, resulting into less fuel being burnt in the main engine and reducing the amount of CO_2 emissions by 13.1%.

As in most aircraft, certain parts of the engine system are in need of cooling, most notably the HPT blades. Concurrently, the onboard cryogenic hydrogen needs to be heated up before entering the combustor to avoid high thermal stresses. The cryogenic hydrogen can be used to cool these parts, while at the same time reaching a more appropriate temperature before entering the combustor. Alleviating conventional cooling methods by making use of the cryogenic hydrogen increases the thermal efficiency of the engine system. Moreover, increasing the temperature of the fuel increases the LHV, which increases the thermal efficiency of the engine system even further.

Three different cases are analysed: firstly, the cryogenic hydrogen is used to cool the bleed air, by which less bleed air is required, increasing the core flow, which increases the thermal efficiency of the cycle. Secondly, using the same principle, the TIT is increased, while the amount of (now cooled) bleed air stays constant to the baseline. In this case the thermal efficiency increases mainly due to the higher LHV of the fuel. Thirdly, the cryogenic hydrogen is used to intercool the core flow between the booster and the HPC, after which the pressure ratio is increased accordingly.

The engine cycle of the APPU is modelled in *Dymola*, a commercial software that uses Modelica, which is an object-oriented, declarative, multi-domain modelling language, which allows the user to model unconventional (engine) system models. The thermophysical properties of hydrogen are simulated using the ExternalMedia library, which is a library that enables Modelica models to interface with external software for fluid property calculations, such as Coolprop, which is written in C++. Another commercial software, *GasTurb*, is used as a means of verification of the Dymola model.
Models are developed to simulate the APPU engine's performance using heat exchangers to intercool and to cool the bleed air or the core flow. The pressure loss that the heat exchanger induces is taken into account for the intercooling model.

The APPU is simulated in cruise and in take-off. The kerosene driven baseline APPU model shows a thermal efficiency of efficiency of 48.3 % at cruise. If the APPU is driven by hydrogen the thermal efficiency is observed to increase to 49.8 % at cruise. Cooling the bleed air down to a temperature of 273.5 K, the required bleed flow decreases with 37 %, and increases the fuel temperature from 20 K to 84 K, increasing the thermal efficiency to 49.9 %. Cooling the bleed air to 273.5 K, while keeping the amount of bleed air constant, allows the TIT to be increased from 1700 K to 1840 K, and increases the temperature of the fuel from 20 K to 120 K, while keeping the rest of the engine cycle constant. This results into an increases thermal efficiency of 50.7 %. It is found that intercooling and increasing the pressure ratio of both compressors to 8, increases the thermal efficiency by 3.7%, from the baseline value of 49.8% to 53.5%. Performance complications due to increasing the OPR to 64 have not been analysed into great detail and might make this result hard to achieve in reality.
The estimated mass of the APPU is 502 kg. The additional mass of the heat exchanger in the case of decreasing the bleed flow is estimated to be 2.2 kg, or 0.4 % of the APPU's total mass. While the additional mass of the heat exchanger when keeping the bleed flow constant is estimated to be 3.7 kg, which translates to an increase of a mere 0.7 % of the APPU's total mass. The intercooling system needs to cool the largest amount of mass flow, resulting the heat exchanger to increase in size and a mass of 22.0 kg, increasing the APPU mass by 4.4%.

It is concluded that the largest contributor to the thermal efficiency is the LHV of the hydrogen. This means that any process in which the hydrogen extracts the most amount of heat is most advantageous, efficiency-wise. Further-

more, it is concluded that adding intercooling and subsequently increasing the pressure ratio increases the thermal efficiency more than cooling and reducing the bleed flow.

The current *Dymola* model does not incorporate the effect of the pressure drop of the heat exchanger during bleed cooling, nor does it simulate the amount of NO_x that is being produced. Recommendation for future work include the effect of pressure drop of the bleed heat exchanger on the system performance, as well as including the effects of using recuperating the nozzle waste heat into the fuel. Furthermore an additional bottoming cycle, in which the hydrogen is expanded over an extra turbine should be investigated.

Contents

Nomenclature

Abbreviations

Abbreviation	Definition
APU	Auxiliary Power Unit
APPU	Auxiliary Power and Propulsion Unit
CFD	Computational Fluid Dynamics
CMSX	Creep-Microscopically Stable Experimental
DAE	Differential-Algebraic System of Equations
gg	Gas generator
HPC	High Pressure Compressor
HPT	High Pressure Turbine
IBC	Inverted Brayton Cycle
IPT	Intermediate Pressure Turbine
LPC	Low Pressure Compressor
LPT	Low Pressure Turbine
ISA	International Standard Atmosphere
MM	Molar Mass
MTOM	Maximum Take-off Weight
MTOW	Maximum Take-off Weight
ODE	Ordinary Differential Equation
OEW	Operational Empty Weight
OPR	Overall Pressure Ratio
ORC	Organic Rankine Cycle
PSFC	Power Specific Fuel Consumption
SBC	Simple Bleed Cooling
SC	Supercritical
SFC	Specific Fuel Consumption
TC	Transcritical
TIT	Turbine Inlet Temperature
TSFC	Thrust Specific Fuel Consumption

Symbols

Symbol	Definition	Unit
A_c	Cross-sectional area	$[m^2]$
c_p	Specific heat capacity at constant pressure	$[\frac{J}{kg \cdot K}]$
e	Specific energy	[J/kg]
f_{id}	Portion of regenerative flow	[kg/s]
h	Specific enthalpy	[J/kg]
h_c	Convective heat transfer coefficient	$[\frac{W}{m^2 \cdot K}]$
k	Thermal conductivity	$[\frac{W}{m \cdot K}]$
L	Length	[m]
$\dot{m}$	Mass flow	[kg/s]
P	Pressure	[Pa]
Pa	Prandtl number	[-]
Q	Heat	[J]
$\dot{Q}$	Heat flow	[J/s]
q	Specific heat	[J/kg]
S	Entropy	[J/K]
T	Temperature	[K]

Symbol	Definition	Unit
t	Time	[t]
V	Velocity	[m/s]
V	Volume	[m^3]
w	Specific work	[J/kg]
w_i	Mass fraction	[kg/s]
$\mathbf{X}$	Composition	[kg/kg]
x	Intercooler efficiency	[-]
β	Fin constant / Expansion ratio	[-]
η	Efficiency	[-]
γ	Specific heat ratio	[-]
∇	Nabla operator	N/A
ν	Kinematic viscosity	[m^2/s]
ω	Vorticity	[rad/s]
ρ	Density	[kg/m^3]
$\wp$	Fin circumference	[m]
ϕ	Compressor / Turbine mass flow	[kg/s]
Φ	Rotation angle	[rad]
ω	Angular velocity	[rad/s]

List of Figures

List of Tables

1

Introduction

From the period 1880-2012, the global averaged land and ocean surface temperature has increased by 0.85 °C, compared to 1850; furthermore, each of the past three decades (at the moment of the report) "has been successively warmer at the Earth's surface than any preceding decade since 1850"[18]. Although this value might initially seem small, its effects might have detrimental impact on the global climate. The impacts of the increasing temperature are many, one of which is the rise in sea level. IPCC reported that from the period 1901 to 2010, the mean rate of global averaged sea level rise was 1.7 mm/year, while during the period 1993 to 2010, the mean rate of global averaged sea level rise was 3.2 mm/year. This global sea level increase can potentially be dramatic for wildlife and human civilisation as well if no appropriate measures are to be taken.
The atmosphere temperature increases if the amount of heat that enters it is greater than the amount that leaves, this is called "radiative forcing". Amongst others, the composition of the atmosphere dictates the amount of solar radiation that is absorbed. The main drivers that cause radiative forcing are the four greenhouse gases: carbon dioxide, methane, nitrous oxide and halo carbons, while other greenhouse gases exist, these four are the main contributors [18]. The IPCC reports mentions that the radiative forcing in 2011 has increased by 2.3 W/m^2 compared to 1750.
As of 2021, the aviation sector is estimated contribute approximately 4% of the human-induced global warming [19]. Moreover, air traffic is expected to grow annually by 3.8 % for the coming 20 years, leading to an additional 4.2 billion passengers in 2043 [20]. European climate target state that the net emissions for transport should be decreased by 90% in 2050, compared to 1990 [21].
This means that the aviation industry has a big responsibility in making aircraft more efficient and less pollutant, this obviously gives rise to lots of challenges.

Efforts are being made to make aircraft, amongst others, aerodynamically more efficient and/or to be driven by renewable fuels. One of these efforts is the flying-V which has been proposed by the TU Delft, which is a blended-body-wing aircraft that merges the fuselage into a wing that results into a 10% higher L/D ratio [22]. However, creating an aircraft that has a radically different, such as an aircraft that works in its entirety on a different fuel, such as hydrogen, requires drastic changes in the fuel system, the tank storage and therefore the entire shape of the aircraft. This requires a large amount of time and money. Therefore, efforts are made on improving existing designs; as improving an existing design is less costly and lengthy than creating an entirely new aircraft. One of these efforts that are is the A321 APPU, which stands for Auxiliary Propulsion and Power Unit. This project is governed by the TU Delft, in which an existing design (Airbus A321 neo) is improved by changing APU and its coherent fuel system. Its two main engines will still be consuming kerosene, while the auxiliary power unit (APU) is replaced by a new engine that functions fully on hydrogen. This means that that the unit will emit no CO_2, CO, UHC or soot; NO_x however does continue to exist in the exhaust gas. Moreover, the APPU integrates Boundary Layer Ingestion (BLI) system and an open rotor propeller within the boundary layer ingestion regime [23], which results to additional thrust, relieving the main engines. Preliminary studies show that the CO_2 emission during a typical 2000 km flight is able to decrease by 20% [23]. The APPU will therefore be an important -transitional- step to a cleaner and more sustainable future.

Because a new type of fuel is used, the APPU must be optimised for its specific design. Currently, work is being done on the preliminary design of its components. One of such components is the cooling of the APPU. Although the existing cycle cools the APPU by means of bleed air, it doesn't make use of the heat sink of the liquid hydrogen on board. This heat sink offers great potential for efficient cooling and increasing the cycle efficiency as the liquid hydrogen is stored at 20 Kelvins. Coinciding with this, the liquid hydrogen needs to 1: be vaporised such that stable combustion can take place, and 2: be elevated to a temperature such that no large temperature gradients exist in the combustion chamber (which could lead to high thermal stresses, which is unwanted). Additionally, having a fuel flow of a too low temperature increases the amount of incomplete combustion, which yields amongst others, compounds such as hydrogen peroxide [24].

Some work has been done in comparing hydrogen fuelled aircraft with conventional aircraft on its and energy consumption and efficiency over different flight missions, as is the case in the study of Verstaete [25]. Another study that has been conducted is that of Balli et al. [26] in which they analyse the effects of hydrogen fuel on the exergetic performance of a turbojet engine. Balli et al. however, analyse an aircraft that fully works on hydrogen. Moreover, they don't take into account the heating of the hydrogen fuel prior to injecting it in the combustor.
This study however, focusses on the thermodynamics of the individual components of the engine, takes into account the effects that the temperature of the fuel has on the cycle efficiency as well as its implications on the main engine.

2

Research Goal & questions

2.1. Research goal

The main focus of this thesis is **to develop a dynamic performance calculation model of a hydrogen fuelled gas turbine engine that utilises the onboard heat sink to increase performance.** The model should be able to provide the work output and efficiencies under different operational parameters.

2.2. Research questions

The research questions that are used to achieve the research objective to fill the knowledge gap and its corresponding sub-questions are defined as follows:

1. What will be the best (least PSFC or highest η_{th}) hydrogen cooling system for the APPU?
   (a) How does the cooling system influence the efficiency of an engine?
   (b) What sort of heat exchangers can be used in cooling aero engines with cryogenic hydrogen?
2. How does the new system behave during a typical flight mission?
   (a) How much fuel does the altered engine burn during cruise?
3. What will be the increase in weight, and its consecutive increase in PSFC?
   (a) What should the sizing of the heat exchanger be in the new design?
   (b) What is the effect of adding a heat exchanger on the mass?

2.3. Hypotheses

Using the heat sinking capacity of the cryogenic hydrogen to cool the bleed air, decreases the amount of bleed air required, which increases the thermal efficiency and the specific thrust of the engine. Instead of reducing the required bleed, the turbine inlet temperature (TIT) could be increased, while keeping the same amount of (now cooled) bleed as the baseline. In another case, the cryogenic hydrogen can be used as a coolant for intercooling. This would reduce the work required to compress the airflow. If this would be combined with increasing the pressure, a higher thermal efficiency can be achieved. These three cases could be integrated in the design of the APPU, however, it is currently unknown to what extend this will improve the thermal efficiency and/or specific thrust. Moreover, the added weight (and volume) of adding components (heat exchangers) will have to be taken into account, as an increased surface area leads to more drag and increased weight means a higher fuel consumption. This research aims to fill the knowledge gap for the APPU specifically, and by extension for similar engines as well.

3

Thermodynamic Cycle Variations

Since the dawn of aviation, aircraft carry chemical energy in the form of (mostly) liquid fuel. This chemical energy has to be converted into work for the aircraft to execute its purpose, which is to propel forward. This conversion from chemical energy into work is effectuated by thermodynamic cycles. Jet engines work on the principle of the open Brayton cycle [27], as jet engines utilise the difference in momentum create thrust as means to propel itself. Brayton cycles are favoured in aircraft, because its applications have a high power to weight ratio. If the engine architecture is changed, by introducing heat sinks and heat exchangers for example, different thermodynamic cycles could be beneficial for the engine performance. In this section some of those thermodynamic cycles are explored, including some innovative methods.
The concept of an engine can be represented by the following relations; which is very fundamental. First of all, the work that is generated equals the difference between the input heat and the output heat, as represented in Equation 3.1 [1].

$$\dot{Q}_{in} - \dot{Q}_{out} - \dot{W} = 0 \tag{3.1}$$

Then, the created entropy can be calculated by taking the difference in the entropy that leaves the system and the entropy that enters the system.

$$\dot{S}_{in} - \dot{S}_{out} - \dot{S}_{gen} = 0 \tag{3.2}$$

The entropy is calculated by Equation 3

$$\dot{S}_{in} = \frac{\dot{Q}_{in}}{T_H} \tag{3.3}$$

$$\dot{S}_{out} = \frac{\dot{Q}_{out}}{T_0} \tag{3.4}$$

The ratio of outgoing and incoming heat becomes then after combining resolving:

$$\frac{\dot{Q}_{out}}{\dot{Q}_{in}} = T_0\left(\frac{1}{T_H} + \frac{\dot{S}_{gen}}{\dot{Q}_{in}}\right) \tag{3.5}$$

Then, the efficiency is defined as the ratio between the obtainable work divided by the input heat, which is shown by Equation 3.6 [1].

$$\eta = \frac{\dot{W}}{\dot{Q}} = 1 - \frac{Q_{out}}{Q_{in}} \tag{3.6}$$

Combining Equation 3.6 with Equation 3.5, gives Equation 3.7.

$$\eta = 1 - \frac{\dot{Q}_{out}}{\dot{Q}_{in}} = T_0\left(\frac{1}{T_H} + \frac{\dot{S}_{gen}}{\dot{Q}_{in}}\right) \tag{3.7}$$

When the generated entropy equals zero (implying that the cycle is completely reversible), Equation 3.7 resolves to Equation 3.8.

$$\eta = 1 - \frac{T_0}{T_H} \tag{3.8}$$

Equation 3.8 is referred to as the 'Carnot efficiency'; the maximum achievable efficiency typical to the Carnot cycle.

3.1. Brayton

An open Brayton cycle is mostly used in gas turbines and aero-engines. An ideal Brayton cycle consists out of isentropic compression, followed by isobaric heat addition, followed by an isentropic expansion. In the case of a closed Brayton cycle, an isobaric heat rejection is added. Its efficiency can easily be calculated using Equation 3.9 [1] (when the assumption is made that the temperature and the specific heat capacities are constant).

$$\eta_{thmd} = \frac{w_{net}}{q_{in}} = 1 - \frac{q_{out}}{q_{in}} = 1 - \frac{c_p(T_4 - T_1)}{c_p(T_3 - T_2)} = 1 - \frac{T_1(T_4/T_1 - 1)}{T_2(T_3/T_2 - 1)} \tag{3.9}$$

In which 1, indicates the state of the fluid before compression, 2 the state of the fluid after compression, 3 the state of the fluid after heat addition, and 4 the state of the fluid after expansion. The P-V and the T-s diagrams can be observed in Figure 3.1, for reference. This can be represented as a function of pressure ratios and the heat capacity ratio, due to the process being isentropic.

$$\frac{T_2}{T_1} = \left(\frac{P_2}{P_1}\right)^{\frac{\gamma-1}{\gamma}} = \left(\frac{P_3}{P_4}\right)^{\frac{\gamma-1}{\gamma}} = \frac{T_3}{T_4} \tag{3.10}$$

Substituting Equation 3.10 into Equation 3.9 (as $\frac{T_4}{T_1} = \frac{T_3}{T_2}$) leads to

$$\eta = 1 - \frac{T_1(T_3/T_2 - 1)}{T_2(T_3/T_2 - 1)} \tag{3.11}$$

which gives a simple equation for the ideal efficiency of the Brayton cycle:

$$\eta_{th} = 1 - \frac{1}{\beta^{\frac{\gamma-1}{\gamma}}} \tag{3.12}$$

with β being the pressure ratio $\frac{P_2}{P_1}$. As can be seen from Equation 3.12, the thermal efficiency increases with an increase in pressure ratio.
This however doesn't mean that the highest amount of work is extracted at the highest possible pressure ratio. For this, a new variable 'specific work' (Equation 3.13, where the subscript 'gg' indicates the 'gas generator') is introduced, which defines the amount of net work per mass flow. If the pressure ratio increases, the amount of net work that can be extracted will increase, then reaches an optimum, and then decreases, this can be observed in Figure 3.2. The optimal pressure ratio is defined as the pressure ratio that induces the highest specific work, for a specified temperature ratio. Furthermore, it can be observed that increasing the temperature ratio does not change the thermal efficiency, contrary to the pressure ratio.

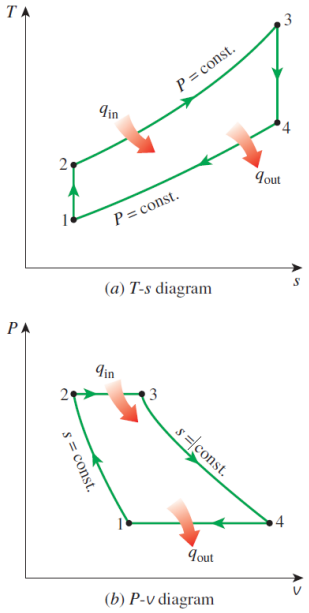

Figure 3.1: T-s and P-V diagrams for ideal Brayton cycle [1]

Summing up, this means that a more efficient system can be built, alluding that the cycle needs more mass flow input to achieve a specified amount of net work. This then, would mean in physical terms that the actual system has to become larger and thus heavier, which could be agreed upon for stationary ground gas turbines, but as weight is an important factor in aero-engines, a trade-off has te be made whether in increase of thermal efficiency at the cost of an increased engine mass has to be made.

$$W_{s,gg} = c_p(T_{gg} - T_5) = c_p T_4\left(1 - \frac{1}{\beta^{\frac{\gamma-1}{\gamma}}}\right) - c_p T_2\left(\beta^{\frac{\gamma-1}{\gamma}} - 1\right) \tag{3.13}$$

$$\frac{W_{s,gg}}{c_p T_2} = \frac{T_4}{T_2}\left[1 - \left(\frac{1}{\beta^{\frac{\gamma-1}{\gamma}}}\right)\right] - \left[\beta^{\frac{\gamma-1}{\gamma}} - 1\right] \tag{3.14}$$

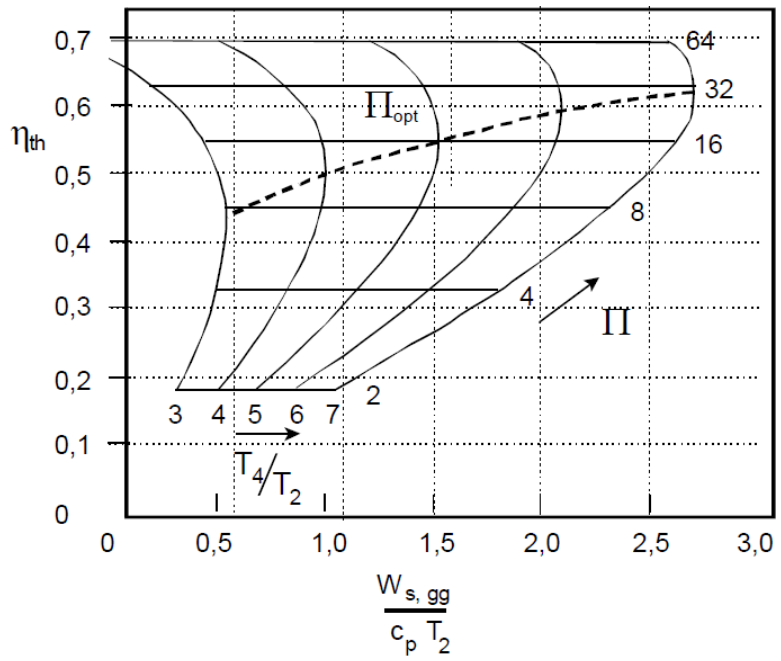

Figure 3.2: Performance graph of a generic ideal Brayton cycle (Π indicates the pressure ratio) [2]

3.1.1. Recuperation

Recuperation (or regeneration) is when the temperature of the exhaust gas is used to increase the temperature after last compressor stage. This means that the input heat that is taken from on external source can be decreased, therewith the cycle's thermodynamic efficiency can be increased. This principle can only be applied if the exhaust temperature is higher than the compressed working fluid temperature. The saved heat would then be as mentioned in Equation 3.15.

$$q_{recup} = h_5 - h_2 \tag{3.15}$$

Where h_5 is the enthalpy of the gas at the recuperator, right after the last turbine stage and h_2 being the enthalpy of the

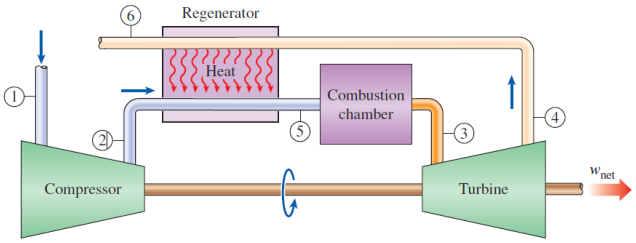

Figure 3.3: Gas turbine with recuperation [1]

gas right after the compression, as can be observed in Figure 3.3. The maximum input heat saved due to recuperation occurs when the recuperator attains the temperature of the exhaust gas at the end of the nozzle. This is shown in Equation 3.16

$$q_{recup,max} = h_{5'} - h_2 = h_4 - h_2$$

The recuperator effectiveness can then be defined as the ratio between the actual input heat saved over the maximum possible input heat saved, as described in Equation 3.17.

$$\epsilon = \frac{q_{recup,act}}{q_{recup,max}} = \frac{h_5 - h_2}{h_4 - h_2} \tag{3.17}$$

A higher effectiveness can be achieved by using a larger recuperator, but this comes at the cost of a heavier system, which is not desirable in aircraft systems. Most recuperators have an effectiveness below 0.85 [1]. If the assumption is made that c_p stays constant, the efficiency of the Brayton cycle can be defined as Equation 3.18 [1].

$$\eta_{thmd} = 1 - \frac{T_1}{T_3}\beta^{\frac{\gamma-1}{\gamma}} \tag{3.18}$$

Plotting Equation 3.18, together with Equation 3.12, gives Figure 3.5.

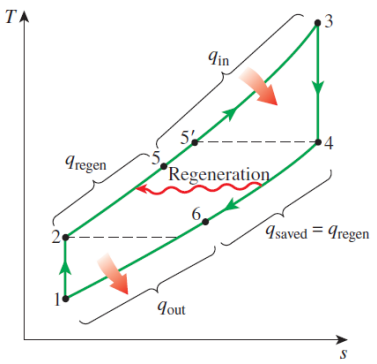

Figure 3.4: T-s diagram of a recuperating Brayton cycle [1]

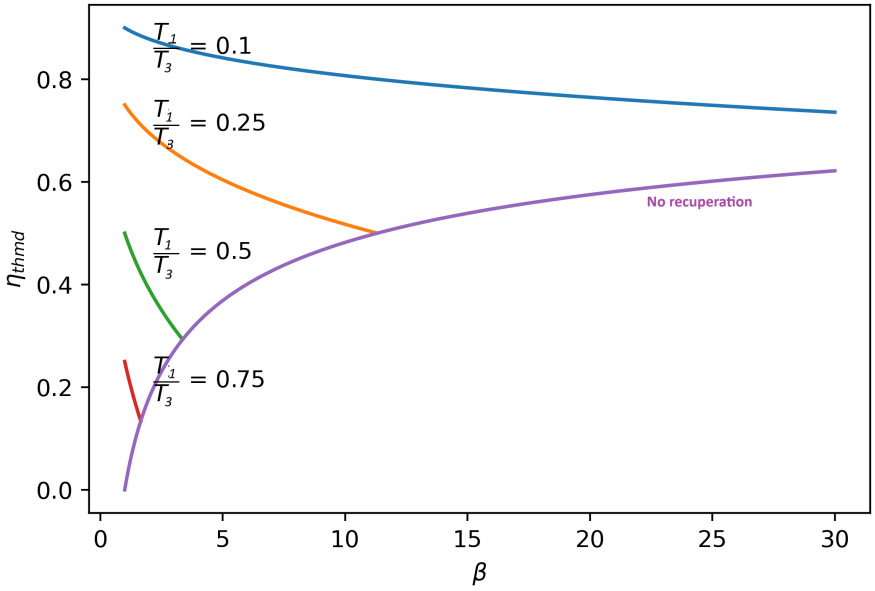

Figure 3.5: The thermodynamic efficiency of a Brayton cycle with recuperation (own work)

As can be seen from the plot, recuperation doesn't always contribute to a larger thermodynamic efficiency. The effect of the recuperator is largest when the temperature ratio of post-compressor to pre-turbine is largest. If the turbine inlet temperature is fixed, this temperature ratio can be increased if the temperature working fluid after the compression is lower. This can be achieved if inter-cooling is used.

3.1.2. Intercooling

Inter-cooling is a concept applied in thermodynamic cycles, to increase the thermodynamic efficiency by decreasing the work needed by the compressor to compress the working fluid (a decrease in the 'back-work ratio', which is defined in Equation 3.19).

$$r_{bw} = \frac{w_{comp,in}}{w_{turb,out}} \tag{3.19}$$

By cooling the working fluid, the volume decreases, which results into less work to compress it to a specified pressure. A typical T-s diagram of a Brayton cycle including an intercooler can be observed in Figure 3.6.

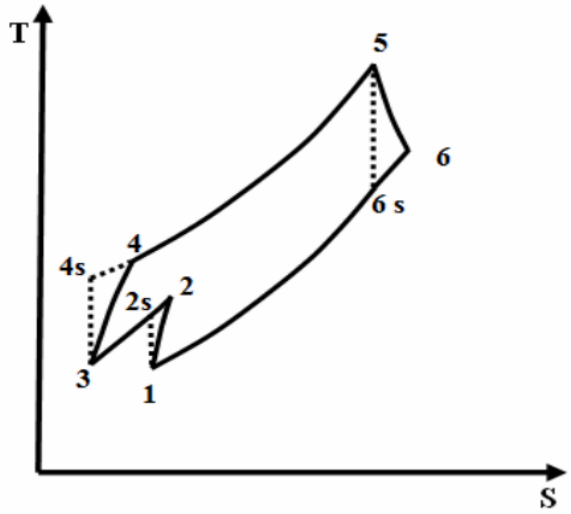

Figure 3.6: T-s diagram of a Brayton cycle with an intercooler [3]

Using an intercooler means that less work is needed to compress the air to the combustor inlet pressure, this means that the engine is left with more net specific work ($w_{net} = w_{turbine} - w_{compressor}$). This surplus of work can be used to increase the difference in momentum, leading to an increased thrust coefficient. However, because the air enters the

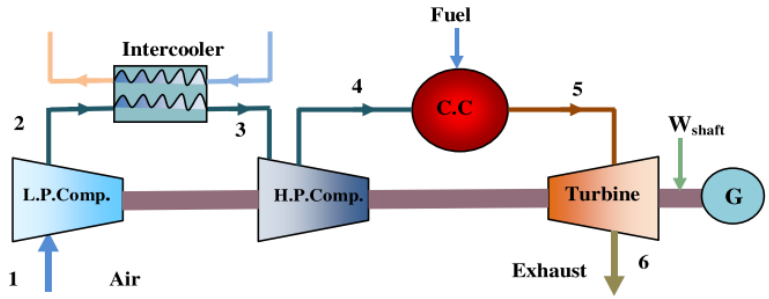

Figure 3.7: Schematic of a Brayton engine with an intercooler connected to a generator [3]

combustor at a lower temperature, Δ T ($\Delta T = TIT - T_{HPC,L}$) has to be higher, which means increasing q_{in}. Looking again at Equation 3.6, this means that the thermal efficiency of the cycle will decrease.
If there is however, no desire to increase the thrust coefficient, nor is there a desire to implement a perhaps heavy recuperator to increase the cycle efficiency, using an intercooler can still provide benefits. The intercooler causes the fluid to have a lower temperature within the HPC (and ultimately before entering the combustion chamber), this means that, if the temperature of the fluid is desired to be kept constant to the initial case, the pressure ratio of the HPC can be larger. This *would* result in an increase in thermal efficiency. Increasing the pressure ratio of a compressor however, could lead to a few issues:

- If there is a higher pressure gradient, the flow will be more susceptible to flow separation and surge. This results to total pressure loss.
- If the spool speed is increased too much, the absolute velocity at the blade tip can get trans- or supersonic. This may lead to unwanted shockwaves and total pressure loss.
- If the absolute velocity is higher, the boundary layer will be thinner, meaning the presence of a steeper velocity gradient, which leads to more friction losses.

This means that increasing the pressure ratio of an axial compressor will decrease the polytropic efficiency and subsequently the isentropic efficiency of the compressor. Furthermore, the isentropic efficiency decreases with the increase of pressure ratio, even if the polytropic efficiency stays constant, as a pressure increment at higher pressures needs more work than the same increment at lower pressures. Dixon [4] derives the overall isentropic efficiency as a function of the pressure ratio, as can be observed in Equation 3.20, in which η_p is the polytropic efficiency.

$$\eta_c = \left[\left(\frac{p_2}{p_1}\right)^{(\gamma-1)/\gamma} - 1\right] / \left[\left(\frac{p_2}{p_1}\right)^{(\gamma-1)/\eta_p\gamma} - 1\right] \tag{3.20}$$

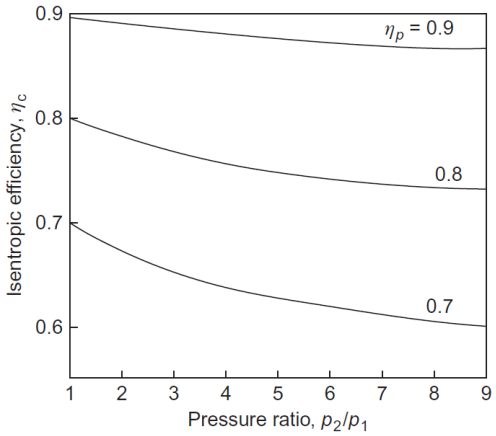

Figure 3.8: Relationship between the isentropic efficiency, pressure ratio and polytropic efficiency for a compressor with $\gamma = 1.4$ [4]

As can be seen in Figure 3.8, the isentropic efficiency decreases with the pressure ratio if the polytropic efficiency stays constant. Wettstein [6] provides an empirical functions for the polytropic efficiency as a function of pressure ratio in both optimistic and conservative scenarios. These functions have been extrapolated as can be seen in Figure 3.10. Using Equation 3.20 and Figure 3.10, a new isentropic efficiency can be calculated as indication of the behaviour in an intercooler.

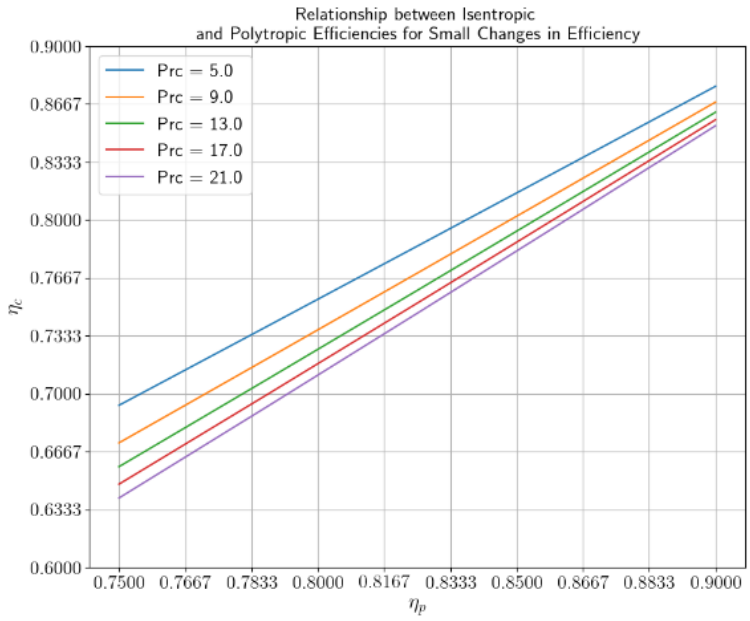

Figure 3.9: Relationship between polytropic- and isentropic efficiency at different pressure ratios[5]

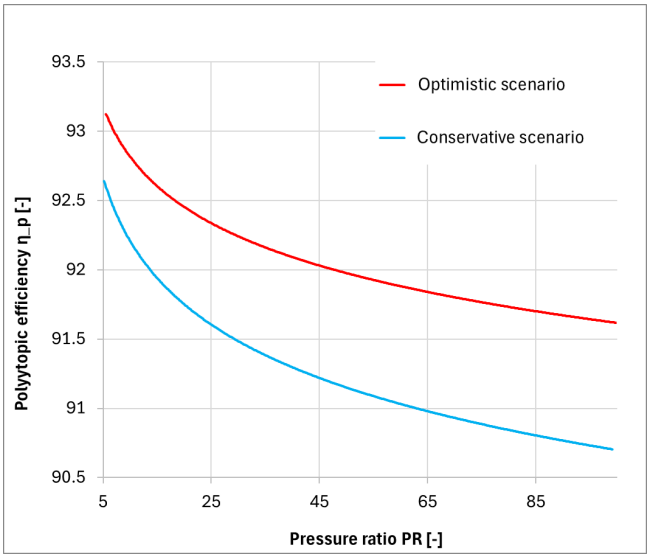

Figure 3.10: Relationship between the pressure ratio and polytropic efficiency of an axial compressor, adapted from Wettstein [6]

If instead of placing a single intercooler between the LPC and the HPC, multiple, smaller intercoolers are added between each compression stage, then the cycle will approach the path of an isothermic compression, as is the case with the Ericsson cycle. A T-s diagram of such a cycle can be observed in Figure 3.11. In such a case, the thermal efficiency approaches the Carnot efficiency. To further increase the cycle's thermodynamic efficiency, a recuperator will have to be added to provide the extra heat without using an external (fuel) source.

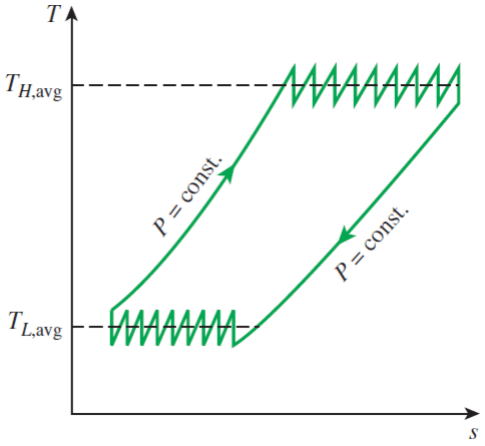

Figure 3.11: Intercooling after multiple compression stages approaches the T-s diagram of an Ericsson cycle[1]

3.1.3. Inverted Brayton cycle

A relatively novel concept within the realm of thermodynamics is the so called 'Inverted Brayton Cycle' or IBC. The IBC has been proposed as a means to recover work from waste heat, by several researchers [28] [7]. The IBC has an opposite flow direction compared to the Brayton cycles, whereas in the IBC the working fluid starts out with an atmospheric pressure (not necessarily an atmospheric temperature) and expands through a turbine, creating work, after which the flow achieves a sub-atmospheric pressure and is being cooled by means of a heat exchanger. Subsequently, the flow is compressed back to atmospheric pressure by means of the compressor, that is driven by the turbine. The compressor allows the existence of a sub-atmospheric pressure after the turbine. The function of the heat exchanger is to cool the air down such that the compression needs less work, leaving the cycle with net work.

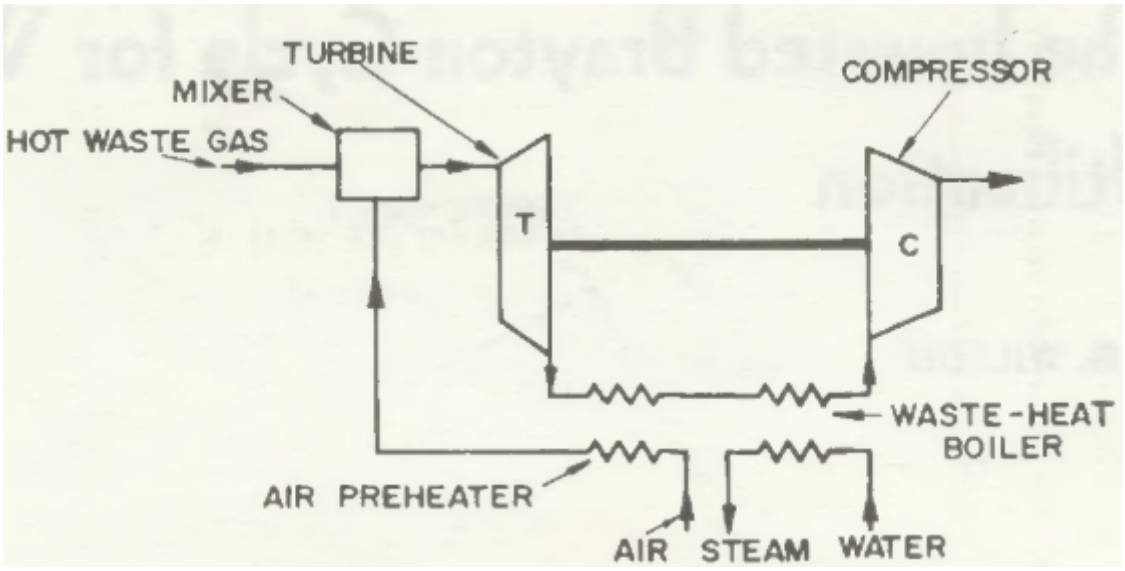

Figure 3.12: Generalised Inverted Brayton cycle [7]

This cycle offers the opportunity to extract from waste heat from the system, much like a recuperator does. If the IBC is used as a bottoming cycle, the thermal efficiency of the entire system will increase. The advantage of an IBC over other bottoming cycles, lie in the simplicity and the availability of the turbomachinery components [29]. A parametric investigation has been done by De Pascal et al. [30] concerning the efficiency and specific work output of different bottoming cycles: ORC and IBC. They compared the bottoming cycle efficiencies at a fixed cooling air temperature of $T = 15°C$, and a variable hot turbine inlet temperatures over a range of $130°C$ to $500\ °C$. The ORC offered a bottoming cycle efficiency between 6% and 24%, while the IBC offered a bottoming cycle efficiency between 4% and 12%. They concluded that "The innovative and not yet developed IBC system is a promising solution but not as performing as the ORC technology, especially in the field of very low temperatures (200–400 °C). If instead heat fluxes are available at temperature values above 350–400 °C, the IBC technology becomes more interesting in terms of achievable efficiency."[30]
However, using this solution in aviation might give rise to some challenges: The components, especially the turbine and the compressor have to be much larger than in a conventional (high pressure) system, as expanding a relatively low pressure fluid to an even lower pressure, infers a larger volume.

3.2. The Rankine cycle

Another thermodynamic cycle is the Rankine cycle, in which the compression and expansion are (ideally) isentropic, and the heat addition and rejection are both isobaric; identically to the Brayton cycle. The difference being that the Rankine cycle uses heat to increase the temperature of the working fluid *and* to induce phase change. A schematic, including a H-s and a T-s diagram is shown in Figure 3.13. Firstly, the liquid is pumped to a higher pressure P_2 (which will be the maximum pressure in the cycle), which doesn't decrease its volume too much, as in this state, a liquid can be considered incompressible (constant density). Secondly, the liquid is heated up (by for example an economiser) at a constant pressure to increase its temperature to T_3 (which equals the evaporation temperature T_E), such that its volume increases. Subsequently the liquid is heated further until the liquid is completely vaporised and a saturated gas is obtained (this is point 4). If the cycle contains a superheating phase, the gas is heated even further to T_5. Lastly, this gas is expanded (isentropically in an ideal case) to a temperature and pressure of T_6 and P_6 and condenses, having returned to its initial condition. In isentropic compression, the *liquid* undergoes a temperature increase that can be calculated via Equation 3.21 [8]. This relation is different than in the Brayton cycle, as the fluid in the Brayton cycle if often times assumed as an ideal gas, whereas the fluid in a Rankine cycle is a liquid. If the fluid is assumed to be incompressible however, Equation 3.21 reduces to zero.

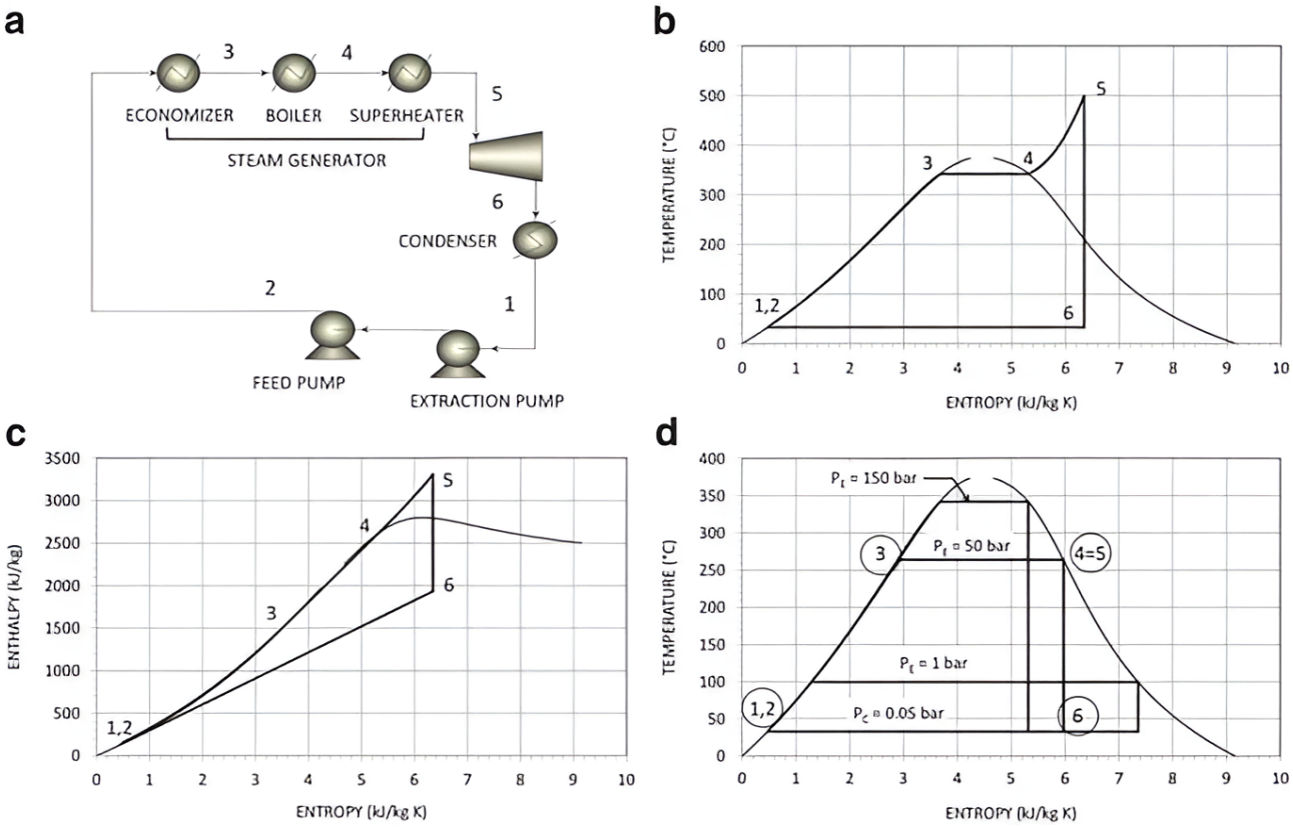

Figure 3.13: Reversible Rankine cycle a) Schematic b) T-s diagram with superheating c) H-s diagram d) T-s diagram showing different cycles for different evaporation pressures [8]

$$\left(\frac{\delta T}{\delta P}\right)_S = -\frac{T}{\rho^2 c_p}\left(\frac{\delta \rho}{\delta T}\right)_P \tag{3.21}$$

3.3. Stirling and Ericsson

Stirling cycles and Ericsson cycles are both thermodynamic cycles that have not been explored into the same depth as other cycles, such as the Brayton cycle. A Stirling cycle is a thermodynamic cycle that entails isothermal compression, followed by a isochoric heat addition, followed by an isothermal expansion and lastly another isochoric heat extraction. The Ericsson cycle is similar to that of the Stirling cycle, but it differs in the method of heat addition/extraction; whereas the heat addition/extraction in the Stirling cycle is isochoric, the Ericsson cycle undergoes isobaric heat addition/extraction. This subtle difference however, causes a drastic change in performance between the two cycles for different situations. In 2018, Costa and MacDonald [31] made a generic comparison between the net work output of a Stirling- and an Ericsson cycle for various situations. The research was done by initially creating the both cycles with an equal amount of net work. Hereafter a parameter was varied and both cycles were analysed which one produced a greater net output. The analysis was done for three different scenarios:

- Equal mass and temperature limits (in which the pressure/volume was variable).
- Equal mass and pressure/volume limits (in which the temperature was variable).
- Equal temperature and pressure/volume limits (in which the mass flow was variable).

In short the results demonstrated that the Stirling cycle produced more net work output at higher pressures and lower volumes, while the Ericsson cycle produced more net work output at lower pressures and higher volumes.

3.4. Direct expansion

In literature, when talking about regasification, Direct expansion is often used as baseline. The term Direct expansion (or DEX for short) is basically an open Rankine cycle in which the working medium is the fluid that needs to be gasified. This Direct expansion is the simplest method of regasifying the liquid in which the liquid's pressure is first elevated (by means of pumping), after which its temperature is elevated (by means of heating), after which the now gas is expanded to a desired pressure. The maximum amount of useful work that can be extracted from a medium is called 'exergy'. Thus the amount of exergy gives a good indication of the potential of a medium. The amount of exergy can be divided into 'thermal exergy' and 'pressure exergy'. This method of Direct expansion recovers the pressure exergy.

$$e(T,P) = e_{th} + e_p \tag{3.22}$$

with

$$e_{th} = e(T,P) - e(T_0,P) \tag{3.23}$$

$$e_p = e(T_0,P) - e(T_0,P_0) \tag{3.24}$$

where T_0 is a reference temperature of 298 K and P_0 is a reference temperature of 1 bar [32]. A schematic can be observed in Figure 3.14 and a T-s diagram can be observed in **??**.

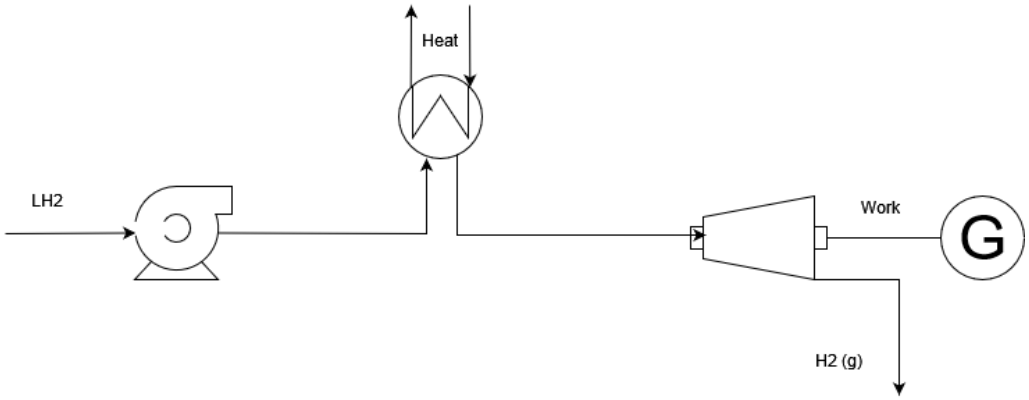

Figure 3.14: Schematic of Direct expansion (own work)

3.5. Using recirculated flow

An innovative method that has been proposed by Laouir [9]. He addresses the use of the very low temperature of the liquid hydrogen to generate mechanical energy, hereby increasing the thermodynamic efficiency. For comparison the method of Direct Expansion (DEx) is used as baseline.
The ideal process of regasification is described by Equation 3.25. In which the assumption is made of isentropic compression, followed by an isothermal expansion, absorbing heat from its surroundings, thus obtaining hydrogen gas in an ideal manner.

$$W_{id} = (h_g - h_l) - T_0(s_g - s_l) \tag{3.25}$$

Indicating that the ideal work that can be extracted from the regasification is the gain of enthalpy during the phase change, minus the loss due to the entropy increase. The second term on the right hand indicates the heat Q_0 that is needed for the phase change. The T-s diagram of the ideal work can be shown in Figure 3.15. For this analysis, a para-hydrogen fluid was assumed. The amount of work that ideally can be extracted through this cycle is shown in Figure 3.16. This indicates that theoretically, the hydrogen has its highest potential at low pressures and high temperatures.

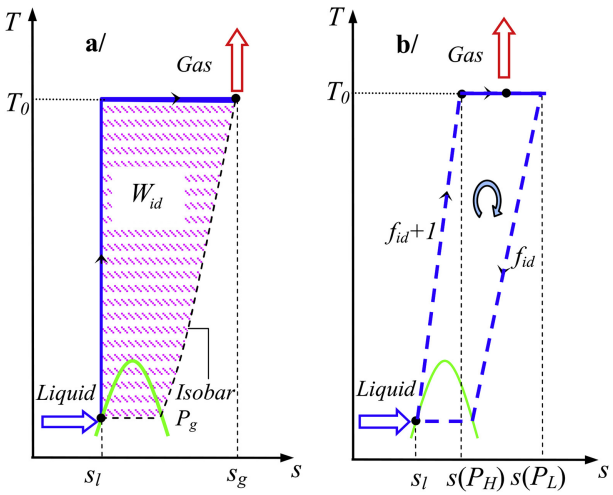

Figure 3.15: T-s Diagram of ideal work that can be extracted [9]

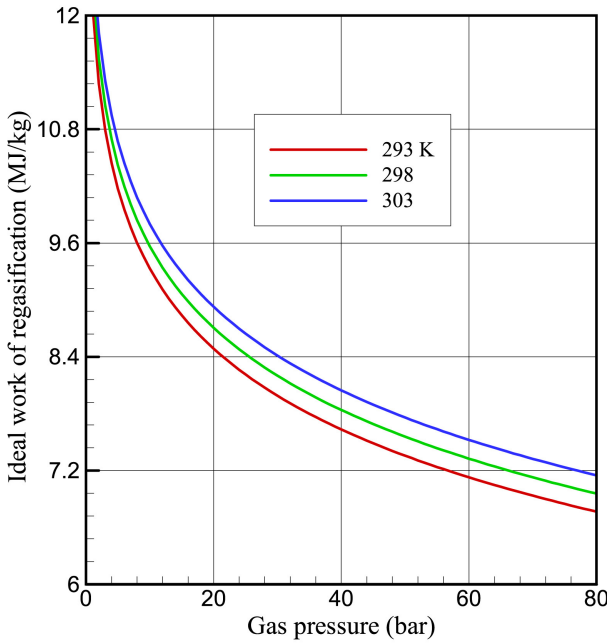

Figure 3.16: Visualisation of the ideal work that can be achieved regasifying the LH2 [9]

The ideal case of DEx as shown in Figure 3.15 is considered very hard to achieve in reality, as there has to be a significant temperature increase of the *liquid* hydrogen due to its compression, which translates to an immense amount of pressure increase. Laouir suggests a novel and complex approach using multiple stages of compression, heating, expansion and recirculation to increase the amount of work that can be extracted. A comparison between the T-s diagrams of the DEx case and the concept that Laouir suggests can be observed in **??**.

4

Heat Exchangers

The Airbus 321 Neo APPU carries a considerable amount of cryogenic hydrogen to be used as fuel for the APPU. This cryogenic fluid has to be heated up and vaporised to be used as fuel within the combustor. The required amount of heat can be extracted from multiple stations within the engine cycle. Furthermore, the heat sink of the cryogenic hydrogen can be used to cool down the bleed air or to introduce a intercooler between the compressors. This requires to usage of heat exchangers. Heat exchangers come in different shapes and forms, together with its own additional weight and total pressure drop, both of which are important parameters considering that an increase in aircraft weight increases the fuel consumption and a pressure drop decreases the engine performance.
This section aims to lay out the different types of heat exchangers, its associated weight and sizing such that an appropriate estimations can be made for future calculations. Furthermore, this section aims to obtain reasonable parameters for common heat exchangers in aircraft. How much of a pressure drop is acceptable? What are reasonable heat transfer coefficients? What is plausible relation between the increase in structural mass and the fuel consumption of the entire system?

4.1. Types of heat exchangers

Heat exchangers come in many shapes and forms and each type comes with its advantages and disadvantages. A suitable choice for a heat exchanger has to be made to be integrated into the Airbus A321 Neo APPU. The best heat exchanger is the one that is able to transfer the largest amount of heat, yet having a minimal pressure drop and being small in size and weight. As mentioned by Murshed et al. [17] and Shah [10], heat exchangers in aviation should have a compactness (heat transfer area over heat exchanger volume) of >700 m^2/m^3. Furthermore, the heat exchanger must be able to function over the entirety of its operating range and should be able to withstand temperatures from roughly 20 K to 700 K.
This section will describe common types of heat exchangers, after which a suitable heat exchanger will be chosen.

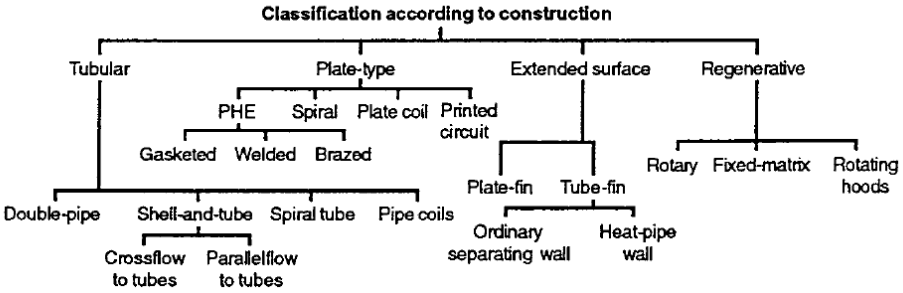

Figure 4.1: Heat exchanger classification based on construction [10]

4.1.1. Tubular Heat Exchangers

Tubular heat exchangers is a type that is generally built of circular tubes and give a considerable amount of flexibility in its design by simply changing the tube length, diameter or arrangement of the tubes. Overall, tubular heat exchangers are able to withstand *high pressures* relative to the environment and are primarily used for liquid-to-liquid and *liquid-to-phase change* heat transfer applications [10].

Double pipe

The simplest type of heat exchanger is the double tube. Herein, a tube surrounds another tube. The inner tube is filled with a fluid of specified temperature, as well as the outer tube. The inner tube is filled with a fluid of specified temperature, as well as the outer tube. This type of heat exchanger is the most affordable to manufacture, easy to (dis)assemble and can be used in tight factory spaces.

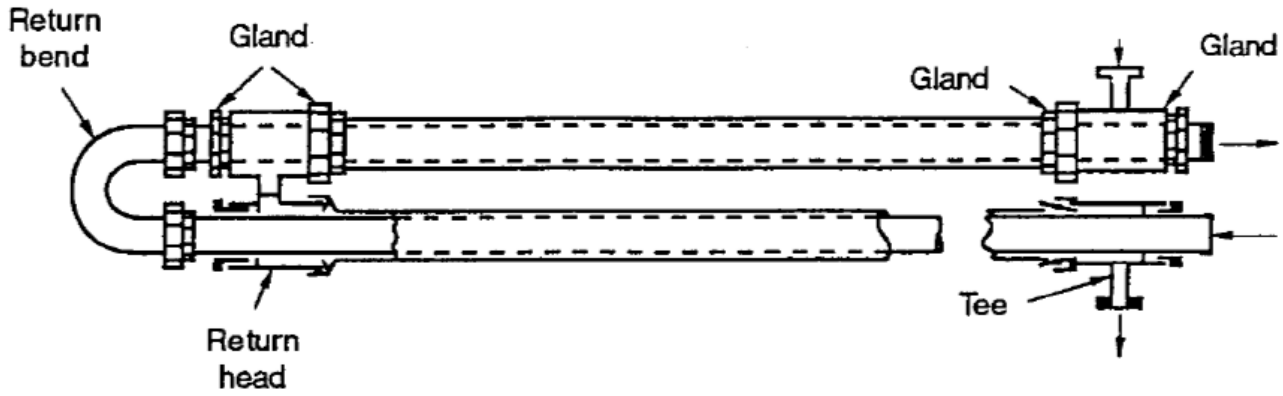

Figure 4.2: Double pipe eat exchanger [10]

A massive downside however, is its bulkiness and its relatively high weight. This makes this type of heat exchanger unsuitable for the APPU.

Table 4.1: Double pipe HEX details

Double pipe			
Pressure range [bar]	vacuum		960
Temperature range		-100	600
Size	Large		
Weight	Large		
Disadvantages	Low allowable pressure drop		

Shell and tube

This type of heat exchanger consists out of multiple (mostly round) tubes surrounded by a hollow cylinder (shell), parallel with each other. One fluid flows within the tubes (also: tube bundle), while another fluid flows across and along the tubes, within the shell. Furthermore, so called baffles can be added which force the fluid within the shell to flow a specific (longer) path, through which the heat transfer is enhanced. The tubes can be 'one-pass', in which the tube bundle covers a distance in a straight sense, or 'multi-pass', in which the tube bundle bends over its covered distance. An example of this can be observed in Figure 4.3.

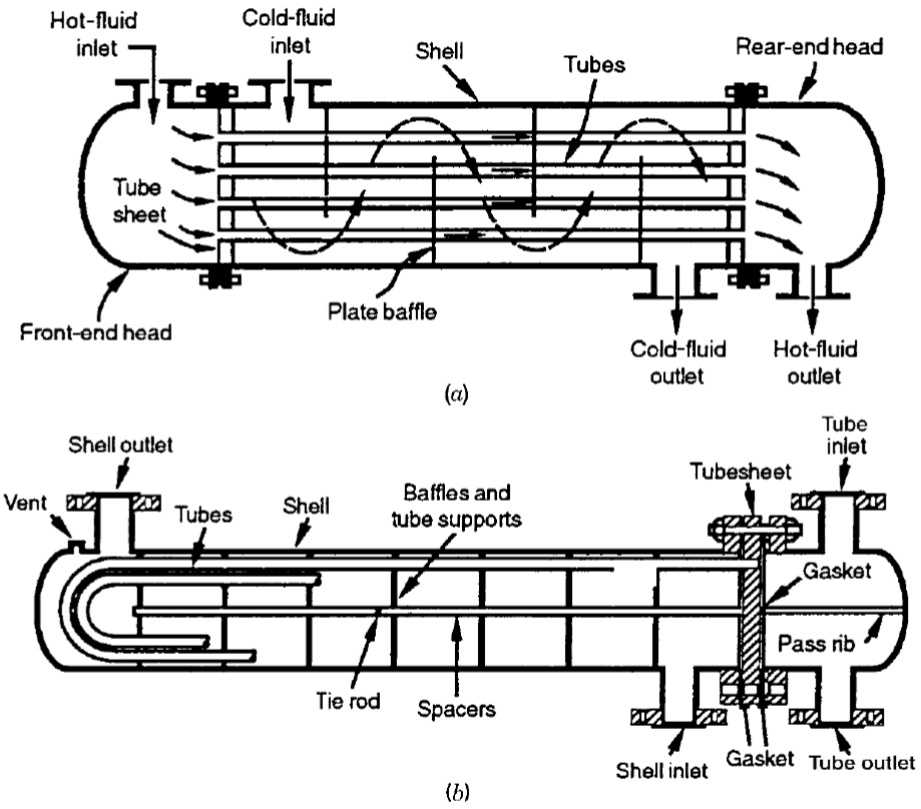

Figure 4.3: Shell-and-tube heat exchanger a) single pass. b) two pass [10]

Shell and tube heat exchangers have a very wide operational range. These heat exchangers operate in pressures close to vacuum till ultrahigh pressures (above 1000 bar); from cryogenic temperatures to high temperatures of about 1400 K or even higher [10]. The temperature and pressure ranges of shell and tube heat exchangers are virtually only limited by the materials of its construction. If the thermostructural properties improve, the operating range of the shell and tube heat exchanger widens. Moreover, Shah and Sekulic mention that shell and tube heat exchangers can easily be designed to withstand rough operating conditions like harsh vibrations [10].
Although the temperature and pressure range is suitable for the APPU, its weight and bulkiness are not. The area to volume ratio is typically not sufficient for it to be used in the APPU.

Table 4.2: Shell-and-tube HEX details

Shell and tube	
Pressure range [bar]	up to 600
Temperature range [° C]	-20 to 500
Size	Very large
Weight	Very large

4.1.2. Plate-Type Heat Exchangers

Another type of heat exchanger are plate-type heat exchangers. These kind of heat exchangers are more compact than the shell-and-tube heat exchangers. Furthermore, these heat exchangers are very efficient, yet cannot serve high pressures, temperatures, or high temperature and pressure differences and are typically only used in liquid-liquid heat exchange[10].
This heat exchanger consists out of thin rectangular well-conducting metal plates stapled and clamped to each other, sealed around the edges by so called 'gaskets' and held together in a frame or matrix. Both ends of the frame (the headpieces) are covered with a thick insulator. The fluid with specified (higher) temperature then enters from the headpiece manifold and flows through the inlet of the first metal piece, filling up the space between these two metal plates and leaving it through the outlet on the other side, flowing out of the heat exchanger. The other fluid (lower temperature) enters the headpiece manifold via another tube and flows through the inlet of the second metal piece, filling up the space and subsequently leaving it through the outlet on the other side, flowing through another channel out of the heat exchanger. This is then repeated for multiple metal plates through the entire heat exchanger. In this manner there exist multiple, high-surface, plates that separate both fluids form each other, but allow heat transfer. A

visualisation of this concept can be observed in Figure 4.4. Often, these metal plates are not smooth, but corrugated for multiple reasons:

- To increase the surface area of the plate
- To propagate turbulence by which heat transfer is enhanced and accumulations of fluid deposits are prevented.
- To stiffen the plate such that a thinner plate can be used, through which the heat transfer is enhanced and the structure becomes lighter.

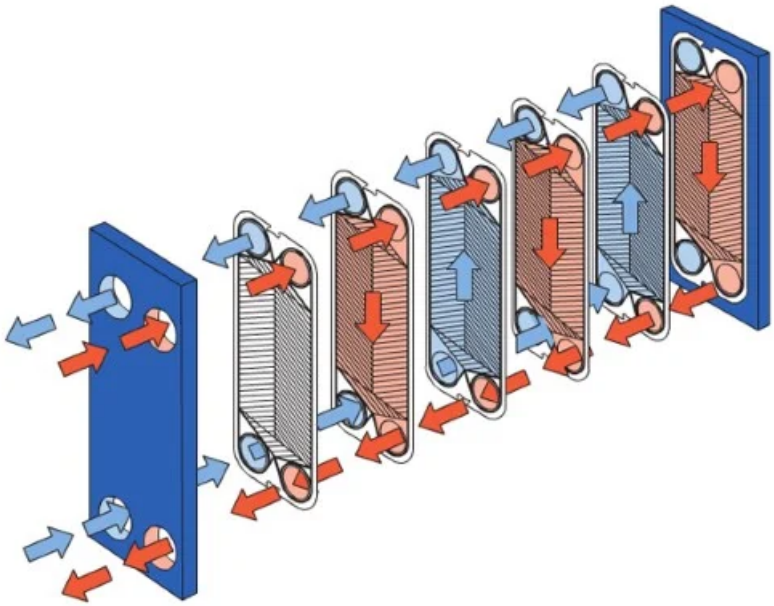

Figure 4.4: Flowing principle of a gasketed plate heat exchanger [11]

Shah [10] provides some general operational characteristics for gasketed plate heat exchangers mentioned in **??**. The limitation of the usage of fluids not higher than 250 $°C$ stem from the limitations of the gaskets materials that tend to be made from rubber, or in more eccentric cases, from asbestos fiber. Moreover, the gaskets limit the use of fluid to noncorrosive fluids.

Plate surface heat exchangers have quite a few advantages over tubular heat exchangers, namely:

- Easy to take apart for cleaning and maintenance.
- The heat transfer surfaces can easily be replaced if the heat exchanger is needed for different tasks.
- Due to the increased shear stresses, secondary flow, high turbulence (due to the corrugated surfaces), there exists a higher mixing, thus reducing the fouling by approximately 10 to 25% with respect to the tubular heat exchangers [10].
- The aforementioned effects, plus the breakup and subsequent reattaching of the boundary layers, swirl, and vortex flow, cause a very high heat transfer coefficient. This increase in heat transfer coefficient means that the heat transfer area could be much smaller, compared to a tubular heat exchanger of similar heat transfer. This means that the cost, total volume and most notably the weight can be decreased. Shah mentions in [10] that the gross weight of a plate surface heat exchanger is approximately one sixth of an equivalent tubular heat exchanger. This aspect would make plate surface heat exchangers especially attractive for aerospace applications.

These advantages come, as usual with certain limitations. The most important limitations are summarised below:

- For equivalent flow velocities, the pressure drop in plate surface heat exchangers is much higher than in tubular heat exchangers. However, the flow velocities needed in plate surface heat exchangers are typically much lower than in tubular heat exchangers, which makes the pressure drop mostly acceptable.
- The pressure range of plate surface heat exchangers is much smaller than tubular heat exchangers.
- Potential of gasket leaking, which could be a problem for toxic fluids or fluids that are ignitable such as hydrogen (especially if the heat exchanger is to be placed in the neighbourhood of a heat source yielding a temperature that is higher than the auto-ignition temperature of the fluid)

- To get a high effectiveness, high viscosity fluids have to be used [33]. This would exclude the usage of most high viscosity gasses (such as air) and high viscosity liquids, such as liquid hydrogen.

Lastly, the channel flow rate of these heat exchangers are relatively speaking very low. For the largest Plate Heat Exchangers, the maximum channel flow rate is 12.5 m^3/h. When converting this amount to the mass flow of liquid hydrogen, this means that a mass flow of no more than 0.246 kg/s of could be achieved. Keeping in mind that the above mentioned upper limit holds for very large (industrially sized) Plate heat exchangers.

Although plate-type heat exchangers can be made very compact, its limited temperature range, proneness to leakages and low effectiveness when using high viscosity fluids, disqualifies this type of heat exchanger to be used in the APPU.

Table 4.3: Plate HEX details [10]

Plate-type			
Pressure range [bar]	1	25	
Temperature range [°C]	-40	200	
Size	Small to large		
Disadvantages	Liquid-liquid only	Leakage risk	large pressure drop

4.1.3. Extended surface

The heat transfer coefficient h for gases is generally one or two order of magnitude lower than that of liquids [10]. To keep the thermal conductance ($h \cdot A$) the same as in liquid-liquid heat exchangers, the a gas-liquid heat exchanger has to have a much larger surface area; this area increase should take place at the gas-side (because h_{gas} is lower here), such that the thermal conductance on both sides is balanced (which decreases the size of the heat exchanger). Extended surface heat exchangers are either plates or tubes (primary surface) that are extended by compact surfaces in the form of fins. To increase the compactness of a heat exchanger, the 'fin density' (number of fins per unit length) should be as high as possible. Adding fins could increase the total heat transfer area by 5 to 12 times the primary surface [10]. Whereas tubular- and plate-type heat exchangers usually have an effectiveness of approximately 60 % (exceptions are possible), extended surfaces can have a much higher effectiveness. Adding fins would decrease the flow area of the fluids and increase its pressure drop, however, this could be countered by making the fins thinner. Other than increasing the heat transfer area, extended surface may either increase or decrease the heat transfer coefficient. Corrugated fins, might induce secondary flows and enhance mixing, therefore, increasing the heat transfer coefficient. Internal fins (i.e. within tubes) however, might slightly reduce the heat transfer coefficient [10]. This increased effectiveness, and compactness makes extended surface heat exchangers a obvious choice for aerospace applications.

Plate-Fin Heat exchangers

A plate-fin heat exchanger is a type in which a plate consisting out of corrugated fins (mostly rectangular or triangular) is sandwiched between two plates through which the gas flows. The liquid flows through tubes that corner the sandwich structure in a parallel fashion. These corner tubes are then divided into individual flow passages parallel to the plate, but perpendicular to the gas flow as shown in Figure 4.5. This causes a 'cross-flow' between the two fluids.

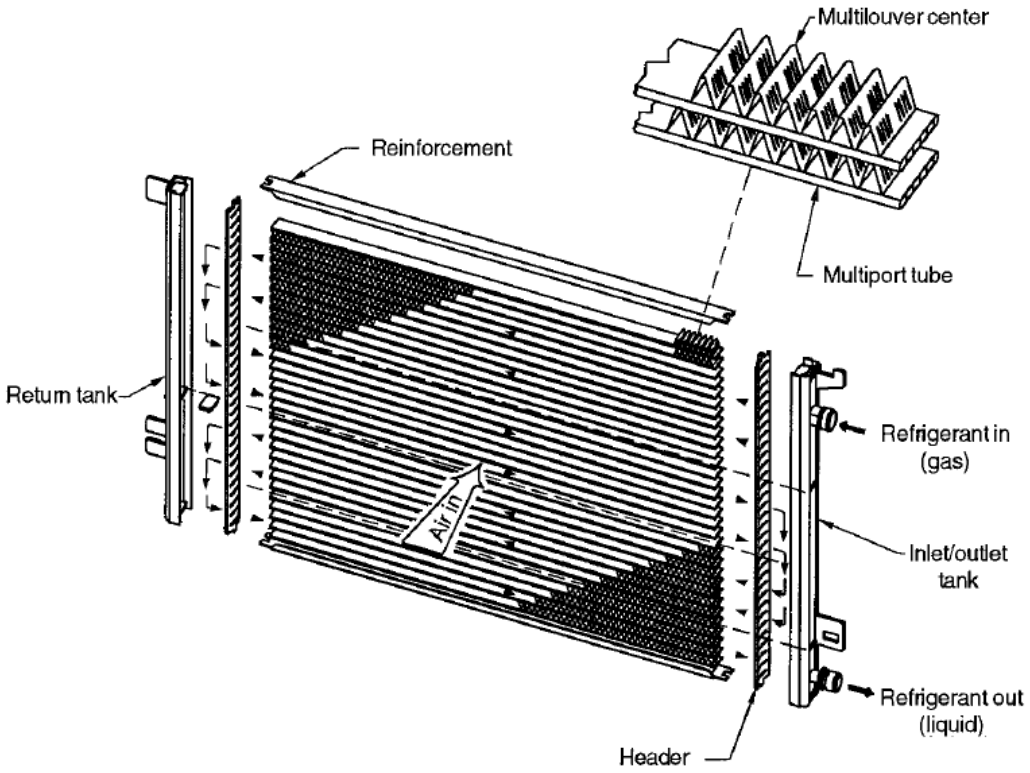

Figure 4.5: Structure of a plate-fin heat exchanger [10]

Plate-fin heat exchangers can be designed for a large range of pressures and temperatures, depending on the structures and materials used. Most plate-fin heat exchangers can operate in an environment of pressures up to 7 bar, however, newer designs are available that can operate under pressures up to 83 bar [10]. The temperature limits depend on the method of bonding and the materials used. There have been created metal plate-fin heat exchangers that allow temperatures up to 1113 K, while those that are made of ceramic materials can reach temperatures up to 1423K. The area density of these types of heat exchangers can be increased by increasing the fin density; Thulukkanam [33] finds that for these types of heat exchangers an area density of 6000 m^2/m^3 is realisable. Furthermore, according to Reay [34] and Shah [10], a *cryogenic* plate-fin exchanger has about 10 volume percent of an equivalent shell-and-tube heat exchanger. However, because the finned web generally has a much smaller thickness, relative to the length and the width, which means that the moment of inertia along the thickness will be much smaller, which could make it more prone to vibrations. Lastly, although this type of heat exchanger can be used for liquid-gas, this type of heat exchanger is especially useful if both fluids are gases as mentioned bay Kays and London [12], as the extended surface can be employed on both fluid sides. If the fluids are liquid and gas however, because the heat transfer coefficients of fluids is generally larger than that of the gas, the large surface area of the tubes would mean that the thermal conductance ($h \cdot A$) on the liquid side would be larger.
Considering the temperature- and pressure ranges, the high possible area density, together with the fact that this type of heat exchanger can be used for gas-liquid, or gas-gas applications, makes the plate-fin HEX a proper candidate to be integrated in the APPU. Its downside however is its proness to vibrations.

Table 4.4: Plate-fin HEX details

Extended surface (plate fin)		
Pressure range [bar]		83
Temperature range	Cryogenic	840
Area density [m^2/m^3]		6000
Effectiveness		95%
Advantages	liquid-gas	gas-gas
Disadvantages	Narrow passages susceptible to fouling	Less tolerant to vibration

Tube-Fin Heat Exchangers

Tube-fin heat exchangers is a type in which one fluid flows through finned tubes, while the other fluid flows through these fins. These fins are placed parallel to the gas flow, contrary to plate-fin heat exchangers. An example can be observed in .

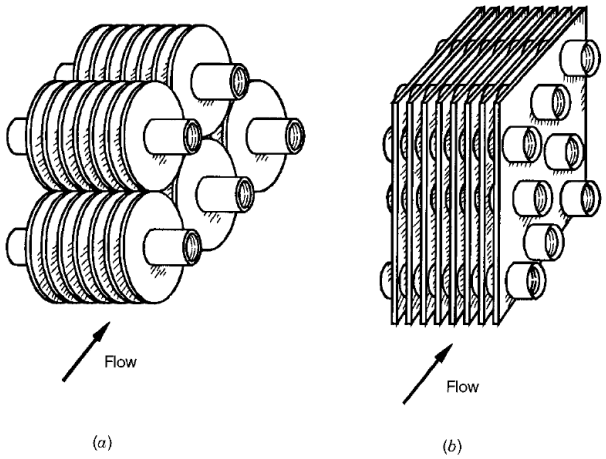

Figure 4.6: Tube-fin Heat Exchanger [10]; a) individually finned tubes; b) continuous fins on tubes

This heat exchanger type can withstand ultrahigh pressures on the tube side. Furthermore, these type of heat exchangers are generally less compact than the plate-fin type, having generally a surface area of about 3300 m^2/m^3 [10] and its heat transfer coefficient is slightly lower than plate-fin types [33]. Its pressure drop however, is a little bit lower compared to the plate-fin type. Contrary to the plate-fin however, this structure is more tolerant against vibrations and is generally used in liquid-gas applications.

Having considered multiple heat exchanger types and how well it fits the design requirements of the APPU, the most obvious choices are the plate-fin and the tube-fin; the plate-fin is more compact but less tolerant to vibrations and is generally more useful in gas-liquid applications. For these reasons, the tube-fin type has been selected to function as a heat exchanger in the APPU.

4.2. HEX Geometry

To get an idea on the heat transfer coefficient and the pressure drop, a HEX geometry has to be selected. For the sake of simplicity, no completely new heat exchanger will be designed, but rather an existing geometry will be selected. Firstly, the shape of the tubes has to be decided on, either circular, or flattened. The most important advantages are shown in Table 4.5; due to the circular shape of the circular tubes, these tubes are more resistant to buckling and allow for very high pressures. The flattened tube on the other hand, is structurally less advantageous, but has a larger heat transfer surface area in return. Moreover, flat tubes can staggered more closely to each other, making the design more compact. Furthermore, the pressure drop in the flattened tubes (hydrogen) is less, as these tubes have a larger cross sectional area for the same volume flow. Moreover, if the flattened tubes are streamlined with the airflow, the amount in pressure loss in the air will also be less. The circular tubes are however easier to manufacture.

Table 4.5: Tubular v.s. flattened tubes

Circular advantages	**Flattened advantages**
Structural integrity	Increased surface area
Ease of manufacturing	Compact design
	Less pressure drop

Due to the fact that the APPU has to be lightweight, compact, and the pressure drop (especially in the airflow) should be small, the decision has been made to use flattened tubes in the heat exchanger.
Kays and London [12] provide tables with dimensional information that is needed to calculate the heat transfer coefficient and the flow-friction of different extended surface heat exchangers. The relevant table can be found in Appendix D. For the flattened tubes, a staggered arrangement is chosen, as this arrangement leads to new thermal boundary layers on the tubes, which propagates the heat transfer. To reduce the pressure drop of the hydrogen, the largest frontal area and the largest hydraulic diameter is chosen, together with the smallest tube width to make the geometry more compact. This makes that the most obvious choice is the "9.1-0.737S" surface designation. This specific heat exchanger has a surface-to-volume ratio of 735 m^2/m^3, which meets the requirement of > 700 m^2/m^3 in aviation heat exchangers.
The tube geometry and the isometric projection can be observed in Figure 4.7 and Figure 4.8, respectively. Its relevant geometrical parameters can be found in Table 4.6.

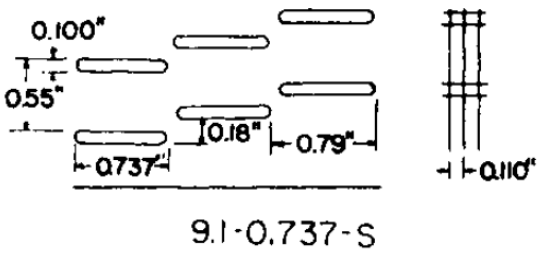

Figure 4.7: Tubes geometry and spacing (in inches) [12]

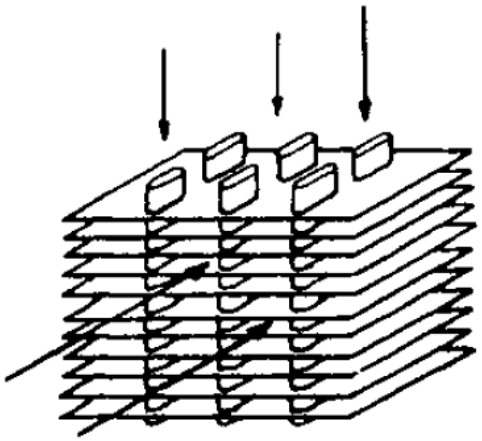

Figure 4.8: Flat finned-tubes continuous fins [12]

Table 4.6: Geometrical parameters tube-fin heat exchanger

Parameter	**Value**
Surface (air-side) area to volume ratio α_{air} $[m^2/m^3]$	735
Free-flow/frontal area ratio σ	0.788
Hydraulic diameter (air side) $D_{h,air}$ [mm]	4.21
Hydraulic diameter (hydrogen side) $D_{h,H2}$ [mm]	4.63
Tube width (normal to flow) W_{tube} [mm]	2.54
Tube length (parallel to flow) L_{tube} [mm]	18.7
Tube wall thickness t_{wall} [mm]	0.254
Transverse spacing between tubes s_{trans} [mm]	11.4
Longitudinal spacing between tubes s_{long} [mm]	1.35
Fin thickness t_{fin}[mm]	0.102
Fins/mm	3.6
Fin spacing s_{fin} [mm]	2.72
Fin area/total area λ_{fin}	0.813

The actual size of the HEX is unknown, as well as the dimensions of the APPU engine, which makes deciding on a heat exchanger size especially difficult. Moreover, the actual sizing of the heat exchanger is an iterative process: the geometry size is needed to calculate the dimensionless Reynolds number, Nusselt number and pressure drop et cetera, from which the heat transfer coefficient can be calculated. If the heat transfer coefficient is too high on one side ($h \cdot A$ should be equal on both sides), then the surface area has to decrease, which means that the Reynolds- and Nusselt number et cetera also change.

Carozza [17] finds that typical heat exchanger sizes vary as mentioned in Table 4.7 for heat exchangers. As an initial geometry the width, height and depth are assumed to be 30 cm, 20 cm and 10 cm, respectively. The heat exchanger is visualised in Figure 4.9

Table 4.7: Typical heat exchanger dimensions in aircraft

	Minimum	Maximum
Width [cm]	10	132
Height [cm]	2.5	132
Depth [cm]	1.9	31

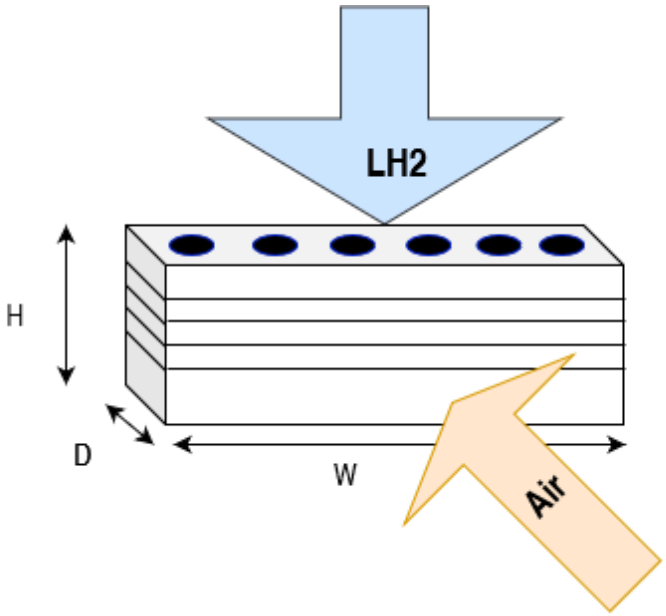

Figure 4.9: Heat exchanger to be used in the APPU, initial dimensions (own work)

4.3. Heat Transfer Coefficient and Pressure Loss

The heat transfer can be calculated by Equation 4.1.

$$Q = h \cdot A \cdot \Delta T \tag{4.1}$$

If the temperatures and surfaces are known, the remaining variable is the heat transfer coefficient. The heat transfer coefficient can be calculated using by Equation 4.2.

$$h = \frac{\overline{Nu} \cdot \overline{k}}{D_h} \tag{4.2}$$

In which Nu, k, D_h are the Nusselt number, the thermal conductivity of the fluid and the hydraulic diameter of the flow. The values of Nusselt number and the thermal conductivity should be averaged over the entire heat transfer. These values however, are a function of temperature. The entering temperatures of the heat exchanger are known, but the leaving temperatures are initially not.

4.3.1. Deciding on the Limits

If the hydrogen would absorb the maximum amount of heat, its leaving temperature would approach the temperature of the entering airflow (736 K), which is well below the auto-ignition temperature of hydrogen. However, because the heat capacity rate ratio ($c_p \cdot \dot{m}$) of hydrogen is much larger than that of the airflow, this limit cannot be reached. It is however, desired to increase the H_2 temperature as much as possible, as a lower hydrogen temperature entering the combustor induces a lower LHV, which is a lost potential of extracting energy in the combustion chamber. Moreover, if the difference in temperature between the combustion chamber and the hydrogen fuel is large, it could lead to thermal stresses.

A downside of heating up the entering fuel to such a high temperature however, is the fact that the cooled air becomes very low. Although the mass flow of the hot air is approximately 5 times higher than the mass flow of the hydrogen, the specific heat capacity of hydrogen is more than 10 times as high as that of air over the entire range. Moreover, the specific heat capacity of hydrogen briefly peaks at 90 times the specific heat capacity of air [35], when the hydrogen transitions from liquid to a supercritical liquid. This means that for the given amount of mass flows, the air decreases in temperature faster than that the hydrogen increases its temperature. This limits the maximum achievable temperature of hydrogen. Neglecting the impact of thermal stresses for the moment, the limit becomes the condensation

temperature of air at the given pressure (13.3 bar), or rather the species that has the highest condensation temperature of in air, which happens to be oxygen. As at 13.3 bar, oxygen condenses at 124 K, while nitrogen condenses at 108 K. However, one should not neglect the presence of water in the air. Although the Dymola model assumes no water to be present in the inlet air, as the small molar percentage of water is deemed negligible when it comes to the thermodynamics of the system, one should not neglect the physical implications water could have on the components (mainly the HPT). However, normally condensed water or even ice is not deemed to be an issue due to its small proportions, and due to the fact that every engine that works at a cruise altitude of 10 km will have ice particles entering the engine. The difference however, is that in ordinary aero-engines, the solid, or liquid water quickly vaporises in the LPC due to the increase of temperature. Therefore, injecting the HPT with air cooled down to the point that it contains ice particles could be an issue for the structure of the HPT blades, especially because the velocity of the airflow in the HPT is much higher than the velocity of the air in an LPC, as can be observed in Figure 4.10, which shows a velocity profile of a generic turbojet engine.

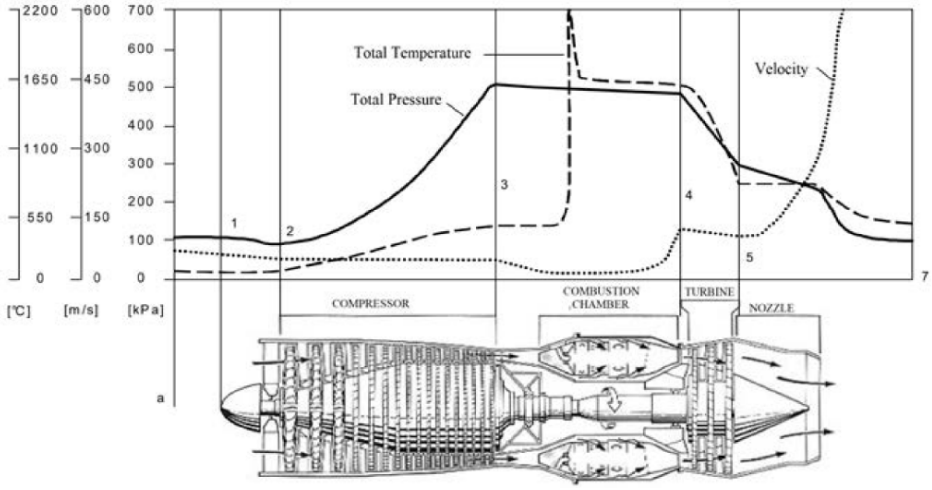

Figure 4.10: Pressure- and velocity profile of a generic aero-engine [13]

Understanding these situations, a temperature limit of the airflow be considered: $T_{air} > T_{melt,H_2O}$ at 13.3, which is approximately equal to 273.1 K, as the melting point of water changes very little as a function of pressure.
Having the entering and the leaving temperature of the airflow, its thermophysical properties can be averaged. The leaving temperature of the hydrogen flow however, is found by means of iteration.

4.3.2. Heat Transfer Coefficient

Firstly, the frontal area of the heat exchanger is calculated.

$$A_{front,air} = W \cdot H \tag{4.3}$$

Subsequently, the mass flux can be calculated using the free-flow over frontal area ratio σ, as mentioned in Equation 4.4.

$$G = \frac{\dot{m}}{A_{front} \cdot \sigma} \tag{4.4}$$

From this, the Reynolds number of air can be calculated with Equation 4.5.

$$\mathrm{Re} = \frac{uD_\mathrm{h}}{\overline{\nu}} = \frac{\rho u D_\mathrm{h}}{\overline{\mu}} = \frac{\rho Q D_\mathrm{h}}{\bar{\mu} A} = \frac{W D_\mathrm{h}}{\overline{\mu} A} = \frac{G D_h}{\overline{\mu}} \tag{4.5}$$

In which u, $\overline{\nu}$, $\overline{\mu}$, Q, W, G are defined as the flow velocity, plate averaged kinematic- and dynamic viscosity, volume rate, mass flow and mass flux, respectively.
There are a number of empirical equations that solve the Nusselt number, each empirical equation has its accompanied flow regime. The Nusselt number averaged over the length of a flat plate in laminar flow can be calculated with Equation 4.6 [36].

$$\overline{Nu} = 0.664 \cdot Re^{1/2} \cdot Pr^{1/3}; \quad for \quad Pr > 0.6 \tag{4.6}$$

Equation 4.2, Equation 4.4 and Equation 4.5 can be applied for the hydrogen side as well, while the frontal area is calculated with Equation 4.7.

$$A_{front,H2} = D \cdot W \tag{4.7}$$

To calculate the Nusselt number of a fluid in a pipe, Equation 4.8 has been proposed by Gnielinski [37]. This empirical

correlation is valid for *smooth* pipes at Prandtl numbers varying from 0.5 up to 2000 [36]. The friction factor f can be calculated by Equation 4.9 [38] or Equation 4.10, if the flow is laminar [36].

$$Nu = \frac{\left(\frac{f}{8}\right) Re \cdot Pr}{1 + 12.7 \cdot \left(\frac{f}{8}\right)^{1/2} \left(Pr^{2/3} - 1\right)}; \quad for \quad 3000 < Re < 5 \cdot 10^6 \tag{4.8}$$

$$f = (0.79 \cdot \ln(Re) - 1.64)^{-2}; \quad for \quad 3000 < Re < 5 \cdot 10^6 \tag{4.9}$$

$$f = \frac{K}{Re}; \quad for \quad Re < 3000 \tag{4.10}$$

In which K takes different values, depending on the shape of the channel. For the tube geometry as described in Figure 4.7, K takes the value of 82, while the flow channel of the airflow (in which the fin surfaces act as channel walls), K becomes 96, as mentioned by Bergmann et. all [36].
After the heat transfer coefficients of both sides have been calculated, the thermal conductance ($h \cdot A_{heattransfer}$) can be calculated. As previously mentioned, for an optimal heat exchange, the thermal conductance should be the same on the both side, as the heat transfer rate is limited by the lowest thermal conductance. If the thermal conductance is the same on both sides, the heat exchanger isn't over-designed on one side, resulting in the heat exchanger being more compact.
To make the thermal conductance the same on both sides, the geometry (W, D, H) of the heat exchange has to be changed. This will change the surface area of heat transfer, but also changes the Reynolds- and subsequently the Nusselt numbers on both sides. This is an iterative process; W, D, H will be changed until h_{air} - h_{H2} are close to zero (with a specified margin).

4.3.3. Effectiveness

The effectiveness of a heat exchanger is defined as the amount of heat that it is able to transfer, compared to the theoretical maximum amount of heat transfer, as defined in Equation 4.11 by [10].

$$\epsilon = \frac{q_{actual}}{q_{max}} \tag{4.11}$$

Using the $\epsilon - NTU$ method as described by Shah et al. [10] and Thulukkanam [33], Equation 4.11 can be calculated using Equation 4.12.

$$\varepsilon = \frac{1 - e^{-NTU(1-C_r)}}{1 - C_r \cdot e^{-NTU(1-C_r)}} \tag{4.12}$$

In which NTU and C_r are the number of transfer units, and the ratio of the minimum and maximum heat transfer rates, and defined as mentioned in Equation 4.13 and Equation 4.18, respectively.

$$NTU = \frac{UA}{C_{\min}} \tag{4.13}$$

In which U is the overall heat transfer coefficient and can be calculated by Equation 4.14.

$$U_{\text{air}} = \frac{1}{\frac{1}{\eta_0 h_{\text{air}}} + \frac{1}{\left(\frac{\alpha_{H2}}{\alpha_{\text{air}}}\right) \cdot h_{H2}}} \tag{4.14}$$

The fin effectiveness n_{fin} is and can be calculated with Equation 4.15 [36].

$$\eta_{fin} = \frac{\tanh\left(mL_{fin}\right)}{mL_{fin}} \tag{4.15}$$

$$m = \sqrt{\frac{2h_{\text{air}}}{k_{fin} t_{fin}}} \tag{4.16}$$

In which α_{air} is the heat transfer surface of the air-side over the total volume of the heat exchanger as given in Table 4.6. The heat transfer surface to area ratio of the tubes can be calculated by:

$$\alpha_{H2} = \frac{P \cdot N_{tubes}}{D \cdot W} \tag{4.17}$$

In which P is the perimeter of the tube and N_{tubes} is the number of tubes within the heat exchanger.

$$C_r = \frac{C_{\min}}{C_{\max}} \tag{4.18}$$

In which C is defined in Equation 4.19.

$$C = \dot{m} \cdot c_p \tag{4.19}$$

The minimum and maximum heat capacity rates in Equation 4.18, are concern both the airflow and the hydrogen flow, meaning that C_{max} and C_{min} take the value of whichever flow has the minimum or maximum value.

4.3.4. Pressure drop

Other than the the compactness and effectiveness of a heat exchanger that should be as high as possible, the pressure losses should be as little as possible, as a pressure drop means a decrease in the potential to create work. The pressure drop is proportional to the velocity squared.

$$\Delta P \propto V^2 \tag{4.20}$$

This means that decreasing the fluid velocity through a heat exchanger will limit its pressure drop.
In this study two sorts of pressure loss are considered:

- Pressure loss of both fluids in the heat exchanger (which are modelled as frictional pressure losses)
- Pressure loss of the airflow through a diffuser; as the mass flow has to be slowed down to enter the heat exchanger at its specified inlet area (which is modelled as a dynamic pressure loss).

The pressure loss through the tubes is defined by Thulukkanam [33], in Equation 4.21, while the pressure loss over the fins is defined in Equation 4.22.

$$\frac{2G_{H2}^2}{\overline{\rho_{H2}}} \cdot f \cdot \frac{H}{D_{h,H2}} \tag{4.21}$$

$$\frac{G_{\text{air}}^2}{2\rho_{\text{air,in}}}\left((1+\sigma_{\text{air}}^2)\left(\frac{\rho_{\text{air,in}}}{\rho_{\text{air,out}}}\right)-1\right)+f\cdot 4\frac{D}{D_{h,\text{air}}}\cdot\frac{\rho_{\text{air,in}}}{0.5\left(\rho_{\text{air,in}}+\rho_{\text{air,out}}\right)} \tag{4.22}$$

To calculate the total pressure loss in the diffuser, Equation 4.23 is used, as provided by Legg [39] in which K_{loss} is defined by House [14] as the loss coefficient .

$$\Delta P_f = K_{\text{loss}} \cdot \frac{1}{2} \cdot \rho \overline{V^2} \tag{4.23}$$

$$K_{loss} = C_0 \cdot \left(1 - \frac{A_{in}}{A_{out}}\right)^2 \tag{4.24}$$

In which $\overline{V}$ and C_0 are the mean velocity and the fitting loss coefficient which depends on the area ratio and the angle of the diffusing duct, respectively, as shown in Figure 4.11 and Figure 4.12.

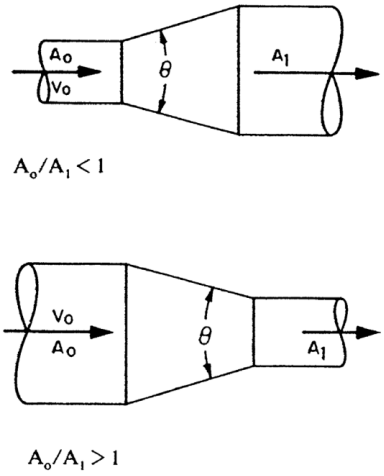

	C_o									
	θ, degrees									
A_o/A_1	10	15	20	30	45	60	90	120	150	180
0.06	0.21	0.29	0.38	0.60	0.84	0.88	0.88	0.88	0.88	0.88
0.1	0.21	0.28	0.38	0.59	0.76	0.80	0.83	0.84	0.83	0.83
0.25	0.16	0.22	0.30	0.46	0.61	0.68	0.64	0.63	0.62	0.62
0.5	0.11	0.13	0.19	0.32	0.33	0.33	0.32	0.31	0.30	0.30
1	0	0	0	0	0	0	0	0	0	0
2	0.20	0.20	0.20	0.20	0.22	0.24	0.48	0.72	0.96	1.0
4	0.80	0.64	0.64	0.64	0.88	1.1	2.7	4.3	5.6	6.6
6	1.8	1.4	1.4	1.4	2.0	2.5	6.5	10	13	15
10	5.0	5.0	5.0	5.0	6.5	8.0	19	29	37	43

Figure 4.11: Fitting loss coefficient in a conical diffuser[14]

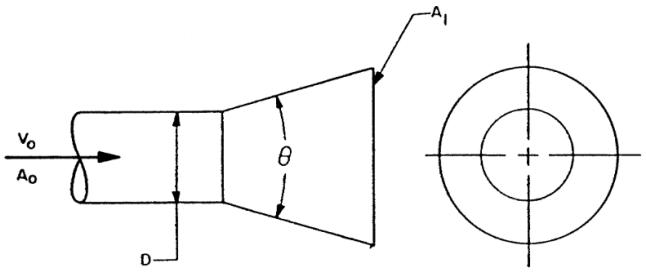

	C_o						
	θ, degrees						
A_1/A_o	8	10	14	20	30	45	≥60
2	0.36	0.33	0.37	0.51	0.90	1.0	1.0
4	0.24	0.21	0.28	0.40	0.70	0.99	1.0
6	0.20	0.19	0.26	0.37	0.67	0.99	1.0
10	0.18	0.16	0.24	0.36	0.68	0.99	1.0
16	0.16	0.16	0.20	0.36	0.66	0.99	1.0

Figure 4.12: Fitting loss coefficient in an annular conical diffuser [14]

Typical pressure losses in aircraft ducts lie in the range of 1 - 5%, as mentioned by Farokhi [40]. Patrao et al. [41] found that the pressure drop in their researched intercooler yielded a pressure loss between 1% and 3%. A generic visualisation of an engine can be observed in Figure 4.13, together with the position and a generic schematic of the the intercooler.

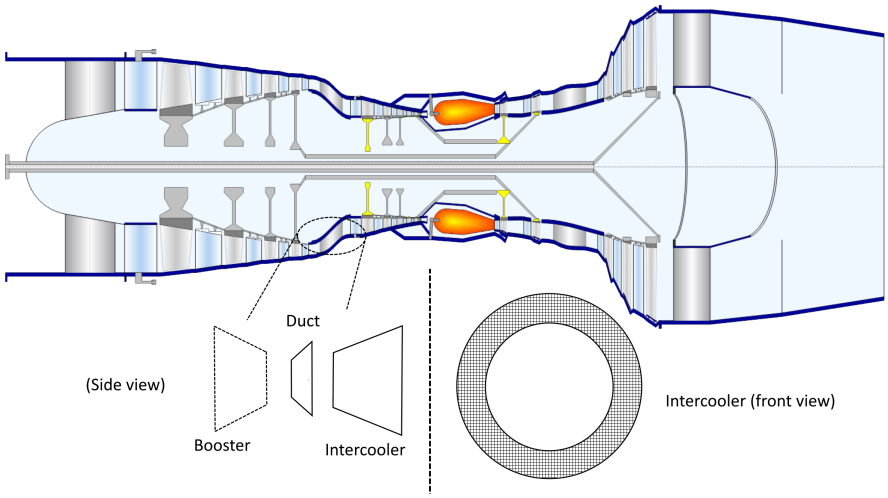

Figure 4.13: Intercooler in APPU (own work)

4.4. Weight estimations

To make an estimation of the heat exchanger weight, the first step is to decide on the material to be used. Thulukkanam [33] finds that the best materials to be used in cryogenic heat exchangers, are aluminium alloys because of its high thermal conductivity (k), strength at low temperature and low cost. Moreover, aluminium has a low density, relative to other metals, which is beneficial in aviation. Thulukkanam suggest a number of aluminium alloys: aluminum alloy 3003, 5154, 5083, 5086, or 5454. Table 4.8 shows important properties for the mentioned alloys[42]. Considering that each alloy is suitable the use in cryogenic heat exchangers, the alloy with the highest thermal conductivity and melting onset temperature is chosen, which is Al-3003.

Table 4.8: Properties aluminium alloys, suitable for cryogenic heat exchangers

	Al-3003	Al-5154	Al-5083	Al-5086	Al-5484
Thermal conductivity k $[W/(m \cdot K)]$	180	130	120	130	130
Density $\rho[kg/m^3]$	2.8	2.7	2.7	2.7	2.7
Melting onset temperature [K]	910	860	850	860	870

Kays et al. [12] find that the specific weight for this heat exchanger configuration yields 875 kg/m^3 for steel. This means that the specific weight of this specific heat exchanger when made out of aluminium, yields $\frac{\rho_{Al}}{\rho_{steel}} \cdot 875$, which equals 314 kg/m^3. Brooks et. al. [43] use a 20% multiplier to account for the additional connecting hardware. This means that the heat exchanger and its installation can be calculated by:

$$m_{HEX} = 1.2 \cdot D \cdot W \cdot H \cdot \rho_{HEX} \tag{4.25}$$

With ρ_{HEX} being the density of the heat exchanger structure, as mentioned above.

5

Methodologies on modelling the APPU

To predict the *heat management and performance increase of an engine cycle using liquid hydrogen* (such as the APPU), a model has to be made. This model can constructed using Dymola [44]; a modeling and simulation environment based on the Modelica language.
Concerning the APPU model, initial work has been done by the Delft University of Technology in GasTurb 12, a tool specifically designed for aero-engine simulation. It has been decided that GasTurb would not be optimal for this research, as GasTurb limits the user in modelling innovative designs. As an example, GasTurb doesn't allow the user to model a combined compressor (axial booster & radial HPC), nor does it allow the user to put a heat exchanger in the model at any place desired, contrary to Dymola. For this reason, the decision has been made to continue the research with Dymola. However, as the initial work has been done in GasTurb, the model first has to be converted to Dymola.
This chapter will elaborate on the analysis tools such as GasTurb and Dymola, followed by a conversion of the GasTurb model into a Dymola model, followed by a lay-out of different Dymola models.

5.1. GasTurb

GasTurb is a program that allows the design and off-design performance of gas turbines [45]. GasTurb initially uses basic thermodynamic equations to solve for the thermodynamic variables at each station, using a semi-perfect gas assumption, meaning that the specific heat capacity is dependent on temperature and substance composition, while it is independent of pressure ($C_P(T, X_i)$). GasTurb models the flow as one-dimensional, through which it is able to give values at the entry- and at the exit plane of each component, however there is no variability in that plane. Furthermore, GasTurb calculates the variables at the stations at steady-state conditions, however, the program allows the user to simulate a transient, based on a polar moment of inertia, specified by the user. Furthermore, the software uses component maps, such as compressor- and turbine maps that are extracted from experimental data, to model off-design behaviour, when the engine is operating at a different altitude, inlet Mach number, or when the engine is accelerating et cetera. Moreover, the inclusion of component maps by GasTurb, allows variation of the component efficiencies with changing flight conditions.
This is beneficial when the user wants to design a complete new engine, but also offers the user adequate tools to commit parametric studies on an already existing engine to acquire knowledge on its behaviour. This comes in use when the user wants to change the design point and make a so called 'sibling' of the baseline.

5.2. Dymola

Dymola uses the Modelica language, which is also used in the OpenModelica software. As the Modelica language makes use of object-oriented features, it is able to use independent, interchangeable models by which new models can be created by connecting sub-models or components with each other. Components can be created from scratch by implementing mathematical (system component) equations. Having a model means that systems of equations exist and in most dynamic models differential equations are present, this means that Dymola needs to solve so called 'Differential-algebraic systems of equations' (or DAE for short). Furthermore, Dymola allows a-causal modeling, which means that the connectors of models are designed through physical compatibility instead of causal compatibility. This means that the connector only concerns with the physical information, and not with the direction of the information flow. This allows the user to easily compose new models.
Contrary to computational fluid dynamics, Dymola (as well as GasTurb) models using 'lumped parameters modelling' (also called 0-D modelling). This means that the thermodynamic variables in a control volume are averaged. This reduces the state-space of the model to a system of finite dimensions, furthermore, it reduces the PDEs into ODEs.
Although Dymola can be used for engine design, the program isn't specifically an aerospace tool, rather it can be used for mechanical engineering in general, electrical engineering, control engineering, etc.

This allows the user to extend and adapt the created model freely, thus allowing the user to come up with innovative designs. Dymola offers a larger degree of freedom in designing models than GasTurb, as Dymola is created for multi-engineering purposes. As this study will be integrating heat exchangers, intercoolers and an additional thermodynamic cycles, Dymola provides the versatility that GasTurb doesn't. For this reason, the decision has been made to construct the models in Dymola.

5.3. Solving methods

Differential equations come in many shapes and forms. One of these types are ordinary differential equations (ODE's for short). ODE's are differential equations that are dependent on *one* independent variable which fulfils an equation in the form as denoted in 5.1.

$$y^n = F\Big(x, y, y', y'', \dots, y^{n-1}\Big) \tag{5.1}$$

The independent variable in 5.1 is x and it's order is n, indicating that the ODE constitutes out of n derivatives. Simpler types of ODE's are first order derivatives, in which n is limited to 1. In such a case, one obtains 5.2.

$$y'(x) = F\Big(x, y\Big) \tag{5.2}$$

Generally these equations yield an infinite amount of solutions. If additional conditions are applied, one can single out a specific solution. Commonly, two types of conditions are used: initial conditions

$$y(t_0) = y_0 \tag{5.3}$$

and boundary conditions

$$g\big(y(x_0), y(x_n)\big) = 0 \tag{5.4}$$

in which g is a function of two variables in this specific case. The amount of boundary conditions depend on the amount of dimensions the ODE entails.
More generally, one can consider a system of p first order ODE's

$$\begin{aligned} y_1' &= f_1\big(x, y_1, y_2, \dots, y_p\big) \\ y_2' &= f_1\big(x, y_1, y_2, \dots, y_p\big) \\ &\vdots \\ y_p' &= f_1\big(x, y_1, y_2, \dots, y_p\big) \end{aligned}$$

for p unknown functions $y_i(x), i = 1, \dots, p$. These systems can be written in vector form

$$\mathbf{y'} = \begin{bmatrix} y_1' \\ \vdots \\ y_p' \end{bmatrix}, \mathbf{F}(x, y = \begin{bmatrix} f_1\big(x, y_1, \dots, y_p\big) \\ \vdots \\ f_1\big(x, y_1, \dots, y_p\big) \end{bmatrix} \tag{5.5}$$

In most cases, Equation 5.5 is not analytically solvable, instead numerical methods have been established to provide approximate solutions. This is done by using so called 'nodes': basically providing a select group of x-coordinates for which the y-values are to be calculated. There exist different methods of defining the x-coordinates, the most basic method of defining a set of x-coordinates is by means of using an equidistant set of x-coordinates: $x_i = x_0 + i \cdot h$. In which h is defined as the *step size*. If Equation 5.2 is integrated, one obtains Equation 5.6.

$$y(x_{i+1}) = y(x_i) + \int_{x_i}^{x_{i+1}} f\big(t, y(t)\big), i = 0, \dots, n-1 \tag{5.6}$$

with $y(x_i)$ being the constant of integration and x_i being a node on which numerical computation is executed. The integral can then be numerically integrated by means of discretisation

$$\int_a^b f(x) \approx \Sigma_i^n w_i \cdot f(x_i) \tag{5.7}$$

with w_i being the quadrature weights for $i = 0, \dots, n$. The weights can be calculated using different methods. If equidistant nodes are used to solve Equation 5.7, one speaks about Newton-Cotes formulas. The integration domain [a,b] is subdivided into n intervals of equal length, such that one obtains

$$x_i = a + i \cdot h \tag{5.8}$$

such that $h = \frac{b-a}{n}$ with the number of nodes being equal to $s = n+1$ (this is the case of closed Newton-Cotes formulas are considered, if open Newton-Cotes formulas are considered, s becomes $n-1$). If $s = 2$, one uses the trapezoidal rule, in which Equation 5.7 becomes Equation 5.9.

$$\int_a^b f(x) \approx \Sigma_i^n w_i \cdot f(x_i) = \frac{b-a}{2}\Big(f(a) + f(b)\Big) \tag{5.9}$$

in which the error term becomes $\frac{1}{12}h^3 f^{(2)}(\xi)$; while if $s = 3$, one gets Simpon's rule and becomes Equation 5.10

$$\int_a^b f(x) \approx \Sigma_i^n w_i \cdot f(x_i) = \frac{b-a}{6}\left(f(a) + 4f\left(\frac{a+b}{2}\right) + f(b)\right) \tag{5.10}$$

in which the error term becomes $-\frac{h^5}{90} f^{(4)}(\xi)$; while if $s = 4$, one gets Simpon's 3/8 rule and becomes Equation 5.11

$$\int_a^b f(x) \approx \Sigma_i^n w_i \cdot f(x_i) = \frac{b-a}{8}\left(f(a) + 3f\left(\frac{2a+b}{3}\right) + 3f\left(\frac{a+2b}{3}\right) + f(b)\right) \tag{5.11}$$

in which the error term becomes $-\frac{3}{80} f^{(4)}(\xi)$. When numerically calculating $y(x_{i+1})$ in Equation 5.6 by means of one of the aforementioned Newton-Cotes formulas, one introduces a local truncation error. This can be represented in Equation 5.12.

$$y(x_{i+1}) = y(x_i) + Q(f, y; x_i, x_{i+1}) + E(f, y; x_i, x_{i+1}) \tag{5.12}$$

The local truncation error E, is dictated by the error terms in the Newton-Cotes formulas and is a function of the step-size h. If the error is ignored, one simplifies the equation to Equation 5.13.

$$y(x_{i+1}) \approx y(x_i) + Q(f, y; x_i, x_{i+1}) \tag{5.13}$$

Indeed, the local truncation error E only analyses the error per step, that is, from x_i to x_{i+1}. Assuming that one wants to solve an initial value problem, the only known value is $y(x_0)$, this means that one obtains its first truncation error at x_1, however, as to solve the integral numerically, a range of values is needed, almost always ranging further than x_1, the truncation error is accumulated. This accumulation is often called the global discretisation error.

Understanding how the integral of Equation 5.6 can be numerically integrated, one has to understand what methods of exist to compute the values of the consecutive nodes. Commonly, in the numerical analysis of differential equations, two types of methods are distinguished:

- Single step methods (also: first-order methods) in which y_{i+1} is computed using one other step.
- Multi step methods (also: multi-order methods) in which y_{i+1} is computed using more than one step.

Single step methods are methods of the form

$$y_{i+1} = y_i + h \cdot \phi(y_{i+1}, y_i, x_i, h), \qquad i = 0, \ldots, n-1 \tag{5.14}$$

in which ϕ is an arbitrary function. ϕ is defined to be implicit if dependent on y_{i+1} and explicit if independent on y_{i+1}.

5.3.1. Euler-Cauchy

5.3.2. Forward Euler

One type of the single step methods is the (forward) Euler-Cauchy method (forward is a synonym for explicit, while the backward Euler is implicit). This explicit single step method is construed as follows:

$$y_{i+1} = y_i + h \cdot f(y_i, x_i) \tag{5.15}$$

Subsequently, if a *single* node Newton-Cotes formula is used, with using Taylor expansion of Equation 5.15, the local discretisation error can be derived to be in the form

$$\epsilon_{i+1}^{EC} = \frac{1}{2}h^2 y''(\xi_i), \quad \xi_i \in [x_i, x_{i+1}], \quad i = 0, \ldots, n-1 \tag{5.16}$$

As a general rule of thumb, if the local truncation error yields $\mathcal{O}(h^n)$, the global truncation error can be described by $\mathcal{O}(h^{n-1})$. Meaning that if the step size h decreases by an amount of $1/b$, the global truncation error also with an amount of $1/b$. At the first step, the solution of the derivative of y will be exact, as y_0 is defined in an initial value problem.

5.3.3. Backward Euler

Contrary to the forward (or explicit) Euler, one can solve the backward (or implicit) Euler. In this case, y_{i+1} is solved by replacing i by +1 in Equation 5.15. Such that one obtains:

$$y_{i+1} = y_i + h \cdot f(y_{i+1}, x_{i+1}) \tag{5.17}$$

Taylor expanding Equation 5.17 and substituting its relevant components, one finds that the error of the backward Euler equals the error of the forward Euler in Equation 5.16. The stability of the backwards Euler, however, is better than the stability of the forward Euler, meaning that for the same time step, the error of the forward Euler may be amplified per time step, while the backwards Euler stays within bounds. This is a clear advantage of the backward Euler.

5.3.4. Method of Heun

In Subsection 5.3.1, the analysis was conducted by solving the quadrature formula (Equation 5.7) by using a closed, single node, Newton-Cotes formula, with the note being specified at the either the lower or upper bound of the domain. Naturally, it is also possible to solve the quadrature equations for higher order methods such as the trapezoidal rule Equation 5.9. In this manner, one obtains a higher order method for solving an ODE with a smaller truncation error. Applying the trapezoidal rule to Equation 5.14, one obtains:

$$y_{i+1} \approx y_i + \frac{h}{2} \cdot \Big(f(x_i, y_i) + f(y_{i+1}, x_{i+1}) \Big) \tag{5.18}$$

which is an implicit single step method and is called The Method of Heun. As a starting value, the forward Euler method is used. The local discretisation error is defined as

$$\epsilon^H_{i+1} = -\frac{h^3}{12} f''\big(\xi_i, y(\xi_i)\big), \quad \xi_i \in [x_i, x_{i+1}], \quad i = 0, \ldots, n-1 \tag{5.19}$$

which yields a local truncation error of $\mathcal{O}^3$ (and thus a global truncation error of $\mathcal{O}^2$, which is one order higher than Euler-Cauchy. This means that the global error decreases by an amount of $1/b^2$, if the step size h is decreased by an amount of $1/b$.

5.3.5. Classical Runge-Kutta method

To obtain an even more accurate solution, without decreasing the step size too much, another method called the 'Classical Runge-Kutta method' can be used. Understanding this method is much more difficult than the aforementioned methods, as for each step, this method uses weighed nodes in a linear system. Because for each step, a linear system has to be solved, this method is not only more difficult to understand, but also more costly to solve. The upside however, is that one obtains a local discretisation error of $\mathcal{O}^5$ and a global discretisation error of $\mathcal{O}^4$. Furthermore, the linear system of equations to be solved, has a degree of freedom of 2, meaning that the solver has to make two 'educated guesses' to close the system. The Runge-Kutta method can be subdivided in explicit and implicit methods, but for the sake of simplicity, only the explicit method will be discussed in this section. The values for y are calculated with Equation 5.20

$$\begin{aligned} y_{i+1} &= y_i + \sum_{j=1}^{4} w_j \cdot k_{j,i} \\ k_{j,i} &= h \cdot f\left(t_j, y_i + \frac{t_j - x_i}{h} \cdot k_{j-1,i}\right), \quad j = 1, \ldots 4, \quad k_{0,i} = 0. \end{aligned} \tag{5.20}$$

in which w_j are the (symmetrical) weights, t_j being the nodes on the specific interval (basically nodes of between the two nodes), and $k_{i,j}$ are defined as the slopes at different positions of the interval: k_1 is the slope of y at t_i (which is x_i) and is determined with Euler's method; k_2 is the slope at the midpoint t_2 (which is $x_i + \frac{h}{2}$) using k_1; k_3 is again the slope at the midpoint t_3 (which is $x_i + \frac{h}{2}$) but now using k_2; and k_4 is the slope at the endpoint t_4 (which is $x_i + h$) of the interval. The weights 1 to 4 are symmetric and defined as $\frac{1}{6}$, $\frac{1}{3}$, $\frac{1}{3}$, and $\frac{1}{6}$, respectively. To chose the optimal step size, $h \cdot L$ should lie between 0.05 and 0.20 (L being the interval size). This step size is allowed to change for each step. As can be seen, the Classical Runge-Kutta method is computationally much more intensive than Euler's method. The above mentioned method solely yields the explicit Runge-Kutta method, which region of stability is small. This means that if the ODE to be solved is stiff, the explicit Runge-Kutta method, might not converge. In such a case, one might chose to decrease the step size, switch to the implicit Runge-Kutta method (which region of stability is larger), or switch to a whole different method all together (like the backwards Euler). Whether this method is worth it, is up to the user to decide.

5.3.6. DASSL

The engine model of the APPU consists out of algebraic equations and out of differential equations. Most notably, the accumulation of mass and energy in the combustion chamber and the accumulation of momentum in the shafts. Some simplifications are made by neglecting the accumulation of mass, energy and momentum in the compressors and turbines. Solving the APPU engine model is then a matter of solving systems of DAE's.
One of the most popular DAE solvers is the DASSL solver, developped by Petzold in 1982 [46]. DASSL (Differential-algebraic system solver) provides a numerical solver of implicit system of differential-algebraic equations. These equations are in the form of

$$\mathbf{F}(t, \mathbf{y}, \mathbf{y'}) = 0 \tag{5.21}$$

The solver can handle equations that are much more complex than ODE systems of the form $y' = f(t, y)$. DASSL can be used to solve two classes of problems:

- Equations for which it is impossible to solve **y'** explicitly, when $\frac{\delta \mathbf{F}}{\delta y'}$ is singular, for example.
- Equations for which it is impractical to solve **y'** explicitly, in which A**y'** = B**y** is solved by multiplying both sides with the inverse matrix A^{-1}. If matrix A is sparse, it doesn't necessarily imply that the inverse matrix A^{-1} will be sparse as well. In such a case, it could be better to solve the equations in their original form.

The method DASSL uses to solve Equation 5.21, is as follows:

- The derivative in Equation 5.21 is approximated by backward differentiation of the k^{th} order, in which k can vary from 1 to 5. The value that k takes varies each time step and is determined using an algorithm. If k = 1, one speaks of the Backward Euler, as previously described, and Equation 5.21 becomes [47]:

$$F\left(t_n, y_n, \frac{y_{n+1} - y_n}{\Delta t_n}\right) = 0 \tag{5.22}$$

  - if k = 1:

$$y_{n+1} - y_n = hf\left(t_{n+1}, y_{n+1}\right)$$

  - if k = 2 :

$$y_{n+2} - \frac{4}{3}y_{n+1} + \frac{1}{3}y_n = \frac{2}{3}hf\left(t_{n+2}, y_{n+2}\right)$$

  - if k = 3 :

$$y_{n+3} - \frac{18}{11}y_{n+2} + \frac{9}{11}y_{n+1} - \frac{2}{11}y_n = \frac{6}{11}hf\left(t_{n+3}, y_{n+3}\right)$$

  - if k = 4 :

$$y_{n+4} - \frac{48}{25}y_{n+3} + \frac{36}{25}y_{n+2} - \frac{16}{25}y_{n+1} + \frac{3}{25}y_n = \frac{12}{25}hf\left(t_{n+4}, y_{n+4}\right)$$

  - if k = 5 :

$$y_{n+5} - \frac{300}{137}y_{n+4} + \frac{300}{137}y_{n+3} - \frac{200}{137}y_{n+2} + \frac{75}{137}y_{n+1} - \frac{12}{137}y_n = \frac{60}{137}hf\left(t_{n+5}, y_{n+5}\right)$$

- Subsequently, to solve Equation 5.22, the Newton-Raphson method is applied:

$$x_{m+1} = x_m - \frac{f(x_m)}{f'(x_m)} \tag{5.23}$$

  such that Equation 5.22 becomes:

$$y_n^{m+1} = y_n^m - \left(\frac{\partial F}{\partial y'} + \frac{1}{\Delta t_n}\frac{\partial F}{\partial y}\right)^{-1} F\left(t_n, y_n^m, \frac{y_{n+1}^m - y_n}{\Delta t_n}\right) \tag{5.24}$$

  This same calculation can be done with any other k in the range from 1 to 5.

5.4. APPU model in Dymola

As previously discussed, it has been decided to make make the model in Dymola, as it is more versatile and allows the addition of heat exchangers, extra bottoming- and topping- cycles and including the sensible enthalpy of the fuel flow going into the combustion chamber. The Dymola model however, has to be made from the ground up, using existing sub-models from available Modelica packages. The following provided packages were used:

- BasicAeroEngines (a package that provides models to simulate engines, provided by the TU Delft [1])

[1] Personal correspondence with Dr. Ir. C. De Servi

- ThermoPower (a package for the dynamic modelling of thermal power plants and energy conversion systems, provided by Politecnico di Milano [2])
- ORC (a package that provides models for modelling Organic Rankine Cycles, provided by the TU Delft [3])
- ExternalMedia (a package based on coolProp provided by F. Casella, J. Wronski, F. Tarraneo [48])
- Modelica Standard Library (provided by Dymola)

The BasicAeroEngines package consists out of different models, relating to the engine components, a few of the important models are mentioned below and further explained in the following subsections. A lay-out of the APPU engine can be observed in Figure 5.1, while the individual sub-models can be observed in Figure C.1.

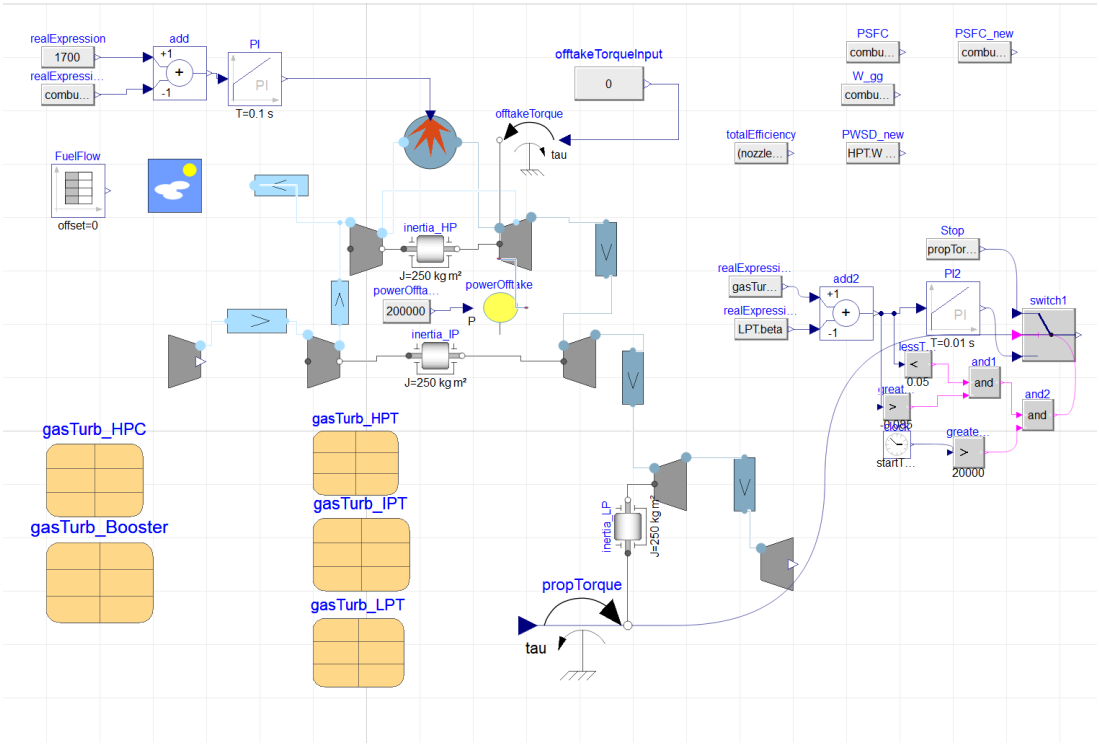

Figure 5.1: Baseline (without HEX) APPU Model in Dymola

5.4.1. Environment

This model is an outer model providing environmental conditions, such as ambient- pressure and temperature, furthermore it provides the Mach number at which the system moves, which is used to calculate the stagnation properties of the state. This model is used in components that are in contact with the boundaries of the system, such as the Air Intake Model and the Nozzle Model. The environment temperature and pressure are calculated by the ISA-equations:

$$T = T_b + T_{lr} \cdot (H - H_b) \tag{5.25}$$

In which T_b, T_{lr}, H and H_b are the base temperature at sea-level (fixed at 288.15 K), temperature lapse rate, altitude and the base altitude (fixed at 0m), respectively.

$$P = P_b \cdot (T_b / T)^{g \cdot M/(R \cdot T_{lr})} \tag{5.26}$$

In which P_b, g, M and R are the base pressure (fixed at 101325 Pa), acceleration of gravity (fixed at 9.80655 m/s^2), molar mass of the air (fixed at 0.0288 kg/mol) and gas constant of air (fixed at 288.2 $J/kg \cdot K$), respectively. The total enthalpy is then calculation with:

$$h_t = h + v/2 \tag{5.27}$$

In which h and v are the enthalpy and the velocity of the air, respectively. The velocity is calculated from the Mach number, which is a parameter of the model.

[2] Idem
[3] Personal correspondence with Dr. Ir. De Servi; created by F. Casella

5.4.2. Air Intake

This model calculates the drag by means of the momentum flux, furthermore, this model provides the mechanical power input by means of calculating the kinetic power entering the intake.

$$W = f \cdot v^2/2 \tag{5.28}$$

$$D = f \cdot v \tag{5.29}$$

In which f is the mass flow in kg/s.

5.4.3. Compressor Maps

Compressor- and turbine maps are an integral part of predicting the performance of an engine. These maps contain four variables: compression (or expansion) ratio, $\frac{P_2}{P_1}$; corrected mass flow, $\frac{\dot{m}\cdot\delta}{\sqrt{\theta}}$; corrected spool speed, $\frac{N}{\sqrt{\theta_{25}}}$; and efficiency, η. Given a corrected spool speed and a corrected mass flow, the pressure ratio can be calculated, as well as the efficiency of the component. For illustration of a compressor map has been generated from GasTurb, visible in Figure 5.2, the red line indicates the surge line and where the graph stops on the bottom side, indicates the choke. There is a fifth 'dummy variable', called β. This variable doesn't have a physical meaning, rather it helps the simulator to find the appropriate value where to spool speed curves are nearly vertical or horizontal. As can be seen in Figure 5.3, at high corrected mass flow, the corrected spool speed becomes nearly vertical, while at low corrected mass flows, the corrected spool speed becomes almost horizontal. If the solver tries to find a pressure ratio for a certain corrected mass flow at a high corrected spool speed, multiple solutions would be possible, due to the corrected spool speed line being vertical. By introducing beta-lines, the solver knows which pressure ratio it should solve for.

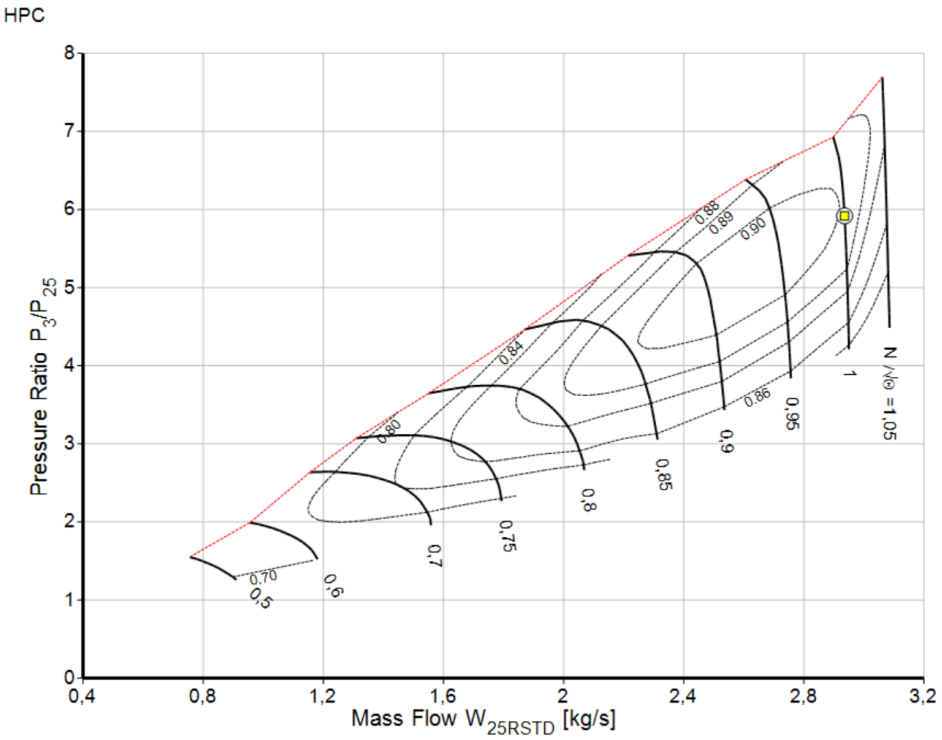

Figure 5.2: HPC compressor map (own work, using GasTurb)

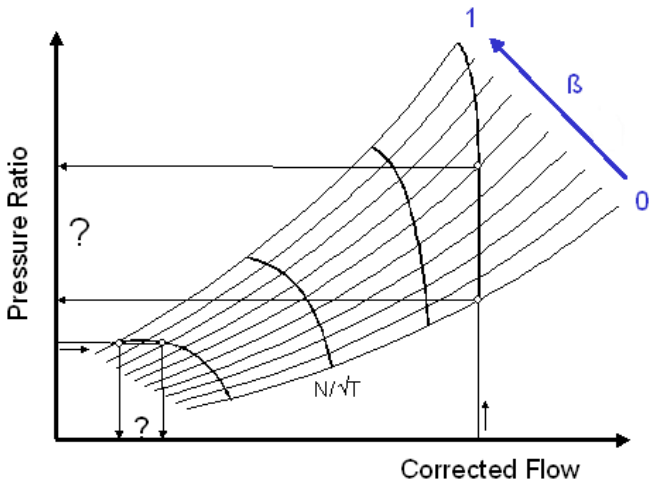

Figure 5.3: Beta lines [15]

To transfer the parameters and inputs from GasTurb to Dymola, some work has to be done on maps. Although different compressor and turbine maps are available, it has been decided to use the same maps from GasTurb in Dymola, in an effort to keep both GasTurb and Dymola models as close to each other as possible. This is done by using the raw map data from GasTurb and convert the data into a format Dymola is able to comprehend. The maps in GasTurb give data for the corrected mass flow, efficiency and pressure ratio at different corrected spool speeds at different beta-values. These spool speeds come at different step sizes and at different counts, depending on the specific map. The booster map for example has 9 different instances where the corrected spool speed is defined, while the HPT only has 5 different instances. The step sizes of these corrected spool speeds are may be variable within the same map, these values might follow a path of: 0.8, 0.9, 1.0, 1.05, 1.1, as is the case in the HPT map. On the other hand, the beta-values within a map do not change, and its step size is constant. The HPC map for example, has 20 beta lines which are equidistant, meaning that on a scale from 0 to 1 (starting at 0, and ending at 1) the beta-values follow a path of: 0, 0.053, 0.105, 0.158, etc. To make this more comprehensible, it has been decided to represent these beta-values as integers when converting the maps into Dymola. In the case of the HPC beta-values, this comes down to a row of 0 till 19. The map data can be found in Appendix B.

5.4.4. Compressor

This model uses mass- and energy balance equations, together with auxiliary equations which use *compressor maps* to calculate pressure (compression) ratio, spool speed, mass flow and consequently the thermodynamic state of the compressor outlet. The input parameters are the reference values of the compressor map, which are defined at the design point of the compressor, these are: reference- inlet- and outlet pressure, inlet temperature, isentropic efficiency, inlet mass flow, spool speed and beta value. The inlet- and outlet boundary conditions of this model entail the total enthalpy, pressure and mass flow. The mechanical boundary condition is connected to the shaft which dictates the spool speed and the torque entering the model. The energy balance is defined as:

$$W = f_E \cdot (h_L - h_E) \tag{5.30}$$

In which the subscript E and L indicate the entering and leaving conditions, respectively. The mechanical work input is calculated with:

$$W = \omega \cdot \tau \tag{5.31}$$

In which ω and τ indicate the spool speed and the torque, respectively.
Using the compressor map, the *nominal*- pressure ratio, efficiency, mass flow and spool speed can be calculated. The nominal- mass flow, pressure ratio and efficiency, defined as ϕ_{nom}, PR_n and η_n, respectively, are a function of both the beta-value β and the nominal spool speed N_n. The appropriate values are calculated using bilinear interpolation in the accompanied map.
The balance equations in the compressor model are defined as follows:

$$PR = P_L / P_E \tag{5.32}$$

$$PR_n = \frac{PR}{P_{L,nom} / P_{E,nom}} \tag{5.33}$$

$$\eta = \frac{h_{iso} - h_E}{h_L - h_E} \tag{5.34}$$

$$\eta_n = \frac{\eta}{\eta_{nom}} \tag{5.35}$$

$$\phi_n = \frac{f_E \cdot \sqrt{T_E}/P_E}{f_{nom} \cdot \sqrt{T_{E,nom}}/P_{E,nom}} \tag{5.36}$$

$$N_n = \frac{\omega/\sqrt{T_E}}{\omega_{nom}/\sqrt{T_{E,nom}}} \tag{5.37}$$

In which h_{iso} is the amount of enthalpy during isentropic compression. These equations calculate the new nominal variables, and thermodynamic variables for each time step.

5.4.5. Combustor

This model uses the conservation equations of mass-, energy and species, an input parameter that takes into account the lower heating value of the fuel, and the combustor efficiency to calculate the added heat and thermophyscial state properties at the outlet. It should be kept in mind that this model has a control volume, in which mass and energy accumulates, as a consequence the model contains differential equation, making the combustor model inherently dynamic. The conservation equations are defined as follows:

$$\frac{\mathrm{d}M}{\mathrm{d}t} = f_E + f_{E,fuel} - f_L \tag{5.38}$$

$$\frac{\mathrm{d}E}{\mathrm{d}t} = f_E \cdot h_E - f_L \cdot h_L + Q \tag{5.39}$$

$$Q = LHV \cdot f_{E,fuel} \cdot \eta_{comb} \tag{5.40}$$

$$X_L[1] = 1 - X_L[2] - X_L[3] - X_L[4] \tag{5.41}$$

$$\frac{\mathrm{d}(M \cdot X_L[2])}{\mathrm{d}t} = f_E \cdot X_E[2] - f_L \cdot X_L[2] - a_{stoich} \cdot f_{E,fuel}/M_{fuel} \cdot M_{O2} \tag{5.42}$$

$$\frac{\mathrm{d}(M \cdot X_L[3])}{\mathrm{d}t} = (-f_L \cdot X_L[3]) + ZH/2 \cdot f_{E,fuel}/M_{fuel} \cdot M_{H2O} \tag{5.43}$$

$$\frac{\mathrm{d}(M \cdot X_L[4])}{\mathrm{d}t} = (-f_L \cdot X_L[4]) + ZC \cdot f_{E,fuel}/M_{fuel} \cdot M_{CO2} \tag{5.44}$$

$$a_{stoich} = ZC + ZH/4 \tag{5.45}$$

X is a column vector that takes into account the different species in the flue gas. The allowed species are 4: N_2, O_2, H_2O and CO_2. This vector is used to calculate the thermophysical properties of the gas. a_{stoich}, ZH and ZC are defined as the stoichiometric ratio of the fuel combustion, the number of hydrogen and carbon atoms in the chemical formula of the fuel.
The amount of energy that enters the system Q is calculated by multiplying the lower heating value (LHV) of hydrogen with the fuel flow. However, in reality the lower heating value is a function of the temperature: at lower temperatures of hydrogen, the LHV will decrease, while it increases at higher temperatures. To make the model more accurate and to include the effect of the hydrogen heating up, the combustor model is altered by replacing Equation 5.39 and Equation 5.40 with Equation 5.46. Both models will be analysed and will be labeled as "*with changing LHV*" and "*without changing LHV*". A visualisation of the fuel flow going through a heat exchanger and feeding into the combustor while changing the LHV of the fuel can be observed in Figure 5.4. The Dymola model without fuel feedback will be initiated with a LHV of hydrogen 119.961 MJ/kg (which is the LHV of hydrogen without taking into account the specific enthalpy of the hydrogen).

$$\frac{\mathrm{d}E}{\mathrm{d}t} = f_E \cdot h_E - f_L \cdot h_L + f_{E,fuel} \cdot h_{E,fuel} - h_{fuel}/M_{fuel} \cdot \eta_{comb} \cdot f_{E,fuel} \tag{5.46}$$

The right-hand side in Equation 5.46 takes into account the amount of energy that enters (and leaves) the combustion chamber per time. The $f_E \cdot h_E$ indicates the amount of energy per second that enters the combustion chamber via the HPC, while $f_L \cdot h_L$ indicates the amount of energy per second that leaves the combustion chamber. The $f_{E,fuel} \cdot h_{E,fuel}$ is the amount of energy per second coming from the fuel that enters the combustion chamber. $h_{E,fuel}$ is dependant on the temperature of the fuel. This means that the amount of energy in the system increases if the temperature of the fuel is increased. Lastly, h_{fuel} is the enthalpy of formation of the fuel, which for hydrogen is assumed to have a constant value of -241.826 kJ/mol [35]. Furthermore the constitutive equations are defined in Equation 5.47, Equation 5.48 and Equation 5.49.

$$M = \rho \cdot V \tag{5.47}$$

$$E = u \cdot M \tag{5.48}$$

In which u is the specific internal energy. The outlet pressure is calculated by:

$$P_E = P \cdot (1 - P_{Loss}/100) \tag{5.49}$$

In which P_{Loss} is the pressure loss during the combustion in %. Solving the system of equations Equation 5.38 up to Equation 5.49 together with the boundary conditions (P, f, h and X) gives the thermodynamic state variables leaving the combustor.

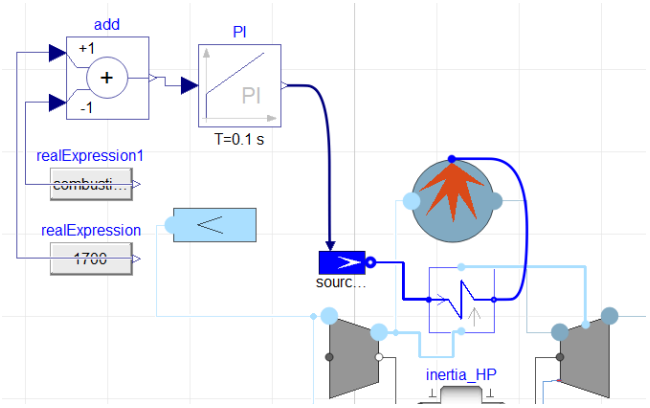

Figure 5.4: Hydrogen flowing through the HEX and subsequently entering the combustor, changing its enthalpy (and LHV) on the way

5.4.6. Turbine

This model does essentially the same as the compressor model, but uses turbine maps instead of compressor maps for the calculation of the pressure (expansion) ratio, mass flow and efficiency. This means that Equation 5.31 up to Equation 5.37 are used in this sub-model as well. In addition, a new balance equation is added:

$$\boldsymbol{X_E = X_L} \tag{5.50}$$

Furthermore, a new turbine model has been created that:

- Allows a power off-take to take into take into account the power that is needed to feed the electronics of the aircraft system.
- Adds another Air Port to the submodel that allows bleed flow to enter the system to cool multiple turbine stages. The amount of bleed that goes to the stator blades and the rotor blades can be set independently.

As bleed cooling is allowed, this changes the balance equations of the submodel.

$$f_E + \sum f_{bl} = f_L \tag{5.51}$$

$$W = f_E \cdot (h_E - h_L) + \sum f_{bleed} \cdot (\boldsymbol{h_{L,bleed}} - \boldsymbol{I} \cdot h_L) \tag{5.52}$$

In which **I** indicates the identity matrix of $N \times N$ with n being the amount of bleed air supplies and $h_{L,bleed}$ indicates the amount of specific enthalpy of each bleed air supply.
The turbine model that doesn't allow bleed (such as the IPT and the LPT), Equation 5.52 and Equation 5.54 become Equation 5.53, respectively.

$$W = f_E \cdot (h_E - h_L) \tag{5.53}$$

$$f_E = f_L \tag{5.54}$$

5.4.7. Propeller Torque off-take

The APPU engine has a propeller that uses mechanical work and converts in into thrust. It is not strictly necessary to model the propeller, as the main interest lies in the thermodynamics of the system. Instead of a propeller model that uses propeller maps and accurately predicts the amount of thrust, the propeller can be replaced by torque source. A torque source can take off a specified amount of torque. This can be specified manually, or with the help of a PI-controller as is mentioned in Subsection 5.4.10. The torque source is connected to the Shaft Inertia model, which is connected to the LPT.
However, for the sake of completeness, the propeller is modeled in Dymola with the use of propeller maps. The amount of force and power that the propeller is able to deliver depends on the blade (pitch) angle and the rotational

velocity of the propeller. The rotational velocity is dictated by a gear ratio that connects the LPT with the propeller spool.
The system of equations that is solved in the propeller submodel are given in Equation 5.55 up to Equation 5.60 [45]. In which n is the amount of rotations *per second* and d is the diameter, which is fixed at 2.4 m [49]. The advance ratio J, the power coefficient C_P and the efficiency η are calculated with a propeller map, using bilinear interpolation. The force coefficient C_F can be calculated through the advance ratio and the power coefficient in Equation 5.58.

$$W = \omega \cdot \tau \tag{5.55}$$

$$C_P = \frac{W}{\rho\, n^3\, d^5} \tag{5.56}$$

$$n = \frac{\omega}{2\pi} \tag{5.57}$$

$$\eta = \frac{C_F \cdot J}{C_P} \tag{5.58}$$

$$F = C_F \cdot \rho \cdot n^2 \cdot d^4 \tag{5.59}$$

$$J = \frac{V}{n \cdot d} \tag{5.60}$$

As the advance ratio is a function of the aircraft velocity, at *take-off*, this value will always be zero, which would lead to an efficiency (and thus a thrust) of zero. In reality however, the propeller is able to generate thrust at take-off. Therefore, another force coefficient is needed to accurately calculate the thrust during take-off. This variable is called the 'static force coefficient' and is defined in Equation 5.61 [45], which the model initiates if the aircraft velocity is less than 70 m/s. $C_{F_{stat}}$ is calculated using a propeller map.

$$F = C_{F,stat} \cdot \frac{W}{n \cdot d} \tag{5.61}$$

If the amount of torque that is taken off is increased, the amount of work that the LPT has to provide also increases, as can be seen in Equation 5.31. This means that $h_E - h_L$ has to increase, as f_E is conserved through the entire engine. As h_E of the LPT is dictated by the outlet of previous sub-model (IPT), the only variable that is allowed to change is h_L. This means that if the propeller requires a higher power, the leaving enthalpy of the LPT has to decrease, which means that the flow in the LPT has to expand more. This subsequently means by increasing the propeller torque, the air velocity that leaves the nozzle will be decreased.
An accurate value for the nozzle exhaust velocity has to be found, which will determine the amount of power the propeller is able to take off. If the nozzle exhaust velocity decreases, the amount of thrust generated by the nozzle will decrease, while the amount of thrust generated by the propeller will increase, due to the increased amount of work available. This means that there will be an optimal value for the exhaust velocity. The optimum power split between the propeller and the nozzle can be calculated by Equation 5.62 as derived by Farokhi [40]. The optimum is defined as the point in with the maximum amount of specific thrust (thrust per mass flow).

$$\alpha_{\text{opt}} = 1 - \frac{\eta_{\text{n}}}{\left(\eta_{\text{PT}}\eta_{\text{mLPT}}\eta_{\text{gb}}\eta_{\text{prop}}\right)^2} \cdot \frac{\gamma_{\text{c}} - 1}{2} \frac{M_0^2}{\tau_{\text{HPT}}\tau_\lambda \left[1 - \left(\frac{p_9/p_0}{\pi_{\text{r}}\pi_{\text{d}}\pi_{\text{c}}\pi_{\text{b}}\pi_{\text{HPT}}}\right)^{\frac{\gamma_{\text{t}}-1}{\gamma_{\text{t}}}}\right]} \tag{5.62}$$

In which α_{opt}, η_n , η_{PT}, η_{mLPT}, η_{gb}, η_{prop}, τ_{HPT}, τ_λ, π_r, π_d, π_c, π_b, γ_c, γ_t and p_9 are defined as the optimal power fraction going to the propeller, adiabatic efficiency of the nozzle, isentropic efficiency of the LPT, mechanical efficiency of the LPT, gear box efficiency, propeller efficiency, HPT pressure ratio, cycle limit enthalpy ratio, static-stagnation pressure ratio, inlet pressure ratio, compressor pressure ratio, combustor pressure ratio, heat capacity ratio in the compressor, heat capacity ratio in the turbine and the nozzle outlet pressure, respectively. In which τ_λ is calculated with Equation 5.63.

$$\tau_\lambda = \frac{c_{p,t} \cdot T_{t,4}}{c_{p,c} \cdot T_{t,0}} \tag{5.63}$$

In which $c_{p,c}$ and $c_{p,t}$ are the specific heat capacities in the compressor and the turbine, respectively. For the sake of simplicity, the isentropic nozzle efficiency is taken to be 1 and it is assumed that the nozzle expands perfectly to the ambient; this leads to:

$$\alpha_{\text{opt}} = 1 - \frac{1}{\left(\eta_{\text{PT}}\eta_{\text{mLPT}}\eta_{\text{gb}}\eta_{\text{prop}}\right)^2} \cdot \frac{\gamma_{\text{c}} - 1}{2} \frac{M_0^2}{\tau_{\text{HPT}}\tau_\lambda \left[1 - \left(\frac{1}{\pi_{\text{r}}\pi_{\text{d}}\pi_{\text{c}}\pi_{\text{b}}\pi_{\text{HPT}}}\right)^{\frac{\gamma_{\text{t}}-1}{\gamma_{\text{t}}}}\right]} \tag{5.64}$$

Having calculated the optimum power fraction that goes to the propeller, the optimal nozzle exhaust velocity can be

calculated with Equation 5.65 [40].

$$V_9 \approx \sqrt{2(1-\alpha)\eta_n h_{t4.5}\left[1-\left(\frac{p_9}{p_{t4.5}}\right)^{\frac{\gamma_t-1}{\gamma_t}}\right]} \tag{5.65}$$

In which station 4.5 is the station at the IPT outlet.
The propeller efficiency η_n is calculated by via a propeller map, provided by Gas-turbine Simulation Program (GSP). The propeller blade angle at cruise is fixed at 56.63°, as mentioned in the final APPU report [49] and rotational velocity is given a value such that the nozzle outlet velocity corresponds with Equation 5.65. At cruise, this gives a steady-state propeller efficiency of 80.3 %, which is in accordance with calculations done by Farokhi [40] and is mentioned by Raymer as an accurate value [50]. The propeller blade angle at take-off is fixed at 20°and the rotational velocity is fixed such that the torque that is taken off from the LPT causes the it to be at design spool speed. At take-off, the propeller efficiency is around 57%, which is a bit lower than the value of 0.65, as mentioned by Rodgers [51].

5.4.8. Nozzle

This model calculates the outlet velocity and nozzle area if the mass flow is fixed. Furthermore, the generated thrust and power are calculated using the velocity and the thermodynamic states of the outlet (the ambient) and the inlet. On the other hand, the mass flow can be calculated if the nozzle area is kept fixed, however, this affects the mass flow through the entire system, and subsequently alters the design point on the compressor and turbine maps.
The inlet conditions (P, h, X) are provided by the leaving conditions of the turbine outlet. The outlet pressure is the same as the ambient pressure and the outlet composition is the same as the inlet. The leaving enthalpy and velocity are calculated with Equation 5.66 and the isentropic relations, given the pressure ratio.

$$h_E = h_L + v^2/2 \tag{5.66}$$

The nozzle area can be calculated through Equation 5.67.

$$f_E = \rho_E \cdot v \cdot A \tag{5.67}$$

The thrust and work are calculated by Equation 5.68 and Equation 5.69, respectively.

$$F = f_E \cdot v \tag{5.68}$$

$$W = f_E \cdot v^2/2 \tag{5.69}$$

In case of comparing the system performance, important variables are the Power Specific Fuel Consumption (PSFC) and the thermal efficiency (η_{th}). These variables are calculated with Equation 5.70 and Equation 5.71, respectively.

$$PSFC = \frac{\dot{m}_{fuel}}{W_{prop} + W_{nozzle}} \tag{5.70}$$

$$\eta_{th} = \frac{\frac{1}{2}\cdot \dot{m}_{nozzle}\cdot (V^2_{nozzle} - V_0^2) + W_{prop}}{\dot{m}_{fuel}\cdot LHV} \tag{5.71}$$

In which W_{nozzle} is defined in Equation 5.69. In which V_0 is the velocity of the aircraft. This means that the thermal efficiency and PSFC are more or less inversely related, with a note that the thermal efficiency also takes into account the aircraft speed, while the PSFC does not.

5.4.9. Shaft Inertia

This model uses the spool speed and the inertia of the spool to calculate the torque of the spool. The spool speed ω is calculated using the rotation angle Φ of the component.

$$\omega = \frac{\mathrm{d}\Phi}{\mathrm{d}t} \tag{5.72}$$

$$a = \frac{\mathrm{d}\omega}{\mathrm{d}t} \tag{5.73}$$

$$J \cdot a = \tau_a + \tau_b \tag{5.74}$$

In which J equals the inertia of the compressor and turbine, and τ equals the torque; a port that connects the shaft inertia sub-model with the compressor (a) and turbine (b).

5.4.10. PI controller

When each submodel has been connected with each other appropriately with suitable input parameters, the model uses DASSL to find a solution. If the spool speed ratio is kept constant, this means that in each of the compressor and turbine maps, appropriate pressure-, mass and efficiency ratios are tried to be found that closes the system of equations. This however, means that the beta-value is a free variable. If the beta-value changes too much, it is possible that the appropriate operating point lies out of bounds. To counter this, a PI-controller has been introduced.
The LPT is connected to the propeller which has been modelled as a Torque Source. The amount of torque that is taken off by the propeller is calculated with a PI-controller. The inputs of the PI-controller are the actual beta-value of the LPT and the design beta-value. This means that the PI controller calculates the required torque to be taken off by the propeller such that the beta-value of the LPT stays as close as possible to its design point.

5.5. Heat Exchanger in Dymola

The ORC package consists out of models needed to model Organic Rankine Cycles, one of those models is the Heat Exchanger Model. The ORC package provides multiple heat exchangers: a simpler heat exchanger that allows two liquids to exchange heat through a wall, and another (more sophisticated) model that allows a liquid inflow and a 2-phase (either gas or liquid, or a combination of those) inflow. It allows different media mass flows at different temperatures and pressures as input, after which heat is transferred through the wall of the heat exchanger, after which the both mass flows exit the heat exchanger with a different temperature.
The entering mass flows are described with the following parameters:

- Medium, which includes:
  - Saturation properties of a two phased medium, such as the saturated pressure and temperature.
  - Critical and triple points of the fluid.
  - Base properties (density (ρ), pressure (P), enthalpy (h), internal energy (u), temperature (T), molar mass (MM) and mass fraction (X_i/X), if applicable. Certain variables will be given, after which the rest of the variables will be calculated.
  - Dynamic viscosity (μ).
  - Thermal conductivity (k).
  - Prandtl Number (Pa).

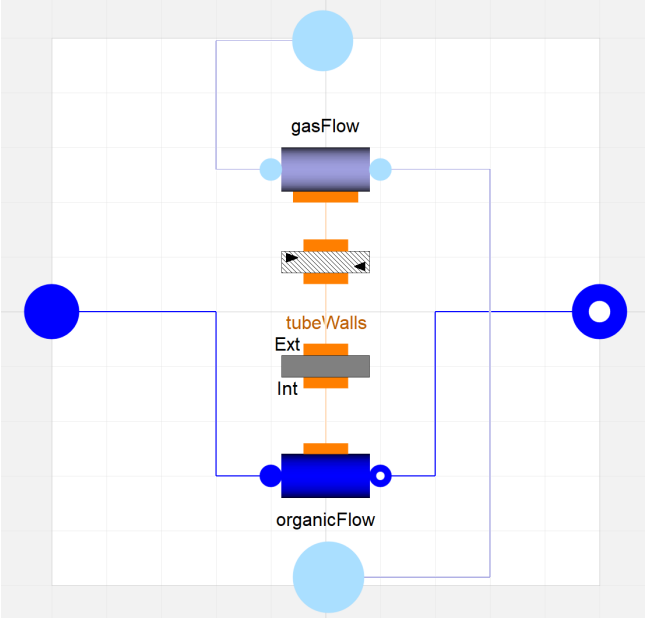

Figure 5.5: Sub-models that comprise the heat exchanger

Figure 5.5 shows the sub-models of the heat exchanger that is shown in Figure C.1g. The model allows the user to set different parameters such as the heat transfer surface on both the hot and the cold sides, the mass and the specific heat capacity of the (metal) wall between the two fluids, the fluid medium of both fluids, the volume of the fluids on both sides and the amount of nodes N in the heat exchanger. These nodes divide the fluid model in multiple volumes to calculate the heat transfer Q and the temperature T on. The model consists out of:

- A 1-dimensional fluid flow model that has been altered to allow any substance of that is provided by the Modelica library *and* the External Media package (of which cryogenic hydrogen).
  - The fluid inside this model can be a one-phase or a two-phase mixture.
  - If a two-phase flow is initiated, the model will be homogeneous as the same velocity as assumed for both phases.
  - The velocity is assumed to be uniform on the cross-sectional plane.
  - Turbulent friction is assumed.
  - The conservation equations are dynamic, which means that the model has a system of differential equations.
  - Longitudinal heat diffusion is not taken into account.
  - The energy conservation equation is calculated assuming a uniform pressure distribution; the pressure drop is lumped either at the inlet or the outlet.
  - The fluid flow can exchange heat through the lateral surface which has to be connected to a 'heat transfer model'.

  The boundary conditions of the model are the mass flow, pressure, specific enthalpy and mass fractions of the fluid which are used in the mass- and energy balance equations.
- A distributed heat terminal that allows the flow variable Q and the effort variable T to be passed on to the next sub-model.
- A finite volume 1D (metal) wall model that takes into account the heat capacity and thermal resistance using equation Equation 5.75.

$$\frac{C_{metal}}{\boldsymbol{N}} \cdot \frac{\mathrm{d}\boldsymbol{T_{vol}}}{\mathrm{d}t} = Q_{int} + Q_{ext} \tag{5.75}$$

  In which C_{metal}, $\mathbf{N}$, $\boldsymbol{T_{vol}}$ are the heat capacity, the number of volumes and the temperature of the volumes of the wall, respectively.
- A Heat Exchanger Topology model that allows the user to set the heat transfer model to either a co-current or counter-current flow.
- Another 1-dimensional fluid flow model that has been altered to allow the connection with the airflow from the BasicAeroEngines package.

5.6. Scaling

The scaling of maps is used due to the lack of experimental data of compressor/turbine maps. To still be able to make accurate calculations, existing maps are scaled. This basically means that the geometry of the compressor/turbine stays the same (which dictates the aerodynamic functions), but the sizing is altered. The sizing of these maps can be altered in such a manner that the maps give optimum values for the specified design point.

As the pressure ratio and efficiency of any gas compressor/turbine depend on a lot of variables (namely: $\dot{m}, D, a, \rho, \nu, R, \gamma, N$ and the geometric design of the machine), efforts are made to reduce the number of variables, making the analysis, and moreover the design of new gas compressors/turbines easier. This is done in two steps:

1. Making the variables independent of each other, such that when a certain variable is changed, it will not affect another variable, except for the pressure ratio and efficiency that is.
2. Making the variables dimensionless, such that comparison of different states will be more straightforward.

5.7. Determining the required bleed flow

As is well known within the community of aerospace engineering, high temperatures are encountered within the components of an engine. Within the compressors, the temperature rises due to the compression of air, but the highest temperatures are encountered in the combustion chamber and in the HPT, which is located right after the combustion chamber. Combustion chambers are made out of heat resistant material and is cooled in stages with bleed air. Combustion chamber design however, is outside of the scope of this research; the focus lies mainly on the HPT and its cooling.
To calculate the required bleed flow to the HPT, the designer should first have an idea on the maximum allowed turbine blade temperature. A higher maximum turbine blade temperature allows either:

- A higher turbine inlet temperature (having the same amount of bleed flow).

  - This results into a higher fuel flow to the combustion chamber, which results in a higher specific thrust.

- A lower bleed flow to the HPT to cool the blades down (having the same TIT).
  - This results into more core flow, which also results in a higher thermal efficiency and a lower PSFC.

For this research, the maximum turbine blade temperature is to be fixed. Commonly, nickel based chromium-cobalt super-alloys are used in turbine blades, as mentioned by Flack [52]. One of these super-alloy types commonly used in aero-engine turbine blades are the "Creep-Microscopically Stable eXperimental" or CMSX type, as mentioned, as mentioned by Okura in [53]. This alloy has a maximum operating temperature of 1618 K, while older Inconel alloys have a maximum operating temperature of around 1423 K [54]. For this study, the assumption is made that the turbine blades are to be made from a CMSX super-alloy. A safety margin of 10% is taken, meaning that the maximum blade temperature in the APPU should be fixed at 1456 K.
To calculate the amount of bleed air needed to cool the turbine, an empirical correlation is used [55].

$$\frac{\dot{m}_c \overline{c_{p,c}}}{\dot{m}_g \overline{c_{p,g}}} = b\left(\frac{T_g - T_b}{T_b - T_c}\right)^s \tag{5.76}$$

In which $\dot{m}_c$, $c_{p,c}$ and T_c are defined as the bleed mass flow, the *average* specific heat capacity of the bleed flow and the blade turbine temperature, and the temperature of the bleed flow, respectively; $\dot{m}_g$, $c_{p,g}$ and T_g are defined as the mass flow entering the HPT, the *average* specific heat capacity of the fluid entering the HPT and the blade temperature, and the turbine inlet temperature (TIT), respectively; T_b is defined as the blade temperature, while b and s are adjustable parameters. The parameter b should be between 0.05 and 0.1; for this study b is set to 0.06 for the NGV and to 0.05 for the rotor stage, while s is set at 1, as mentioned by Yin et al. [56].
The provided initial GasTurb model of the APPU had an initial bleed flow of 2% of the HPC mass flow to the NGV and 3% to the rotor stage. These values are to be replaced by solving for $\dot{m}_c$ in Equation 5.76. Before this can be done, reasonable values for $c_{p,c}$, T_c, $\dot{m}_g$, $c_{p,g}$ and T_g should be found. These values are calculated by simulating the APPU engine in Dymola, without bleed and without the use of a heat exchanger, while the specific heat capacities are calculated and averaged in coolProp [57]. As an illustration, these calculated values (at the hydrogen cruise baseline) can be found in Table 5.1.
Due to the introduction of a heat exchanger, T_c can be changed. If T_c drops, the amount of required mass flow decreases. The relation between required mass flow and the bleed air temperature can be observed in Figure 5.6, making use of Equation 5.76. Furthermore, the TIT temperature could be increased as much as the combustion chamber allows. This can be observed in Figure 5.8 which show the relation between the bleed temperature and the TIT (T_g in the graph) with respect to the mass flow of the bleed air. A similar trend holds for the rotor bleed.
As can be observed from Figure 5.7 and Figure 5.8, the higher the bleed temperature is, the more mass flow is required for the bleed, this increases exponentially, this can be observed from Figure 5.6 as well. Increasing the TIT however, increases the required bleed flow in an approximate linear fashion, as only T_g and $\overline{c_{p,g}}$ are increasing in Equation 5.76.
At a TIT of 1700 K, if the bleed air is not cooled, the NGV bleed should be 2.18% of the HPC outflow, while the rotor bleed should be 1.81%. While if the bleed air is cooled to a minimum (which is around 273.15 K, as at this point icicles will form which could damage the structure or the turbine blades), a NGV bleed of 1.38 % and a rotor bleed of 1.15% of the HPC outflow is required.

Table 5.1: Dymola outputs for simulation without bleed air and no heat exchanger

$\overline{c_{p,c}}$	T_c	$\dot{m}_g$	$\overline{c_{p,g}}$	T_g
1153.6	736	3.708	1218.2	1700

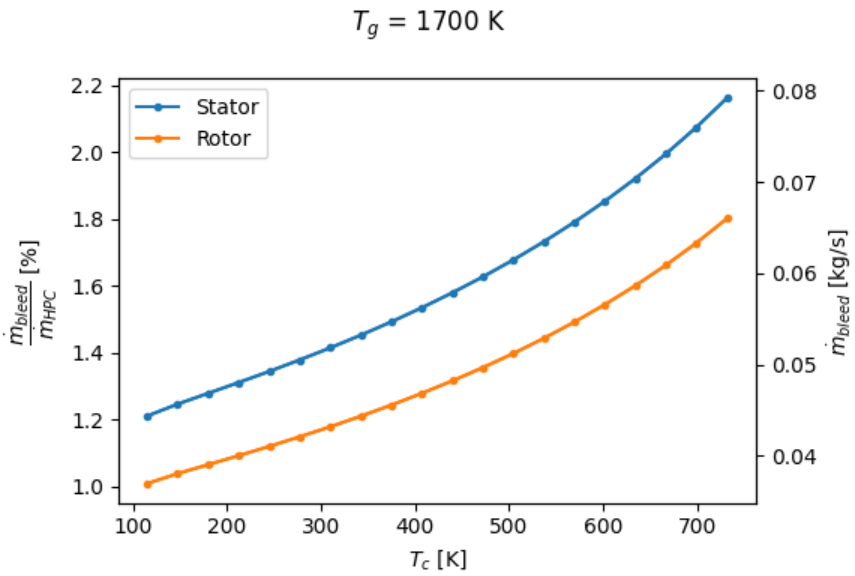

Figure 5.6: Relation of required bleed flow to bleed temperature at TIT = 1700 K (own work)

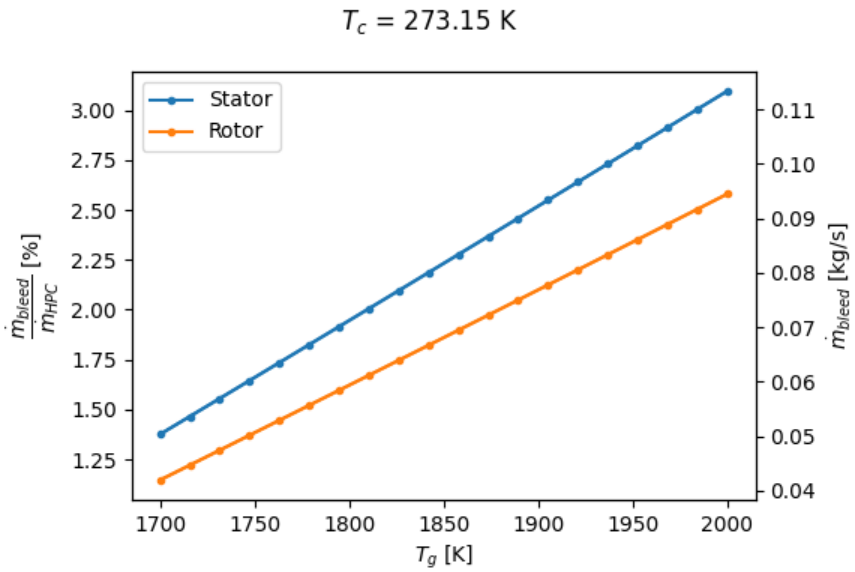

Figure 5.7: Relation of required bleed flow to turbine inlet temperature if T_c = 273.15 K (own work)

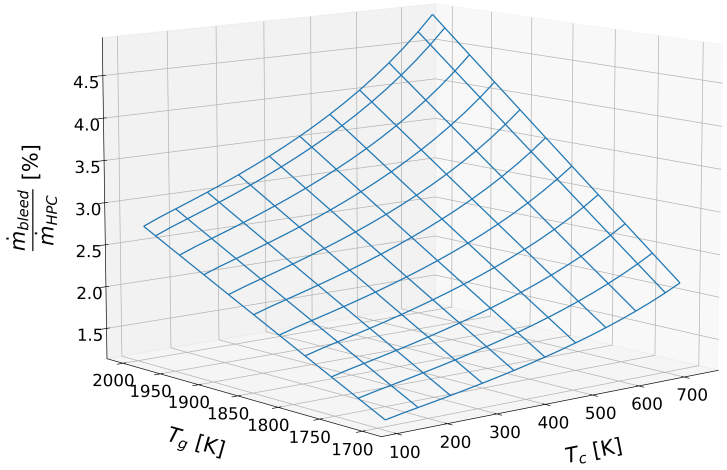

Figure 5.8: Required stator bleed air (own work)

5.8. Heat exchanger sizing

To design the geometry of the heat exchanger a few considerations have to be made. Should the heat exchanger have a high effectiveness, or should the heat exchanger be very compact; and where is the heat exchanger going to be installed?

The *bleed* heat exchanger will be small, as it only has to cool a very small amount of airflow. This means that it is relatively easy to integrate this heat exchanger into the engine system. Therefore, the bleed heat exchanger will be assumed to be of rectangular shape which can be installed at a convenient place. On the other hand, the *intercooling* heat exchanger has to cool a much larger amount of mass flow, which means that this heat exchanger should be placed *annularly* within the trajectory of the core flow.

If the effectiveness of the heat exchanger increases, the heat exchanger will be bulkier and heavier, as can be seen in Figure 5.13. Because mass is considered to be of greater importance than the heat exchanger's effectiveness, the decision has been made to focus on the compactness of the heat exchanger. In theoretical terms this means that the product of the heat transfer coefficient and the heat transfer surface on the air-side ($U_{air} \cdot A_{air}$), should be very close to the value on the hydrogen side ($U_{H2} \cdot A_{H2}$). This means that the amount of heat transfer that the hot air is able to give, is approximately equal to the amount of heat that the cold hydrogen is able to absorb. In this manner, the heat exchanger won't be over-designed on one side and under-design on the other.

Both these heat exchangers are designed using the Optimization package of Scipy. The objective function tries to minimise the relative difference between the thermal conductance on both sides.

$$\frac{|(U \cdot A)_{air} - (U \cdot A)_{H2}|}{(U \cdot A)_{H2}} \tag{5.77}$$

And is constrained by a simple inequality equation:

$$\frac{|(U \cdot A)_{air} - (U \cdot A)_{H2}|}{(U \cdot A)_{H2}} \leq 0.12 \tag{5.78}$$

The state variables are temperature, pressure and mass flow rate, which are defined by the heat exchangers inlet (either the booster outlet or the HPC outlet, depending whether the optimisation is conducted for the intercooling HEX or the bleed HEX, respectively) and outlet. The design variables for the rectangular heat exchanger are the width, depth and height (W, D and H). The annular heat exchanger however, has only two design variables, namely: the outer diameter

and the depth (r_o and D). The inner diameter equals 10.95 cm and is constrained by the height of the hub at the booster outlet, to avoid structural deviations on the hub.
Next, the bounds of the design variables have to be set. These bounds are defined as "common heat exchanger sizes" as provided by Carozza [17] and can be observed in Table 5.2

Table 5.2: Common heat exchanger sizes in aviation, from Carozza [17]

	Minimum	Maximum
Width [cm]	10	132
Height [cm]	2.5	132
Depth [cm]	1.9	31

The bounds of the intercooling heat exchanger, however are a little bit different. The depth of this heat exchanger has a lower bound of 1.9 cm and an upper bound of 61 cm. The outer radius however, has a lower bound of 12 cm (which is approximately 1 cm above the inner radius of the heat exchanger) and an upper bound of 50 cm.
A flowchart of the calculation process can be observed in Figure 5.9

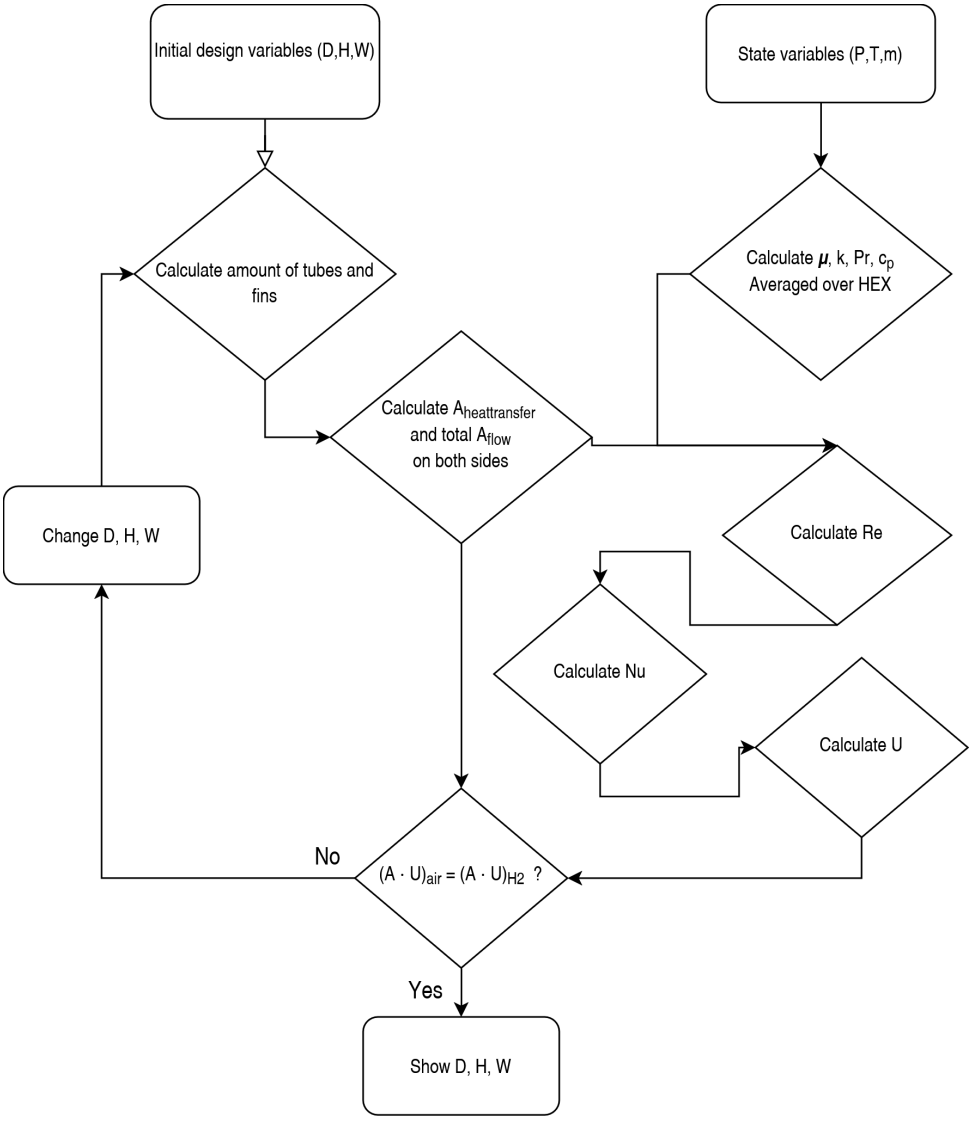

Figure 5.9: Flowchart of HEX optimisation

5.9. Impact of mass on the aircraft-level fuel consumption

Altering the APPU engine cycle to increase its performance by means of Simple Bleed Cooling, cooled bleed and increasing TIT, or intercooling and raising the pressure ratio, also comes with a drawback: an additional mass of the heat exchanger, which theory and methodology have been described in Section 4.4 and Section 5.8, respectively. This additional mass implies that the aircraft will additional lift which comes with more drag. This means that the aircraft thrust needs to be increased accordingly. To achieve a net benefit, the decreased fuel flow per amount of thrust (thrust

specific fuel consumption) of the altered APPU design should outweigh the additional fuel consumption that is caused by increasing the take-off mass.
This can be estimated as follows:

- The assumption is made that the increase in thrust is linearly proportional to the increase in maximum take-off mass.
$$T_{total} \propto MTOM \tag{5.79}$$
- To calculate the increased amount of thrust required, Equation 5.80 is used.
$$\Delta\%_{T_{total}} = 1 + \frac{m_{addition}}{MTOM} \tag{5.80}$$
- The useable hydrogen onboard is fixed. To provide an equal amount of thrust during the entirety of the cruise, the fuel flow has to stay constant to the baseline. This means, that a comparison has to be made with regards to thrust per fuel flow.
$$\Delta\%_{T/\dot{m}} = \frac{\left(\frac{T_{APPU}}{\dot{m}_{fuel}}\right)_{new} - \left(\frac{T_{APPU}}{\dot{m}_{fuel}}\right)_{baseline}}{\left(\frac{T_{APPU}}{\dot{m}_{fuel}}\right)_{baseline}} \tag{5.81}$$
In which $\dot{m}_{fuel}$ is the fuel flow. Equation 5.81 is basically a representation for the percentual increase in thrust of the altered APPU model.
- The thrust share of the APPU (Φ_{APPU}) is defined as the ratio between the APPU thrust and the total thrust. The baseline thrust share is $\Phi_{APPU} = 0.168$ as mentioned in the technical report of the APPU [49]. To calculate the increase in the thrust share of the APPU, the increased thrust of the altered design has to be divided by the new required thrust.
$$\Delta\%_{\Phi_{APPU}} = \frac{\Delta\%_{T/\dot{m}}}{\Delta\%_{T_{total}}} \tag{5.82}$$
- The new thrust share can then be calculated.
$$\Phi_{APPU,new} = \Phi_{APPU} \cdot (1 + \Delta\%_{\Phi_{APPU}}) \tag{5.83}$$
- The absolute difference in APPU thrust share is then:
$$\Delta\Phi_{APPU} = \Phi_{APPU,new} - \Phi_{APPU} \tag{5.84}$$
- Lastly, assuming that the thrust is linearly proportional to the fuel flow, the new fuel mass can be calculated by using Equation 5.85.
$$m_{f,new} = (1 - \Delta\Phi_{APPU}) \cdot m_f \tag{5.85}$$
In which m_f is the total amount of fuel required.

5.10. Cases

This section explains the alterations of the engine cycle of the APPU that are investigated. Three major alterations have been made, to increase the thermal efficiency of the engine cycle.
As the APPU engine is fuelled by hydrogen, which is stored at 20 K, injecting this cryogenic hydrogen directly into the combustor causes high thermal stresses in the combustor. This means that the hydrogen has to be heated up, prior to entering the combustion chamber. At the same time, the HPT blades need to be cooled. The heat sink of the cryogenic hydrogen can therefore be used as a means of cooling, while at the same time increasing its own temperature before entering the combustor. This leads to the first case: "Simple Bleed Cooling". The thermal efficiency is defined in Equation 5.86 [2].

$$\eta_{th,jet} = \frac{0.5 \cdot \dot{m} \cdot \left(v_j^2 - v_0^2\right)}{\dot{m}_{fuel} \cdot LHV} \tag{5.86}$$

Equation 5.86 is valid for jet turbines. For a turboprop however, the kinetic energy that the propeller adds to the system should be taken into account, converting Equation 5.86 to Equation 5.87.

$$\eta_{th,prop} = \frac{0.5 \cdot \dot{m} \cdot \left(v_j^2 - v_0^2\right) + W_{prop}}{\dot{m}_{fuel} \cdot LHV} \tag{5.87}$$

Furthermore, the PSFC is defined in Equation 5.88, which is inversely correlated to Equation 5.86

$$PSFC = \frac{\dot{m}_{fuel}}{W_{prop} + W_{nozzle}} \tag{5.88}$$

In literature the LHV value is often taken as a constant, this value is in reality however, a function of temperature.
To evaluate the variations in the thermal efficiency between the baseline and the modified engine cycles, the percentual difference is employed as the comparative metric. To provide an intuitive understanding of the extent to which engine cycle performance improves over the baseline, the LHV in Equation 5.86 is set constant to the LHV of the baseline.

5.10.1. Simple Bleed Cooling

Simple Bleed Cooling (SBC) is an alteration of the APPU system in which the liquid hydrogen is used to cool down the bleed air. In conventional engines, the bleed air that is used to cool the turbine blades is taken directly from the HPC, which means that conventionally the turbine blades are cooled with an air flow that has a temperature that is identical to the HPC temperature. In SBC however, the heat exchanger will be sized such that the bleed air will attain a temperature of approximately 273 K, as explained in Subsection 4.3.1. This results into a lesser required bleed flow to keep the turbine blades at a temperature of 1456 K, which consequently results into a higher core flow and an increased fuel temperature (meaning a higher LHV), which both contribute to a higher thermal efficiency, as can be observed in Equation 5.86.

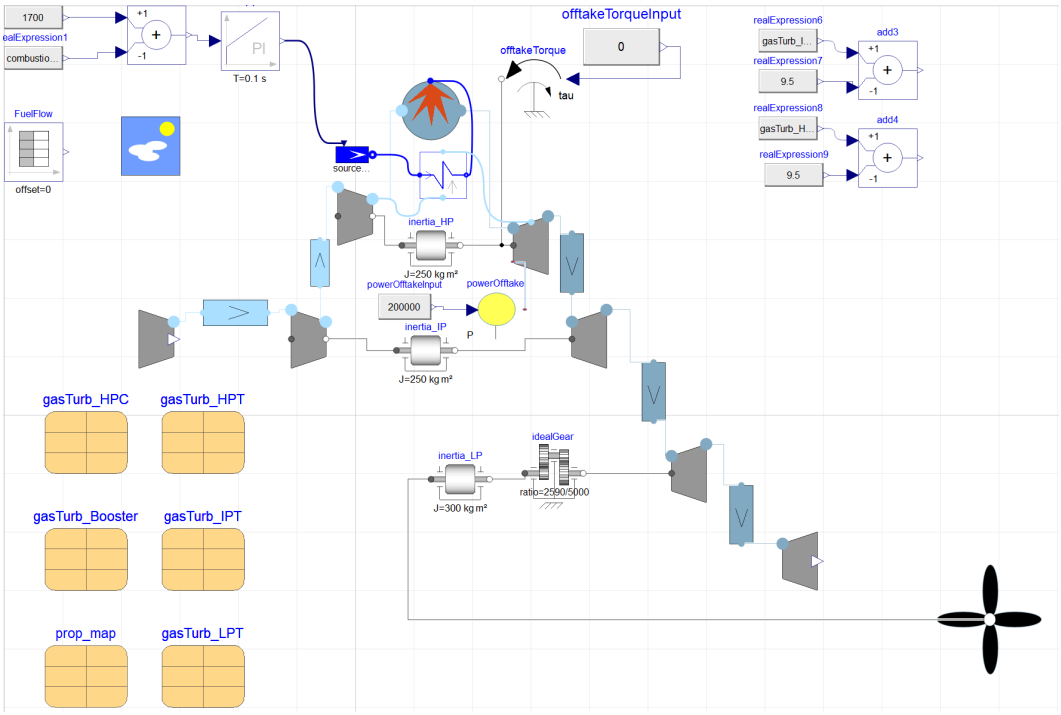

Figure 5.10: Visualisation of the Simple Bleed Cooling model in Dymola

5.10.2. Increased TIT

Another concept is proposed: increasing the TIT, while cooling the bleed air. If the TIT is increased, the turbine requires more cooling. This can be realised by either increasing the amount of bleed air going to the turbine, or by cooling the bleed air once again, using the same principle as described in Subsection 5.10.1. Solely increasing the bleed air going to the HPT will decrease the thermal efficiency. For this reason, the bleed air has to be cooled to increase the thermal efficiency.
This case offers an advantage over the SBC case through two different mechanisms:

- Increasing the TIT (and thus the temperature ratio) increases the specific work output, as there is more energy available to convert into useful work, this can be observed in Equation 3.14 and Figure 3.2. Furthermore, in non-ideal Brayton cycles, increasing the temperature ratio increases the thermal efficiency, as can be observed in Figure 5.11. This is due to the fact that at higher temperatures less irreversibilities are created and consequently, less entropy compared to lower temperatures.

- Increasing the TIT and increasing the amount of bleed flow accordingly, means that the heat capacity increases (although the *specific* heat capacity of the air stays constant). This means that the hydrogen is capable to absorb

a larger amount of heat, before the bleed air reaches its limit of 273 K. This translates to a higher hydrogen temperature and a higher LHV.

The visualisation of this case in Dymola is the same as Figure 5.10.

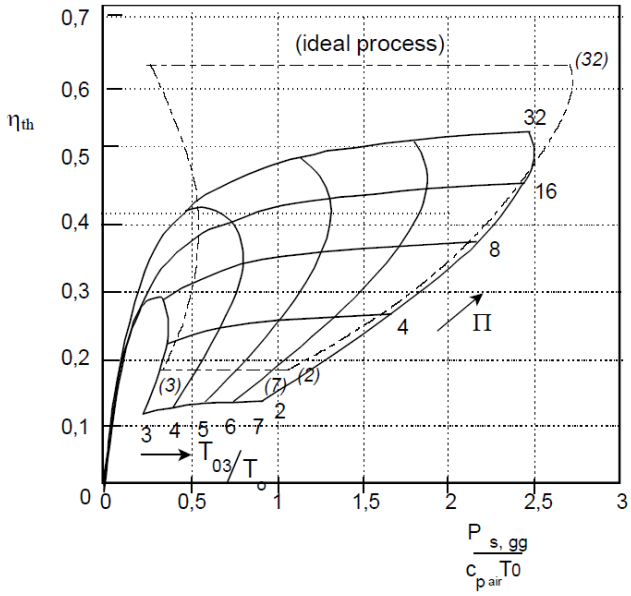

Figure 5.11: Performance graph of a generic non-ideal Brayton cycle

5.10.3. Intercooler

This last concept describes the Intercooling case; in which the cryogenic hydrogen is used to cool the entire core flow between the booster and the HPC.

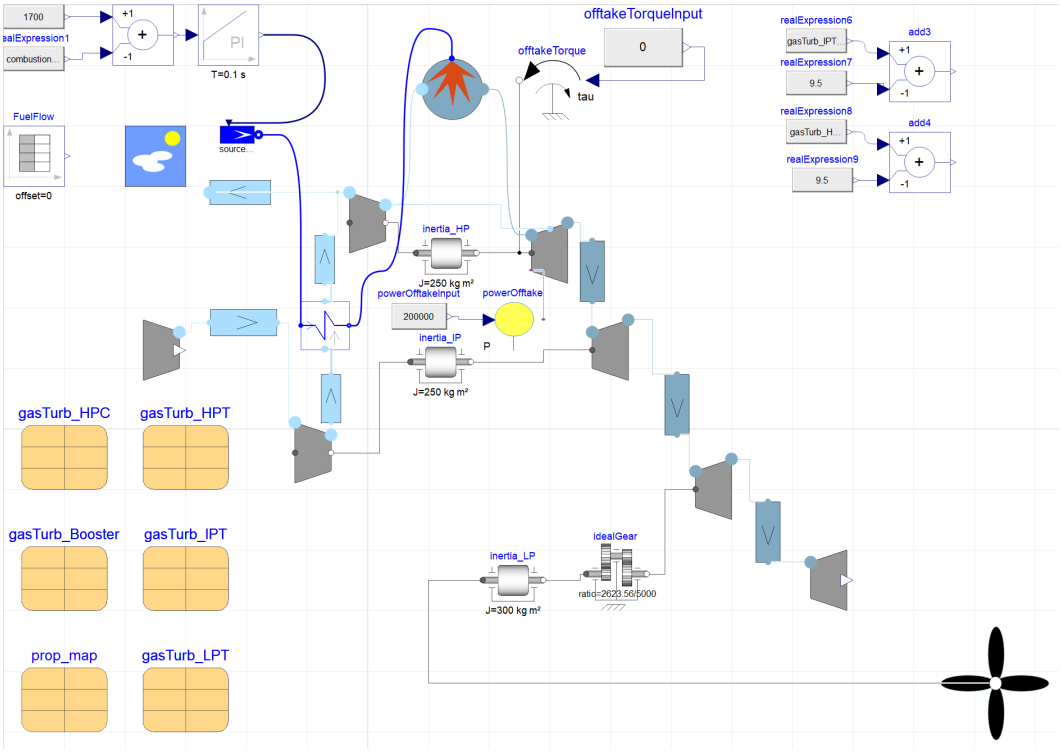

Figure 5.12: Visualisation of the intercooling model in Dymola

As previously mentioned in Section 3.1, intercooling decreases the amount of work that is needed to compress the airflow, however this means that the ΔT in the combustion chamber has to increase, for a fixed TIT, which leads to an increase in PSFC and a decrease in thermal efficiency if no recuperation is used to heat the airflow before entering the combustion chamber. In this case study however, a range of pressure ratios of both the booster and the HPC are

increased by an equal amount. The largest pressure ratio that will be analysed in the pressure ratio that causes the HPC outlet temperature to reach a temperature that is identical to the baseline (which is 736 K). Compared to the Simple Bleed Cooling case, the amount of airflow that flows through the heat exchanger in the Intercooling case is much higher. This means that the hydrogen is capable to attain a much higher value, without risking the airflow to drop below the freezing point of water. Furthermore, because the temperature of the air that is to be cooled is much smaller than the cases described in Subsection 5.10.1 and Subsection 5.10.2, together with an increased mass flow rate, will result into a different and larger heat exchanger design.

5.10.4. Weight verification

To verify heat exchanger weight, the calculated values are compared with data from literature. Most of the heat exchanger weight estimations in aviation, refer back to Kailos' article on Increasing Helicopter Capability from 1967 [16] in which he provides an empirical relation between the specific weight of a heat exchanger in aviation and its effectiveness. Although this source is quite dated, the article of Kailos is still cited in more recent literature, by Ali et al. [58] and Syed[59]. The graph provided in Kailos' paper has been digitised and has been converted into a sixth-order polynomial. This can be observed in Figure 5.13, it should be noted that Kailos assumed the heat exchanger to be made out of Inconel. Furthermore, it should be noted that this relation is only valid for 'fixed surface heat exchangers', such as extended surface heat exchangers as described in Subsection 4.1.3. The provided relation is not valid for rotary type heat exchangers.

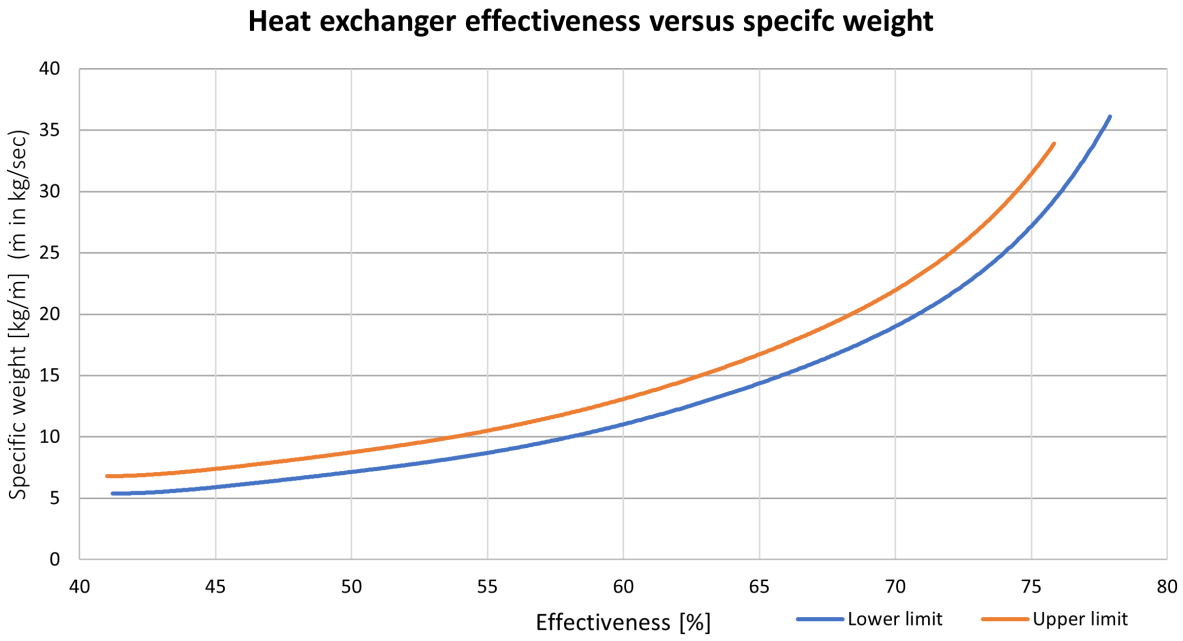

Figure 5.13: Fixed geometry tubular type heat exchanger specific weight versus effectiveness adopted from [16]

Figure 5.13 indicates that the specific weight increases as the heat exchanger effectiveness increases. At 60% effectiveness, the specific weight starts to increase significantly (by a factor of 2 between 60% and 75% effectiveness). This is why most reports (concerning helicopters) that analyse regenerated cycles, limit the heat exchanger effectiveness to 60% [58].
The hydrogen baseline model of the APPU uses a total bleed flow of 0.146 kg/s to cool the HPT at cruise. Making use of Figure 5.13, one can deduce that the weight of a heat exchanger with an effectiveness of 60%, would be between 11 and 13 kg/$\dot{m}$, which, in the case of the APPU, would be between 1.6 and 1.9 kg. In the case a heat exchanger effectiveness of 80%, this would increase to a weight between 6.7 and 7.9 kg. Moreover, the specific weight on the vertical axis in Figure 5.13, is based on an Inconel heat exchanger. It is assumed that this graph translates vertically if another material (such as aluminium) would be used, due to changing density. In reality, if a different material is selected, the conductivity would also change which would lead to a slightly different function. However, as this method is solely used to verify the HEX mass calculation as described in Section 4.4, only translating the graph proportional to the change in density, is deemed sufficient.

6

Top Level Requirements & Dymola Verification

This chapter first discusses the top requirements of the APPU, after which an initial baseline simulation is done in *GasTurb*. Then, a similar simulation will be done in *Dymola*, having converted the baseline model from *GasTurb* to *Dymola*, after which a comparison between the two software will be provided.

The top level requirements are defined defined as [60]:

- Cruise power 2.4 MW
- Max power at take-off at SLS 5 MW
- A 0.5 kg/s of bleed is taken for pneumatic systems
- Auxiliary power of 200 kW is extracted during the entire flight

An early GasTurb-model of the (kerosene) APPU in take-off has been provided by the team working on APPU project, from the Delft University of Technology. This GasTurb-model has been adapted and expanded, namely: the combustion efficiency from 99.95% to 99 %, changing the fuel heating value from 42 MJ/kg to 119.961 MJ/kg (as is appropriate for hydrogen, although this value is a function of the hydrogen temperature) and changing the working fluid in *GasTurb* to hydrogen (meaning that the components are subject to a different flue gas composition, meaning that the specific heat ratio γ changes accordingly). Furthermore, the bleed flow going to the NGV and the rotor blades have been changed in accordance with Equation 5.76. Furthermore, it is assumed that during take-off, an overboard bleed of 0.5 kg/s is needed for pneumatic systems or air conditioning; this overboard bleed is set to 0 kg/s during cruise. During cruise, the aircraft operates at a height of 10058 meters and a Mach of 0.78 and no deviation from the ISA will be assumed. As no initial data is given about the pressure ratios of the booster and the HPC, the assumption is made that both components contribute equally to the pressure increase, as this is thermodynamically most efficient. Initially the overall pressure ratio is given to be 35, which means that both the booster and the HPC will have a pressure ratio of $\sqrt{35} = 5.92$. The other parameters are all kept constant to the provided parameters from the kerosene case, this includes the combustor temperature which is fixed at 1700 K.
Because these parameters are changed from the initial model, the output will change too, most notably the shaft power delivered (PSD) and the mass flow. For this reason, the GasTurb-model has been iterated to achieve a PSD of 2400 kW (5000 kW during take-off), while minimising the core mass flow.
A more detailed overview of the hydrogen baseline parameters from *GasTurb* can be found in Appendix A. As can be seen in Figure A.1, the inlet corrected mass flow isn't the same as value in Table 6.1. This is because *GasTurb* uses mass flow corrected to standard day conditions as input. A full overview of the details can be seen in 6.1.

With the previous specifications, the following results for cruise have been calculated in *GasTurb*.

Table 6.1: Technical specifications initial baseline (hydrogen) cruise

Power	:	2400 kW
Airflow	:	3.662 kg/s
TSFC	:	4.427 g/(kN*s)
PSFC	:	0.05771 kg/(kW*h)
OPR	:	35
Fuelflow	:	0.0385 kg/s
$\eta_{thermal}$	:	0.4898
A_{noz}	:	0.1081 m²
Intake PR		0.98

Efficiencies:		isentropic	polytropic
Booster	:	0.898	0.92
HPC	:	0.899	0.92
Burner	:	0.990	
HPT	:	0.927	0.92
IPT	:	0.915	0.91
LPT	:	0.924	0.90

Table 6.2: Technical specifications initial baseline (kerosene) cruise

Power	:	2400 kW
Airflow	:	3.991 kg/s
TSFC	:	12.96 g/(kN*s)
PSFC	:	0.1686 kg/(kW*h)
OPR	:	35
Fuelflow	:	0.1124 kg/s
$\eta_{thermal}$	:	0.4698
A_{noz}	:	0.1170 m²
Intake PR		0.98

Efficiencies:		isentropic	polytropic
Booster	:	0.898	0.92
HPC	:	0.899	0.92
Burner	:	0.990	
HPT	:	0.927	0.92
IPT	:	0.915	0.91
LPT	:	0.924	0.90

Station	W kg/s	T K	P kPa	WRstd kg/s
amb		222,77	26,202	
1	3,662	249,94	39,174	
1	3,662	249,94	39,174	
2	3,662	249,94	38,390	9,002
24	3,662	433,32	227,270	2,002
25	3,662	433,32	223,861	2,033
3	3,662	736,65	1325,259	0,448
31	3,514	736,65	1325,259	
4	3,552	1700,00	1258,996	0,716
41	3,633	1681,71	1258,996	0,728
42	3,633	1401,64	524,499	
43	3,701	1391,15	524,499	
44	3,701	1391,15	519,254	
45	3,701	1391,15	519,254	1,634
46	3,701	1250,65	313,882	
47	3,701	1250,65	313,882	
48	3,701	1250,65	310,743	2,588
49	3,701	756,96	32,084	
5	3,701	756,96	32,084	19,504
6	3,701	756,96	31,443	19,902
8	3,701	756,96	31,443	19,902
Bleed	0,000	433,32	223,861	

Efficiencies:	isentr	polytr	RNI	P/P
Booster	0,8983	0,9200	0,448	5,920
Compressor	0,8993	0,9200	1,359	5,920
Burner	0,9900			0,950
HP Turbine	0,9271	0,9200	1,590	2,400
IP Turbine	0,9148	0,9100	0,814	1,654
LP Turbine	0,9236	0,9000	0,550	9,685

HP Spool mech Eff	0,9900	Nom Spd	43267 rpm
IP Spool mech Eff	0,9900	Nom Spd	25257 rpm
LP Spool mech Eff	0,9900	Nom Spd	5000 rpm

hum [%]	war0	FHV	Fuel
0,0	0,00000	119,961	Hydrogen

FN	=	8,69 kN
TSFC	=	4,4273 g/(kN*s)
P2/P1	=	0,98000
P25/P24	=	0,98500
P3/P2	=	34,52070
WF	=	0,03847 kg/s
s NOx	=	0,51438
Therm Eff	=	0,48978
WCHN/W25	=	0,02210
WCHR/W25	=	0,01840
P44/P43	=	0,99000
WCIN/W25	=	0,00000
WCIR/W25	=	0,00000
WLcl/W25	=	0,00000
P48/P47	=	0,99000
Incidence	=	0,00 °
P6/P5	=	0,98000
P8/Pamb	=	1,20000
WBld/W2	=	0,00000
A8	=	0,10809 m²
V8	=	287,2 m/s
WBHD/W2	=	0,00000
WBld/W25	=	0,00000
Loading	=	100,00 %
e442 th	=	0,92040
eta t-s	=	0,86763
TRQ	=	100,00 %
PWSD,eq	=	2400,0 kW
SFC,eq	=	0,05771 kg/(kW*h)

Figure 6.1: *GasTurb* results for the engine working on hydrogen at h = 10058 m and M = 0.78 (cruise)

The APPU model from *GasTurb* has been emulated in *Dymola*, using the models described in Chapter 5, using the same input conditions as much as possible. Comparing the outputs of *Dymola* to *GasTurb*, the accuracy of the Dymola-model can be verified. If the outputs of *Dymola* are close to the outputs of *GasTurb*, one can argue that it is likely that the Dymola-model is computing the simulation correctly. Having done a correct verification of *Dymola* to *GasTurb* gives confidence that simulations of new models in *Dymola* are trustworthy.
A visualisation of the setup of the APPU model in *Dymola* can be found in Figure 5.1. The model is simulated using DASSL, and the steady-state results are shown in Table 6.3, Table 6.4 and Table 6.5.

Table 6.3: Baseline (hydrogen) pressure comparison between *GasTurb* and *Dymola* at cruise

Stage	**Gasturb** [bar]	**Dymola** [bar]	**Difference** [%]
P_{amb}	0.26	0.26	0.00
P_1 (booster.P_E)	0.39	0.39	0.00
P_{24} (booster.P_L)	2.27	2.27	0.00
P_3 (HPC.P_L)	13.25	13.28	+0.23
P_4 (HPT.P_E)	12.59	12.61	+0.16
P_{45} (HPT.P_L)	5.245	5.260	+0.29
P_{47} (IPT.P_L)	3.145	3.155	+0.32
P_5 (LPT.P_L)	0.321	0.321	-0.04

Table 6.4: Baseline (hydrogen) temperature comparison between *GasTurb* and *Dymola* at cruise

Stage	**Gasturb** [K]	**Dymola** [K]	**Difference** [%]
T_1 (booster.T_E)	249.9	249.6	-0.12
T_{24} (booster.T_L)	433.3	432.7	-0.14
T_3 (HPC.T_L)	736.7	736.4	-0.03
T_4 (HPT.T_E)	1700	1700	0.00
T_{41} (inside HPT with NGV bleed)	1682		
T_{42} (inside HPT with rotor bleed)	1402		
T_{45} (HPT.T_L)	1391	1389	-0.14
T_{47} (IPT.T_L)	1251	1253	+0.22
T_5 (LPT.T_L)	757	762	+0.65

Table 6.5: Selected parameters baseline comparison

Parameter	**Gasturb**	**Dymola**	**Difference** [%]
PSFC [kg/kWh]	0.0577	0.0574	-0.47
A_{nozzle} [m^2]	0.1408	0.1426	+1.28
m_{fuel} [kg/s]	0.0385	0.0392	+1.85
W_{LPT} [MW]	2.40	2.46	+2.33
$v_{nozzle}[m/s]$	287.2	287.2	0.00
$\eta_{thermal}$ [%]	48.98	50.00	+2.09

As can be seen in Table 6.3 and Table 6.4, the thermodynamic states at each station in *Dymola* closely resembles the results in *GasTurb*, with the largest outlier being the LPT leaving pressure. These very small differences can be explained by the fact that *Dymola* deviates a little bit from the design point, as the beta-values of the component maps change a little bit, due to the model being a dynamic system. The pressures at station '41' and '42' (after the NGV and the first rotor stage, respectively) have not been calculated within *Dymola*, as the Bleed Turbine Model is a lumped-parameter model, meaning that the variables are exclusively calculated at the entering port and the leaving port of the model. Furthermore, a number of selected parameters have been compared with each other in Table 6.5. These discrepancies are also low, the largest being the equivalent shaft power delivered, which is approximately 2% greater in *Dymola*, which corresponds to the increased thermal efficiency.
This can again be ascribed to the changing beta-values, which causes the system to operate a tiny bit off-design. Nevertheless, these differences are very small. This means that it can be concluded that *Dymola* correctly represents *GasTurb* and can be used to expand the model for more sophisticated simulations.

7

Results

The APPU baseline has been constructed in Dymola and verified in Chapter 6. In this chapter the baseline model of both kerosene and hydrogen will be analysed during both take-off and cruise.
Subsequently, in Subsection 7.2.2 the baseline will be extended by adding a heat exchanger between the HPC and HPT that cools down the bleed air and simultaneously heat up the fuel flow, increasing its enthalpy by which the heat of combustion is increased.
Then, using the same principle, Subsection 7.2.3 will show the results of changing the TIT on the engine performance. Subsection 7.2.4 will show the results of using the heat exchanger as an intercooler, after which the calculations on the heat exchanger are shown in Section 4.4.

7.1. Design conditions

The baseline will be created by building on the model provided in Chapter 6. The top level requirements can also be observed in Chapter 6. A few changes have been made:

- The overboard bleed is set to 0 kg/s during cruise, as the overboard bleed is mostly used for pneumatic systems at take-off.
- The power split between the propeller and the nozzle will be close to optimal: maximum specific thrust per cycle.
- The equivalent shaft power delivered during cruise will be decreased to around 2.4 MW, which means that the mass flow entering the system can be decreased, while during take-off the power requirement is considerably higher: around 5 MW [60].

Table 7.1: Operating conditions at the baseline

Operating condition	**Cruise**	**Take-off**	**Cruise**	**Take-off**
Parameter	*Hydrogen*	*Hydrogen*	*Kerosene*	*Kerosene*
Height [m]	10094	0	10094	0
Mach [-]	0.78	0.1	0.78	0.1
TIT [K]	1700	1700	1700	1700
OPR [-]	35	25.6	35	25.6
$\dot{m}_{25}$	3.662	10.020	3.946	10.855
NGV bleed / $\dot{m}_{25}$ [%]	2.18	2.29	2.22	2.35
Rotor bleed / $\dot{m}_{25}$ [%]	1.81	1.91	1.85	1.96
HEX Surface area [m²]	0	0	0	0
Overboard Bleed [kg/s]	0	0.5	0	0.5
Blade angle [°]	56.63	20	56.63	20
Total bleed / $\dot{m}_{25}$[%]	3.99	4.19	4.07	4.31

The reason why the OPR during cruise is higher than during take-off has to do with the fact that T_4/T_2 increases at a higher altitude as the TIT stays fixed, while the ambient temperature decreases at high altitudes. To achieve the most amount of specific work, the ideal pressure ratio most be lower at lower temperature ratios, as can be observed in Figure 3.2. In Table 7.2, the efficiencies of the components can be observed. The isentropic efficiencies are calculated

from the component maps. As it is assumed that the nozzle perfectly expands to the ambient pressure, the nozzle efficiency is 1. The combustion efficiency is assumed to be 0.99 [61] and the mechanical efficiency is assumed to be 0.99 as well. The combustion pressure loss is estimated to be 5%.
The fact that the core flow of the hydrogen system is lower than that of kerosene (while having the same TIT and OPR) is due to the H_2O mass fraction in the flue gas being larger, which leads to an increased specific heat coefficient. Consequently, for a particular temperature, the hydrogen flue gas has more enthalpy than the kerosene flue gas, meaning that the same amount of shaft power can be generated with less mass flow.

Table 7.2: Efficiencies of the components

Efficiencies	Value [-]
Mechanical (HPT, IPT, LPT)	0.99
Booster (isentropic)	0.8983
HPC (isentropic)	0.8993
HPT (isentropic)	0.9268
IPT (isentropic)	0.9147
LPT (isentropic)	0.924
Nozzle	1
Combustor	0.99
Propeller	0.85

Table 7.3: Pressure ratios at the design point

Operating condition	**Cruise**	**Take-off**	**Cruise**	**Take-off**
Pressure ratio	*Hydrogen*	*Hydrogen*	*Kerosene*	*Kerosene*
Booster [-]	5.92	5.3	5.92	5.3
HPC [-]	5.92	4.9	5.92	4.9

Table 7.4: Shaft speeds of the engine

Operating condition	**Cruise**	**Take-off**	**Cruise**	**Take-off**
Shaft speed [RPM]	*Hydrogen*	*Hydrogen*	*Kerosene*	*Kerosene*
PT-shaft	5000	5000	5000	5000
IP-shaft	25257	23735	24331	22836
HP-shaft	43267	12000	41681	37333

7.2. Results

With the top-level requirements and input parameters as defined in Section 7.1, the APPU performance can be calculated. Firstly, the baseline performance is shown, followed by the performance of the APPU engine when the bleed air is cooled together with the specifics of the heat exchanger. Subsequently, the performance of the engine will be shown when adding an intercooler.This section is concluded by comparing the results to the baseline model.

7.2.1. Baseline

The APPU baseline models are initiated by using the input parameters mentioned in Table 7.1 up to Table 7.4 and the component maps mentioned in Appendix B. The shaft speeds mentioned in Table 7.4 are the design shaft speeds, which means that the actual shaft speed will change with time. As the design point of the APPU is at cruise, the calculated nozzle outlet area at cruise will be used at take-off as well. The results at steady-state are mentioned in Table 7.5 and in Table 7.6. Two types of baseline models have been simulated:

- A model in which the LHV of the fuel is calculated with the enthalpy of combustion equation at a reference state of 298 K which only utilises the enthalpy of formation in its calculation. The results of this baseline are shown in Table 7.5 and is labelled as "Baseline with Standard LHV".
- A more realistic model in which the LHV of the fuel is calculated with the enthalpy of combustion equation takes

takes into account the enthalpy of formation *and* the sensible enthalpy (meaning the temperature change of the fuel itself). The results of the baseline are shown in Table 7.6 and is labelled as "Baseline with Variable LHV".

This means that the Baseline with Standard LHV principally injects the hydrogen at 298 K, while the Baseline with Variable LHV principally injects the liquid hydrogen fuel at 20 K. It has been decided that the kerosene injection temperature equals its flash point (which is around 38°C) In reality the hydrogen needs to be vaporised before it is able to combust, these values are calculated for the sake of comparison to other models.

Table 7.5: Output parameters of the baseline at different conditions

Operating condition	**Cruise**	**Take-off**	**Cruise**	**Take-off**
Output parameter	*Hydrogen (LHV includes h_f)*	*Hydrogen (LHV includes h_f*	*Kerosene (LHV includes h_f)*	*Kerosene (LHV includes h_f)*
PSFC [kg/kWh]	0.05778	0.06995	0.1667	0.2032
PSD, eq [MW]	2.41	5.02	2.41	5.02
F_{total} [kN]	8.8	46.0	8.9	46.1
F_{sp} (kN/kg/s)	2.41	4.59	2.25	4.25
m_{fuel} [kg/s]	0.03919	0.09828	0.1132	0.2861
V_{nozzle} [m/s]	170	134	167	133
$V_{nozzle,opt}$ [m/s]	170	23	167	28
A_{nozzle} [m²]	0.1843	0.1843	0.195	0.195
$\eta_{thermal}$ [-]	0.5194	0.4291	0.5058	0.4148
$\dot{m}_{25}$ [kg/s]	3.662	10.02	3.946	10.855
$\dot{m}_{45}$ [kg/s]	3.701	9.220	4.059	10.642

Table 7.6: Output parameters of the baseline in which LHV includes the formation enthalpy h_f of the fuel and the sensible enthalpy & h_s

Operating condition	**Cruise**	**Take-off**	**Cruise**	**Take-off**
Output parameter	*Hydrogen (LHV includes h_f & h_s, T_{fuel} = 20 K)*	*Hydrogen (LHV includes h_f & h_s, T_{fuel} = 20 K)*	*Kerosene (LHV includes h_f & h_s, T_{fuel} = 311 K)*	*Kerosene (LHV includes h_f & h_s, T_{fuel} = 311 K)*
PSFC [kg/kWh]	0.05970	0.07381	0.1666	0.2031
PSD, eq [MW]	2.43	4.94	2.41	5.02
F_{total} [kN]	8.9	46	8.9	46.1
F_{sp} (kN/kg/s)	2.43	4.54	2.25	4.25
$\dot{m}_{fuel}$ [kg/s]	0.04078	0.1020	0.1131	0.2858
V_{nozzle} [m/s]	170.8	136	167	133
$V_{nozzle,opt}$ [m/s]	170.8	23	167	28
A_{nozzle} [m²]	0.1847	0.1847	0.196	0.196
$\eta_{thermal}$ [-]	0.5026	0.4066	0.5061	0.4151
LHV [MJ/kg]	116.032	116.045	42.73	42.73
$\dot{m}_{bleed,total}$ [kg/s]	0.1461	0.3991	0.1606	0.4209
$\dot{m}_{45}$ [kg/s]	3.703	9.623	4.058	10.641

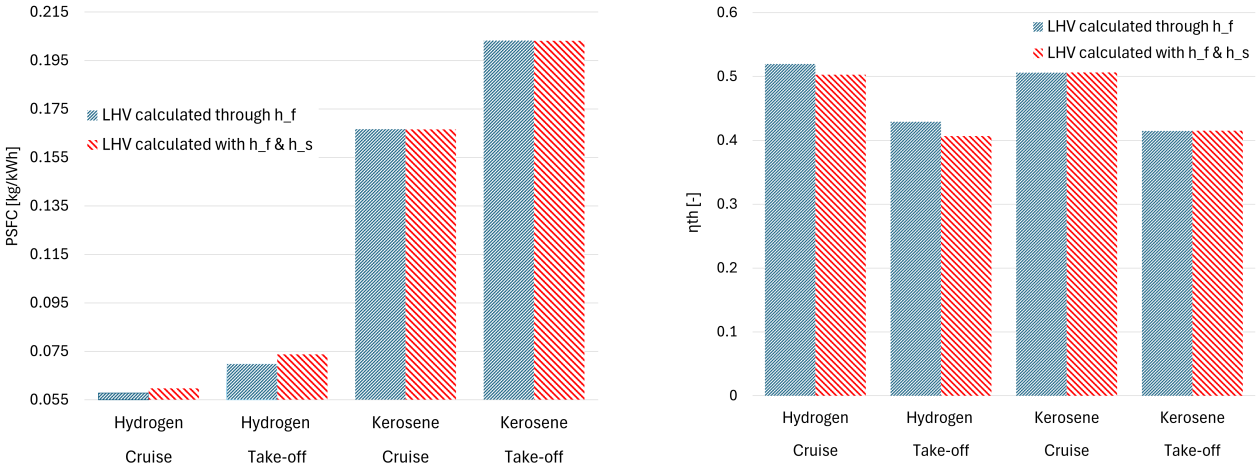

(a) PSFC of baseline

(b) η_{th} of baseline

Figure 7.1: Comparison of PSFC and thermal efficiency for baseline configuration

As can be observed, the baseline with standard LHV for hydrogen has a better performance than baseline with variable LHV. For the hydrogen baseline with variable LHV at cruise operation, the thermal efficiency decreases with approximately 3.2% and the PSFC increases with approximately 3.3 % compared to the baseline with standard LHV. This is to be expected, as a larger amount of enthalpy is injected into the system (298 K compared to 20 K). The difference between the baseline with standard LHV and the baseline with variable LHV of the kerosene case is much smaller, as the difference of the fuel temperature is much smaller compared to hydrogen.
This means that the LHV of the hydrogen case *cannot* be assumed to be constant, as the fuel temperature has a huge effect on the system performance. This is in stark contrast to kerosene, as the cycle performance due to change in fuel temperature is negligible. The baseline with variable LHV will be used to compare any further models, as its inclusion of the fuel temperature on the LHV is physically more accurate.

The T-s plot of the hydrogen baseline with variable LHV can be observed in Figure 7.2. The very steep, almost vertical line between point 4 and 43 may seem to indicate that the expansion is isentropic, however this decrease in specific entropy is due to the addition of the bleed air, which has a temperature of 736 K. In reality the specific entropy between point 4 and 43 should increase a little bit due to the entropy of mixing, which happens if two streams of fluid with different composition (and temperature) mix with each other. This is not taken into account.

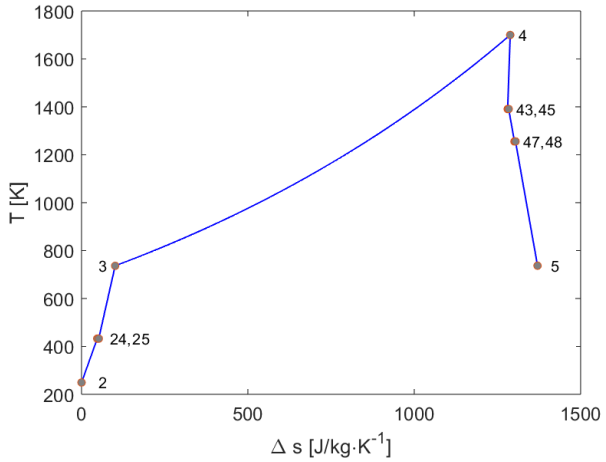

Figure 7.2: T-s plot of the hydrogen baseline case at cruise

7.2.2. Simple Bleed cooling

This subsection will focus on the APPU system in which the liquid hydrogen is used to cool down the bleed air. This case is labelled as 'Simple Bleed Cooling'. The heat exchanger will be sized such that the bleed air will attain a temperature of approximately 273.5 K, which is just above the freezing point of water, as previously mentioned in Subsection 4.3.1. This results into a lesser required bleed flow to keep the turbine blades at a temperature of 1456 K, which

consequently results into a higher core flow and an increased fuel temperature, which both contribute to a better system performance. All the other input parameters, such as TIT, OPR and $\dot{m}_2$ are kept constant to the baseline.
The introduction of a heat exchanger and a diffuser also comes at the expense of total pressure losses. These pressure losses have been calculated using the methods described in Subsection 4.3.4. The total pressure loss encountered is approximately 2.1% of the HPC leaving pressure. This pressure loss has not been included in the system performance calculations, as the HPT model hasn't been developed to include pressure losses in the bleed flow.

Table 7.7: Results of the Simple Bleed Cooling case at cruise and take-off

Operating condition	**Cruise**		**Take-off**	
Output parameter		*Difference w.r.t. baseline [%]*		*Difference w.r.t. baseline [%]*
Stator bleed [%]	1.38	-37	1.39	-39
Rotor bleed [%]	1.15	-37	1.16	-39
PSFC [kg/kWh]	0.05958	-0.20	0.07360	-0.29
PSD, eq [MW]	2.44	0.44	5	1.32
F_{total} [kN]	8.93	0.41	45.9	0.88
F_{sp} [kN/kg/s]	2.44	0.39	4.58	0.86
$\dot{m}_{fuel}$ [kg/s]	0.04089	0.26	0.1031	1.05
V_{nozzle} [m/s]	172	0.70	137	0.74
$V_{nozzle,opt}$ [m/s]	172	0.70	24	4.35
A_{nozzle} [m²]	0.1837	-0.54	0.184	-0.36
$\eta_{thermal}$ [-]	0.4994	0.219	0.4073	0.29
T_{fuel} [K]	84.3	322	95.6	378
LHV [MJ/kg]	117.13	0.95	117.24	1.0
$\dot{m}_{bleed,total}$ [kg/s]	0.0926	-36.6	0.243	-39
$\dot{m}_{45}$ [kg/s]	3.703	0.001	9.385	-2.5
$\dot{m}_{HEX}$ [kg]	2.211	/	2.211	/

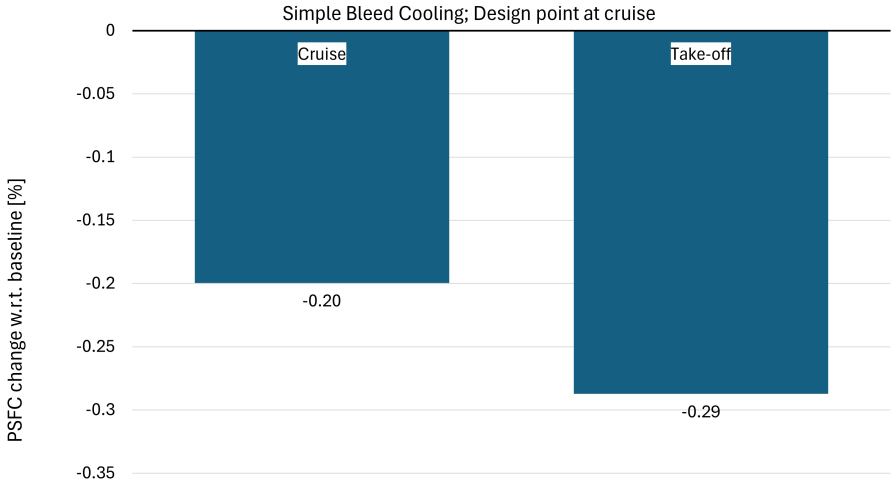

Figure 7.3: Power Specific Fuel Consumption change of Simple Bleed Cooling w.r.t. the baseline (decreased bleed flow, i.e. higher core flow)

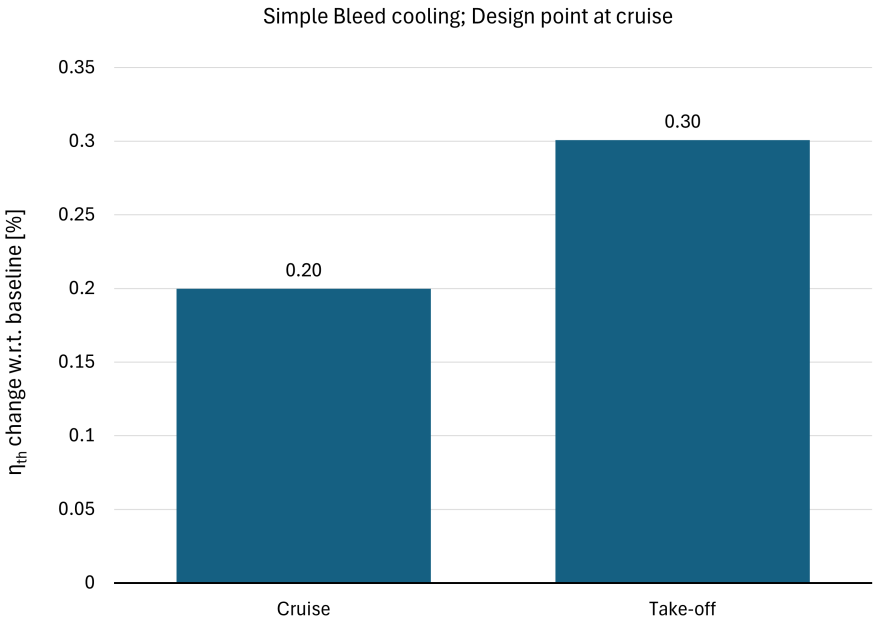

Figure 7.4: Thermal efficiency change of Simple Bleed Cooling w.r.t. the baseline (decreased bleed flow, i.e. higher core flow))

As can be observed from Figure 7.3 and Figure 7.4, the engine's performance is increased by Simple Bleed cooling; during cruise, the PFSC decreases with approximately 0.2 % while the thermal increases by approximately the same amount with respect to the baseline. The performance increase during take-off is even higher. This is because the amount of bleed air during take-off is higher, which allows the hydrogen to extract more enthalpy from the bleed air, resulting into a further reduction in the required mass flow. Furthermore, using the methodology as described in Section 4.4, the total added mass of adding the heat exchanger plus its system integration is estimated to be 2.2 kg, while the effectiveness of the heat exchanger has been calculated to be around 70%, using the calculation method described in Subsection 4.3.3. The verification method as described in Subsection 5.10.4, indicates that the heat exchanger mass should lie in the range of 1.78 kg and 2.12 kg, which is not too far off.

The T-s plot of SBC is shown in Figure 7.5. Not a large difference can be observed. A close-up of the T-s plot can be observed in Figure 7.6, and it can be observed that the specific entropy actually decreases a little bit. This can be explained by the fact that the small amount of bleed air that enters the HPT is cooler compared to the baseline.

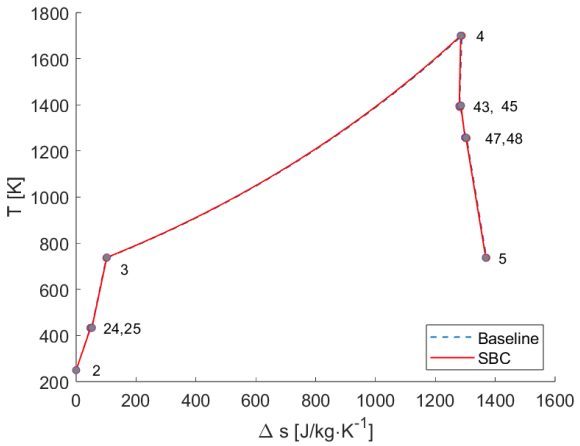

Figure 7.5: T-s plot of the hydrogen Standard Bleed Cooling case at cruise

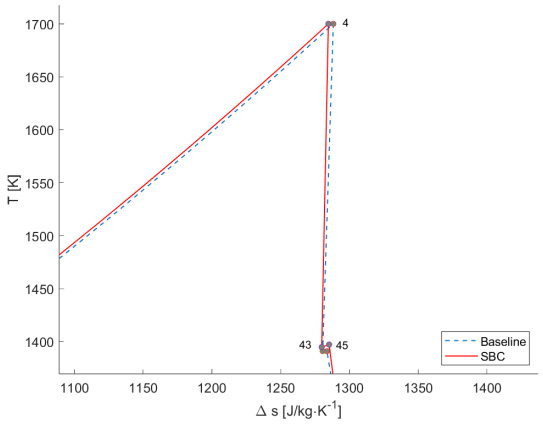

Figure 7.6: Zoomed-in view of the T-s plot

7.2.3. Changing TIT

Another case that can be studied, is the effect of increasing the TIT. If the TIT is increased, then the amount of bleed air should be increased as well, to keep the turbine blade temperature constant (at 1456 K). The bleed air is again cooled down to around 273 K, such that a lesser amount of bleed air is needed. The change in PSFC and thermal efficiency with respect to the baseline can be observed in Figure 7.7. As expected, the engine performance increases if the TIT

is increased. The graph starts at a TIT of 1700 K, which is identical to the SBC-case. The TIT then increases, as well as the required bleed air, which causes the thermal efficiency to increase as well.
At a TIT of approximately 1840 K, the amount of (cooled) bleed air required equals the amount of required bleed air in the baseline. This means that at a TIT of 1840 K, all the other input parameters, such as OPR, m_2 and the bleed air to the HPT are kept constant to the baseline. As can be observed from the graph, the thermal efficiency increment is much larger than the increment that could be achieved at the SBC-case.

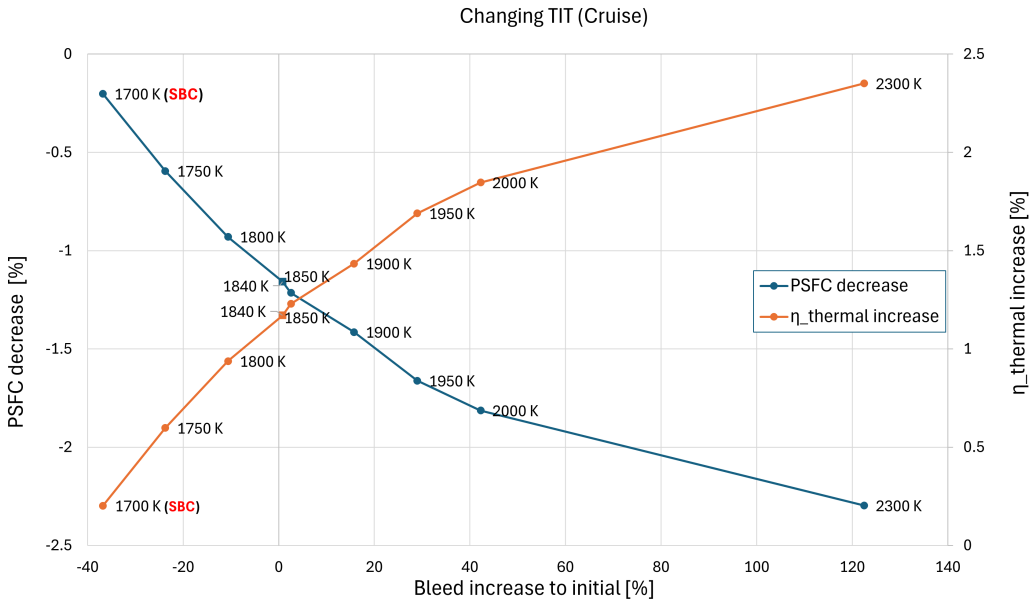

Figure 7.7: Percentual changes of PSFC and thermal efficiency for changing TIT at cruise; T_{bleed} = 273.5 K

The absolute values of the PSFC and the thermal efficiency are shown in Figure 7.8. This graph shows the absolute values of PSFC and thermal efficiency compared to the hydrogen baseline. The values of the *kerosene* baseline lie outside of the picture, as the thermal efficiency of the *kerosene* baseline is approximately 50.6%, while the PFSC is approximately 0.167 kg/kWh.

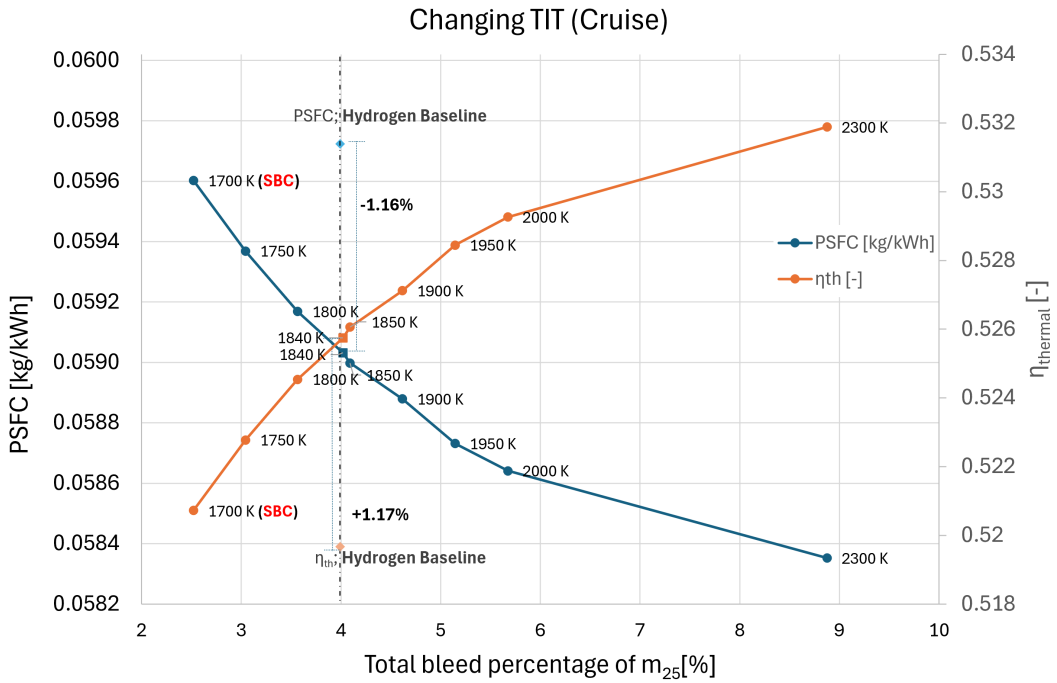

Figure 7.8: Percentual decrease of PSFC and increase of thermal efficiency for different TIT at cruise conditions

Figure 7.9 shows that the temperature of the fuel increases in a non-linear fashion for increasing TIT.

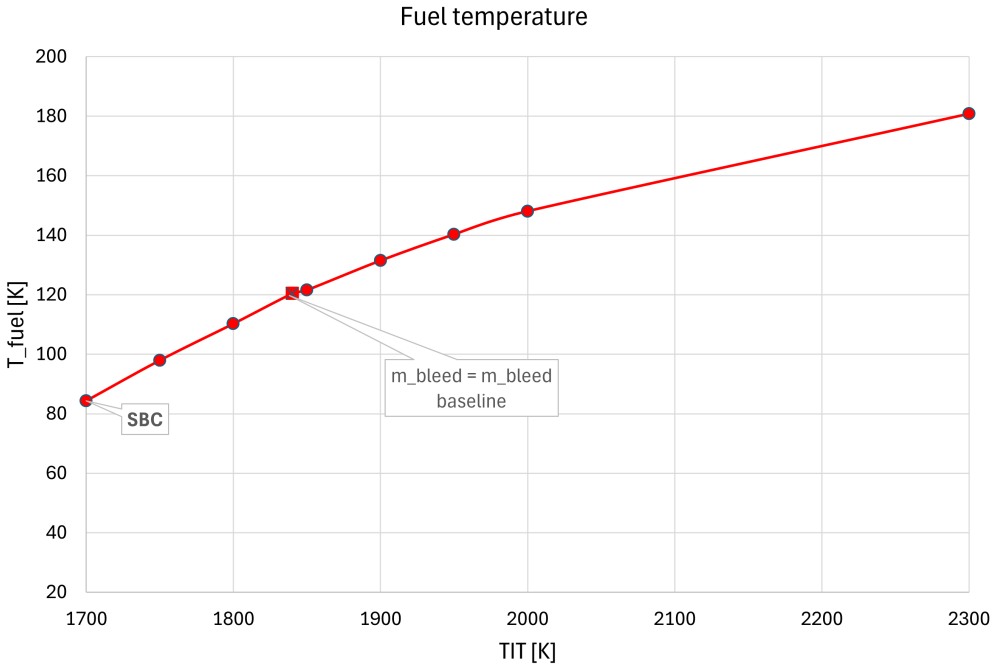

Figure 7.9: Hydrogen temperature when changing the TIT at cruise conditions

The increase in required bleed flow due to the increasing TIT, means that the heat capacity rate of the air also increases. This means that the heat transfer area of the heat exchanger must be increased as well, to keep the bleed air temperature at approximately 273.5 K. Increasing the heat transfer area of the heat exchanger with a fixed internal geometry, means that the external geometry has to be increased, which leads to a higher heat exchanger volume and thus a higher mass. The change in heat exchanger mass can be observed in Figure 7.10. Figure 7.11 shows the T-s plot

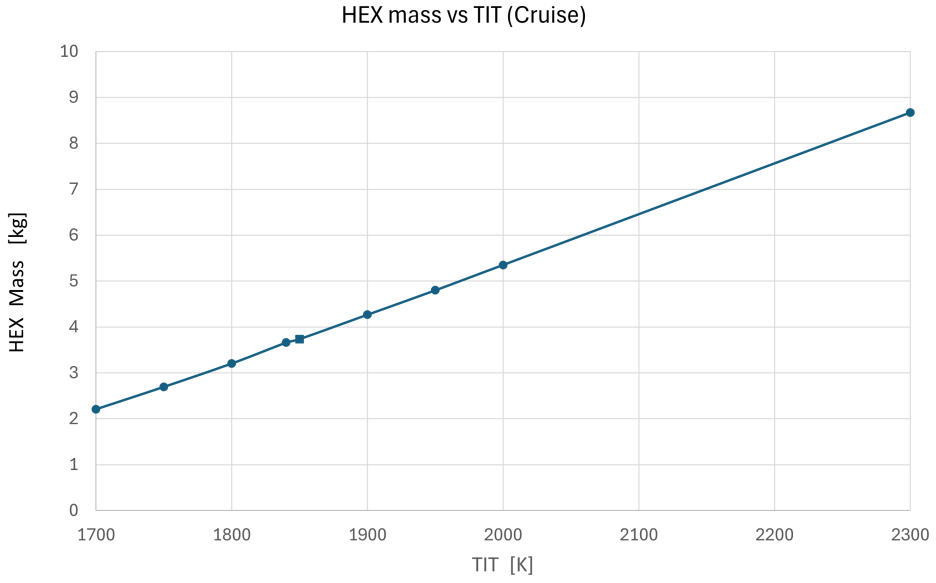

Figure 7.10: Heat exchanger mass as a function of TIT

of the APPU engine cycle in which the TIT has been increased to a temperature of 1840 K. It can be observed that the amount of net work increases.
The specific heat capacity at each station changes and is calculated by averaging the specific heat capacity at the inlet and outlet of each component (in reality the specific heat capacity changes continuously), with the exception of the combustor. In the combustor, the specific heat capacity at the combustor outlet is used to calculate the specific entropy. For this reason, a small discrepancy can be observed in the heat addition lines between point 3 and 4.

Moreover, the expansion line between 4 and 43 of the new engine cycle *decreases* the specific entropy, much more than the baseline. This is ascribed due to the fact that a larger amount of cooled bleed air enters the HPT.

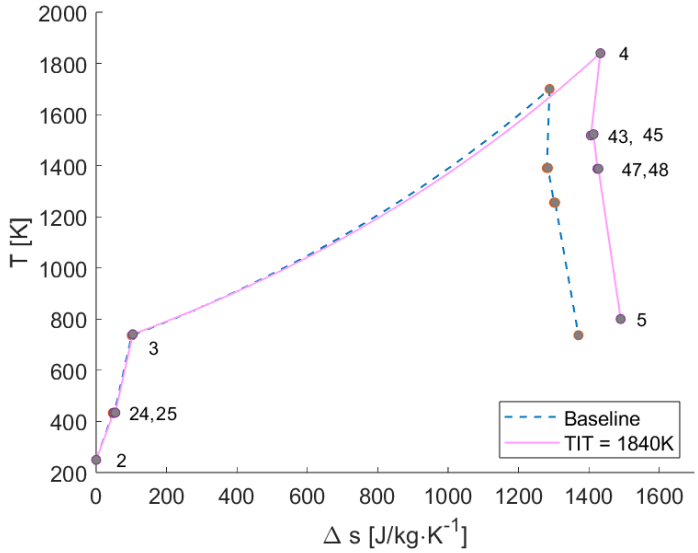

Figure 7.11: T-s plot of the APPU hydrogen, at cruise, TIT=1840

7.2.4. Intercooler

This last variation of the APPU engine includes the Intercooling-case, in which the cryogenic hydrogen cools the entire core flow between the booster and the HPC. This case is simulated to an extend in which the hydrogen attains a temperature which is very close to the temperature of the entering airflow. The hydrogen temperature is therefore able to be heated up to 472 K, while the airflow is cooled down from 473 K to approximately 408 K. Subsequently, the pressure ratio of the booster and the HPC are both increased equally from 5.92 to 8, which results to a HPC outlet temperature of 736 K (as was the case in the baseline). This means that except the compression ratios, the rest of the input parameters, such as TIT, bleed flow going to the HPT and m_2 stay constant to the baseline. The increase in pressure ratio affects the polytropic- and consequently the isentropic efficiency negatively, as described in Subsection 3.1.2, so an assumption should be made in what terms this affects the values of the system performance.

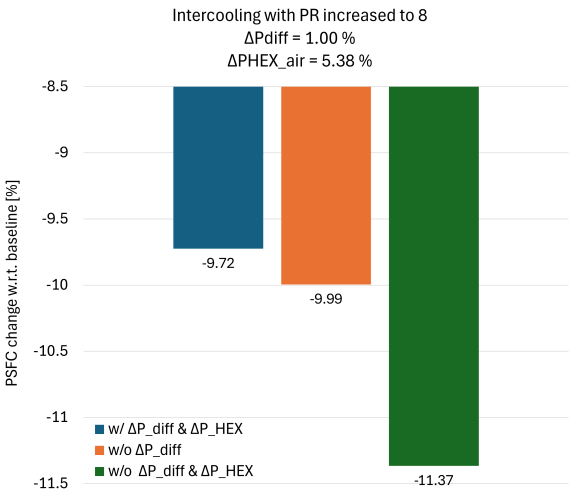

Figure 7.12: Power Specific Fuel Consumption change with respect to the baseline for an intercooler with increased pressure ratio

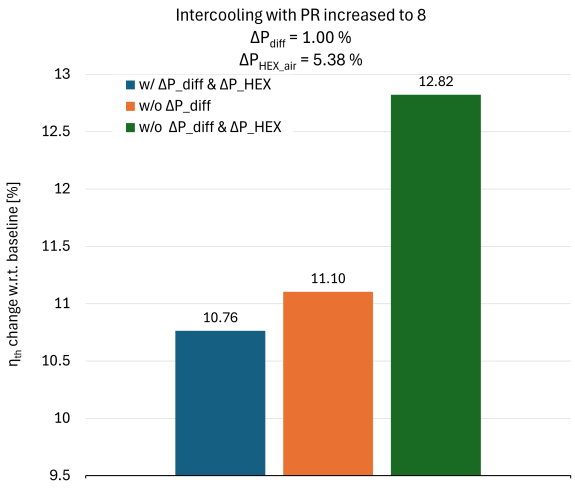

Figure 7.13: Thermal efficiency change with respect to the baseline for an intercooler with increased pressure ratio

The total pressure losses due to the diffuser and the heat exchanger have been calculated to 1.0 % and 5.4%, respectively and have been included included in this simulation. As can be observed in Figure 7.12 and Figure 7.13, the performance of the engine system can be increased by a huge amount. Furthermore, the effect of the pressure losses on the performance are not to be neglected. The reduction in PSFC compared to the baseline without taking into

account any pressure losses is approximately 11.4 %, while the introduction of both HEX and diffuser pressure losses reduce this to only 9.7 %. This means that the pressure losses in this specific case contribute for a *relative percentage* decrease of 15 % in system performance.
Furthermore, because the amount of airflow that passes through this heat exchanger is much higher than the Simple Bleed Cooling case, the size and mass of the heat exchanger will be higher as well. Again using the methodology described in Section 4.4, the heat exchanger mass has been calculated to be 22.0 kg. Furthermore, the heat exchanger effectiveness has been calculated to be 84.5 %. This value is subsequently verified, using the correlation described in Subsection 5.10.4 indicates that the HEX mass should lie between 19.9 kg and 22.4 kg.
Figure 7.14 shows the percentual difference of the thermal efficiency and the PSFC with respect to the baseline. Figure 7.15 shows the increase of the fuel temperature with respect to OPR. Contrary to the Increasing-TIT case, in which the fuel temperature increased non-linearly, increasing the OPR increases the temperature linearly.

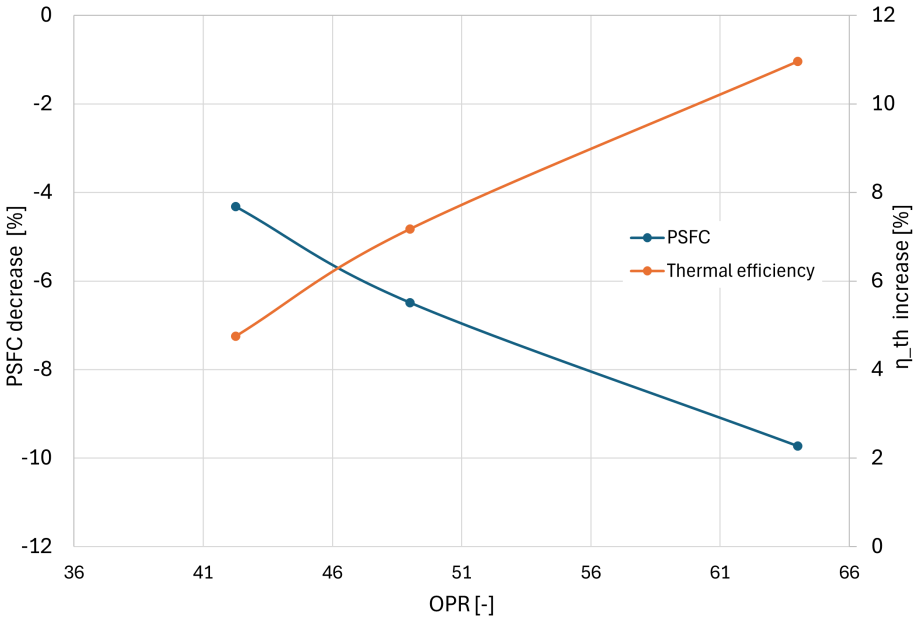

Figure 7.14: Percentual changes of PSFC and thermal efficiency for changing OPR at cruise

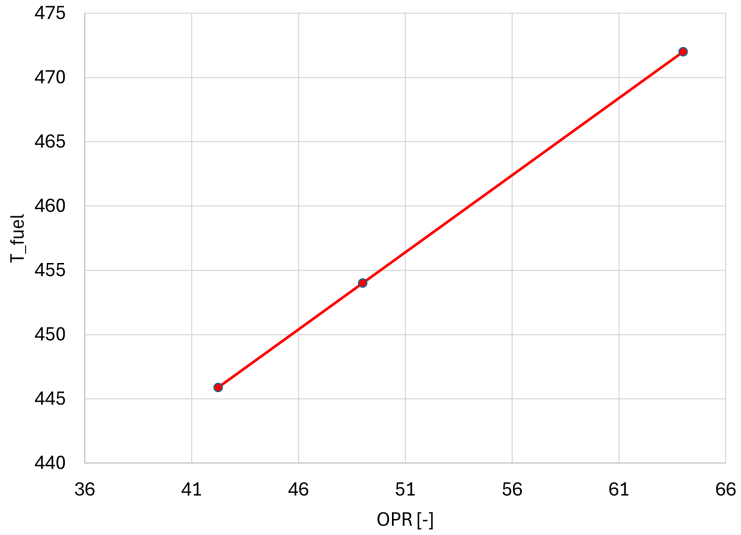

Figure 7.15: Fuel temperature as a function of OPR at cruise

Figure 7.16 shows that increasing the OPR generates less entropy. The line of the heat addition (3-4) becomes steeper when the pressure ratio is increased. This is explained by the fact that increasing the pressure ratio also increases the HPC outlet temperature, which increases the specific heat capacity in the combsutor.

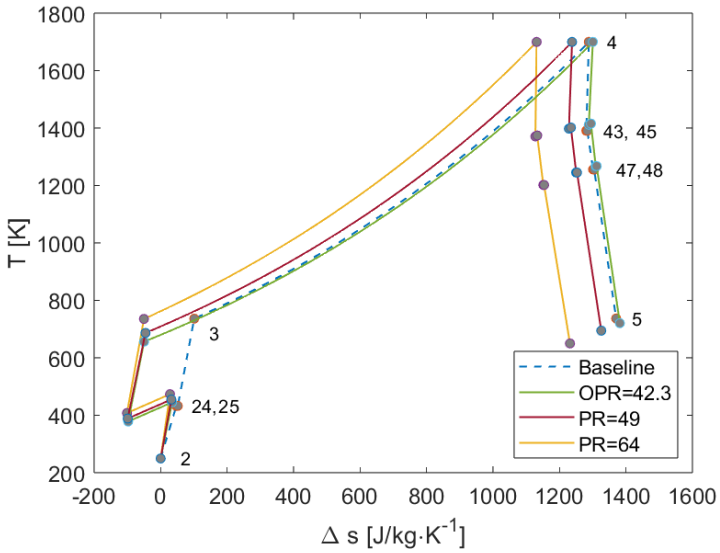

Figure 7.16: T-s plot of the APPU (hydrogen, at cruise), different PR

7.3. Sensitivity analyses

The introduction of cooling the bleed air and subsequently decreasing it, as well as the introduction of an intercooler increase the performance of the engine cycle. However, multiple aspects contribute to this performance increase: the increase in LHV due to the fuel heating up and increase in core flow. To analyse the effect of each contribution, multiple simulations have been conducted that isolate the effects of each aspect.

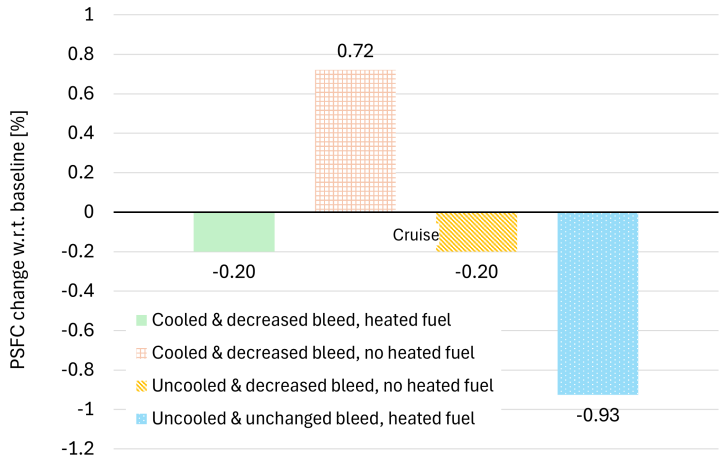

Figure 7.17: Contributions of bleed and fuel temperature on the PSFC

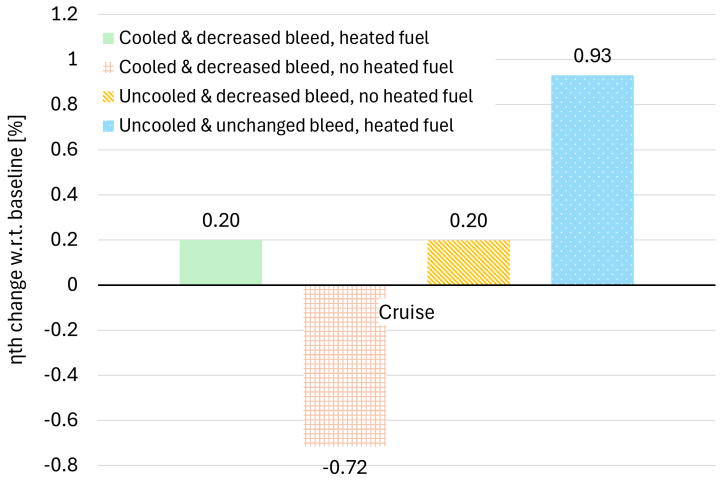

Figure 7.18: Contributions of bleed and fuel temperature on the thermal efficiency

At the cruise condition, four different simulations have been conducted:

- A case in which the bleed flow is cooled down to 273 K, in which the total amount of bleed flow has been decreased with 37 % and in which the fuel temperature has been increased through the heat exchanger accordingly (from 20 K to 84.3 K). The data of this case can be observed in Table 7.7, Figure 7.3 and Figure 7.4. This case is indicated by the green block diagram in Figure 7.17 and Figure 7.18.
- A case in which the fuel temperature is *not* heated, but rather stays at 20 K. The bleed flow is again cooled down to 273 K, and the bleed is decreased with 39 %, similar to the previous case. This case is indicated by the red block diagram in Figure 7.17 and Figure 7.18.
- A case in which the neither the fuel temperature is increase, nor the bleed flow is cooled down. The only changed variable is the the amount of bleed, which is decreased by 37 %. This case is indicated by the yellow block diagram in Figure 7.17 and Figure 7.18.
- A case in which the bleed is not cooled down, nor decreased. The only changed variable is the fuel temperature, which is raised to 84.3 K. This case is indicated by the blue block diagram in Figure 7.17 and Figure 7.18.

It can be observed that the largest contribution to the system performance is the heating of the fuel, which decreases the PSFC with approximately 0.9 % compared to the baseline. Only decreasing the bleed flow contributes to a much smaller decrement in PSFC, namely 0.2 %. If the bleed flow were to be cooled down, and subsequently its mass flow decreased *without* heating up the fuel would actually contribute in a *worse* system performance. This is because a cold air flow is injected into the HPT, which considerably decreases its specific enthalpy. In the case of heating the fuel flow, the amount of enthalpy that is taken away from the HPT is reinjected into the combustion chamber, evening out the losses. For this reason, the green bar and the yellow bar are almost identical: the amount of enthalpy in the system stays constant.
Furthermore, a similar analysis has been conducted to the Intercooler case. The analysis has been conducted for the Intercooler case that includes both the diffuser *and* heat exchanger pressure losses. As can be observed in Figure 7.19 and Figure 7.20, the largest contributor to the system performance increase, is the increase in fuel temperature, although the increase in pressure ratio also yields a large contribution.

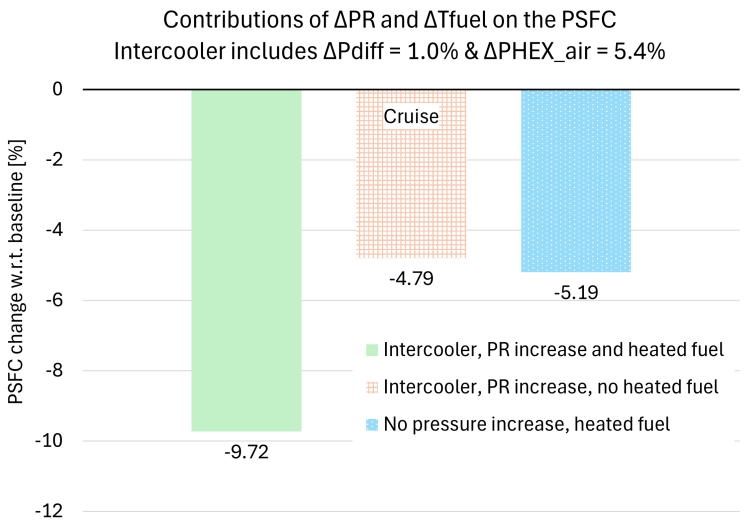

Figure 7.19: Contributions of increasing the overall pressure ratio to 64, and raising the fuel temperature to 472 K on the PSFC

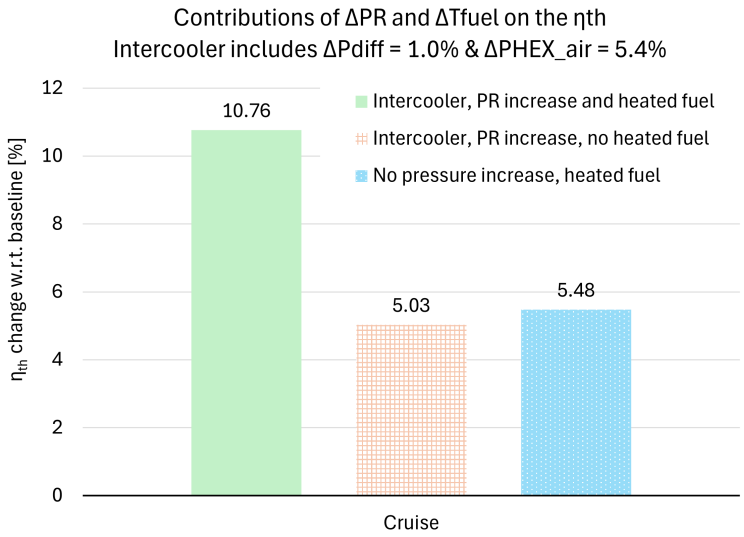

Figure 7.20: Contributions of increasing the overall pressure ratio to 64, and raising the fuel temperature to 472 K on the thermal efficiency

7.4. Impact on aircraft fuel

As mentioned in Section 5.9, additional mass due to the inclusion of a heat exchanger increases the portion of the fuel flow to the main engines. However, if this deterioration if offset by the performance increase of the altered engine cycle, the net fuel flow of the main engine will be smaller.
As these values are calculated assuming that the increase in main engine thrust is linearly proportional to the increase in MTOM, the effect of the BLI is not taken into account in the calculation of the TSFC, and only the cruise conditions have been analysed, the following results are a fairly rough estimate.

Table 7.8: Effects of different engine cycles on the aircraft-level performance

Output parameter	**SBC**	**TIT = 1840**	**Intercooling OPR = 64**
m_{HEX} [kg]	2.21	3.66	22.0
Δ % TSFC w.r.t. baseline [%]	-0.15	-0.99	-9.12
$\Phi_{APPU,new}$ [-]	0.1683	0.1697	0.1849
$\Delta\%\Phi_{APPU}$ [%]	0.15	0.99	10.04
Δ Φ [-]	0.0003	0.0017	0.0169
$m_{fuel,new}$ [kg]	12457	12439	12249
$\Delta\%m_{fuel}$ [%]	-0.03	-0.17	-1.69

As can be observed from Table 7.8, on aircraft-level, the increasing TIT-case does much better than than the SBC-case, as the thermal efficiency of the former is much higher than the latter, while the difference in additional mass is relatively small. The largest increase is again observed from the Intercooling-case, which increases the APPU thrust fraction by 1.69% and decreases the amount kerosene by the same amount.

Assuming that the price of kerosene per kg is €0.65 per kilogram as of December 2024 [62], and assuming that the Airbus A321neo APPU will be making an average of two flights per day, the amount of money that can be saved, has been calculated. Furthermore, assuming that kerosene can be represented as $C_{12}H_{26}$, the amount of CO_2 that will be saved during a flight can be calculated, as can be observed in Table 7.9.

Table 7.9: Effects of different engine cycles on fuel savings

Output parameter	**SBC**	**TIT = 1840**	**Intercooling OPR = 64**
Kerosene saved per flight [kg]	3.2	20.8	210
€ saved per flight	2.1	13.5	136.6
€ saved per year	1 500	9 881	99 779
CO_2 saved per flight [kg]	9.8	65	651
CO_2 saved per year [t]	7.1	47	476

8

Discussion

This study aimed to develop a dynamic model that is able to utilise the heat sink of the hydrogen to increase the aircraft performance. A number of simulations have been conducted and a multitude of results have been obtained. The results of Chapter 7 need to be critically analysed, whether these results comply with established literature. Moreover, any unexpected behaviour, inaccuracies and assumptions have to be analysed to find its implications on the results.

8.1. Key Findings and Optimal Case

In Section 7.2 the three different cases have been simulated:

- Cooling and decreasing the bleed flow while the TIT and OPR stay constant to the baseline.
- Raising the TIT to 1840 K such that the cooled bleed air stays constant to the baseline as well as the OPR.
- Intercooling the core flow while simultaneously increasing the overall pressure ratio to 64, while the TIT, HPC outlet temperature and bleed flow stay constant to the baseline.

The results show that the Intercooling-case causes the largest increase in thermal efficiency and largest decrease in PSFC, followed by increasing the TIT-case, and lastly the Simple Bleed Cooling-case.
The results shows that in each case, the largest contributor to the system performance is the fuel temperature which increases the amount of enthalpy in the system. This contribution weighs relatively more than reducing the bleed flow or increasing the pressure ratio. This means that if a proper way can be found to increase the fuel temperature even further, without necessarily changing the engine design, the engine system can perform even better.
As illustrated in Figure 7.19 and Figure 7.19, the percentual decrease in PSFC observed for the case where both fuel preheating (PSFC -5.19%) and pressure ratio enhancement (PSFC -4.79%) are applied closely approximates the summation of the individual contributions from each modification (PSFC -9.68%), with a minor discrepancy of 0.04%, which is ascribed to the bilinear interpolation procedure while scaling the maps. A similar behaviour can be observed for the SBC-case. This means that the OPR and the fuel temperature are uncoupled from each other, as well as the core flow and the fuel temperature, as long as the component maps are able to find a solution that converges. This means that if the fuel temperature were to be increased, without taking the core flow or the OPR into consideration, the engine performance would increase in a very predictable fashion.

This raises the question whether using a combination of the Intercooling-case and the SBC-/Increasing TIT-case would increase the system performance even further, and how much, and would a combination of these cases be uncoupled with each other with respect to the system performance?

8.2. Combining the Intercooling-case with the SBC-/Increasing TIT-case

Increasing the pressure ratio together with intercooling would decrease the amount of entropy generated in the system. Less bleed flow, as the results show also increase the cycle efficiency and the PSFC. If these two principles were to be combined the system performance would definitely increase, mainly due to the increase in fuel temperature. In the case of such a combination, a decision should be made whether to cool the bleed air first, or to cool the booster outlet first. The SBC-case increases the fuel temperature to 84 K, while the Intercooling-case (with a OPR of 64) increases the fuel temperature to 472 K, in which the former is limited by the freezing point of water in the bleed air and the latter is limited by the booster outlet temperature. In the Increasing TIT-case however, if the TIT were to be increased to a temperature that exceeds practical limits, such as 2300 K, the fuel temperature increases to approximately 180 K. This means that the maximum achievable hydrogen temperature is dictated by the booster outlet temperature, when combining these cases. The first flow to undergo cooling experiences a larger temperature gradient due to the

initially greater thermal differential, whereas the second flow encounters a reduced temperature gradient as a result of the diminished thermal contrast. This means that the flow that the last flow to be cooled will need a larger heat exchanger, increasing the additional mass. However, if the air flow between the booster and the HPC were to cooled to its limit first, the hydrogen fuel becomes 472 K, which means that the lower limit of the bleed air increases (from 273 K to 472K), consequently increasing the required bleed flow as mentioned in Equation 5.76, which results into a lower engine performance.
Therefore, if the proposed concepts were to be used in combination with each other, the bleed air should be cooled before the core flow between the booster and HPC. This consideration is valid only under the assumption that the APU operates independently, without integration into the primary propulsion system. On the aircraft-level, however, this means that the intercooler mass increases, due to which the APPU thrust fraction would be decreased which needs to be compensated for by the main engine. This means that intercooling and required bleed flow reduction are coupled with each other, and further calculations should be done whether the reduced performance due to the heat exchanger mass increase of such a combined case outweighs the benefit of decreasing the bleed flow.

8.3. Effects on the bleed flow

Increasing the OPR results into an increased bleed air pressure. This means that the specific heat capacity of the bleed air increases, as c_p increases with pressure. Therefore, the bleed air would be able to transfer more heat to the hydrogen before the bleed air reaches its lower temperature limit, which means that the heat exchanger can be more compact. Moreover, an increased specific heat capacity of the bleed air means that less bleed air is needed, according to Equation 5.76. In reality however, the effect of the pressure on the specific heat capacity is minimal. If the OPR is increased from 35 to 64, the specific heat capacity only increases with 0.2%, which decreases the required mass flow by a similar percentage. Considering the SBC-case, in which decreasing the bleed flow with 37% resulted in a PSFC decrease of 0.2%, decreasing the bleed flow with 37.2% would virtually make no difference.

8.4. Implications of η_{is} on η_{th}

The baseline engine has been modelled with an OPR of 35, this is on the high side, especially for an auxiliary power unit, which tend to have a lower pressure ratio than the main engine. Increasing the pressure ratio of both the booster and the HPT to 8, leads to an OPR of 64. This might not be viable with current technology, and might have some serious repercussions on the isentropic efficiency the compressor operates at. Nevertheless, the behaviour of such a high pressure engine can be analysed, albeit very crudely, to get a better understanding for similar cases.
As mentioned in Equation 3.20, the isentropic efficiency of a compressor decreases with an increasing pressure ratio. Moreover, although the polytropic efficiency is mainly dictated by the stage and blade geometry, as well as the flow behaviour, Figure 3.10 shows that the polytropic efficiency tends to decrease with increasing pressure ratio, based on empirical relations. If the pressure ratio is increased from 5 to 8, the polytropic efficiency decreases with approximately 0.3%. This means that the isentropic efficiency will be decreased by 0.8 %, according to Equation 3.20. This decreased isentropic efficiency means that during compression, more entropy is being created, leading to a lower thermal efficiency. The effects of the isentropic efficiency on the APPU engine cycle have been calculated in *Python*, and is visualised in Figure 8.1.

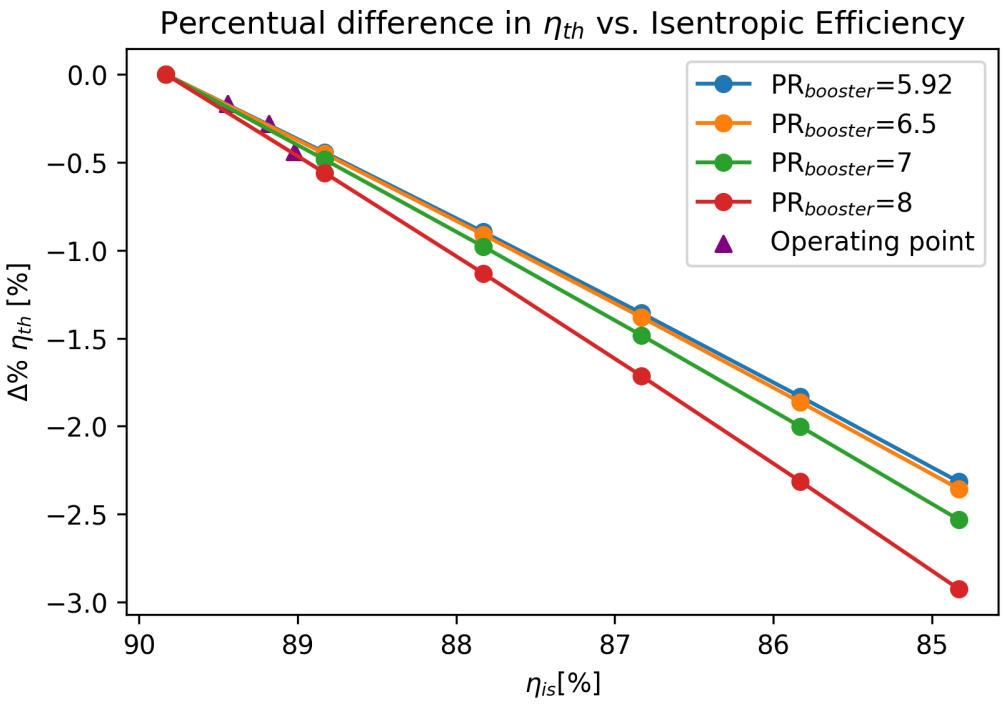

Figure 8.1: The *percentual* decrease in thermal efficiency of the APPU engine cycle when the isentropic efficiency decreases

It can be observed that the percentual decrease in thermal efficiency is minimal. A percentual decrease of 0.44% in thermal efficiency, at a booster pressure ratio of 8 doesn't marginalise the percentual increase (of 10.96% Figure 7.13) that is achieved by this new cycle.

8.5. BLI effect

This research focussed mainly on the thermodynamics of the engine cycle and the effect of BLI has not been taken into account for the thrust calculations. Rather, thrust that has been calculated using propeller maps. This is a crude approximation of reality and does by no means approach the accuracy that might be obtained from other methods such as CFD calculations, let alone when a BLI is included. This affects mainly the final calculations that have been described in Section 5.9, and wouldn't have a significant effect on the thermodynamic calculations.

9

Conclusions

Having conducted multiple simulations and after analysing and verifying the results, a number of conclusions can be drawn and the research questions stated in Chapter 2 can be answered.

- The first sub-question is: "*How does the cooling system influence the efficiency of an engine?*" The hydrogen baseline engine has a thermal efficiency and a PSFC of 49.8 % and 0.0597 kg/kWh at cruise, respectively, while the kerosene engine has a thermal efficiency and a PSFC of 48.3% and 0.167 kg/kWh, respectively. Using the hydrogen fuel to cool the bleed flow and adequately decreasing it, results into a thermal efficiency of 49.9 % and a PSFC of 0.0596 kg/kWh.

  Increasing the TIT to 1840 K together with cooling the bleed flow to 273.5 K leads to a required bleed flow that equals the amount of bleed flow in the (uncooled) baseline case. This increases the thermal efficiency to 50.7 % and the PSFC to 0.0590 kg/kWh.

  Using the hydrogen fuel to facilitate intercooling while subsequently increasing the pressure ratios of the booster and the HPC until a HPC outlet temperature is reached similar to the baseline, a thermal efficiency of 53.5 % and a PSFC of 0.0539 kg/kWh can be reached, given the optimistic assumption that the polytropic efficiency of the compressors stays constant.

- The second sub-question is: "*What sort of heat exchangers can be used in cooling aero engines with cryogenic hydrogen?*" The type of heat exchangers that is most suitable in aviation, using cryogenic hydrogen are the "Tube-Fin" heat exchanger (which is a subdivision of the extended surface heat exchangers) with 9.1-0.737-S as its surface designation as provided by Kays & London [12], due to its compactness, low pressure drops, tolerance against vibrations and its usability of cryogenics. Moreover, the heat exchanger that is made of aluminium alloy Al-3003 offers the best perspective, due to its adequate temperature limit and its high thermal conductivity.

- The third sub-question is: "*How much fuel does the altered engine burn during cruise?*" Having made the assumption that for every percent of increased APPU thrust fraction (Φ_{APPU}), a percent less fuel has to be burnt by the main engine, the estimate of fuel saved per flight is 3.2 kg for the SBC-case, 20.8 kg for the Increased TIT-case and 210 kg for the Intercooled-case.

- The fifth sub-question is: "*What should the sizing be of the heat exchanger in the new design?*" Two different heat exchangers have been designed, one to cool the bleed air and another one to intercool the core flow between the two compressors. The bleed heat exchanger is designed in a rectangular shape, while the intercooling heat exchanger has been designed in annular fashion. Both heat exchangers use the same surface designation 9.1-0.737-S, using the aluminium alloy Al-3003. The bleed heat exchanger has a height, depth and width of 36 cm, 16 cm and 10 cm, respectively. The intercooling heat exchanger on the other hand has an inner radius, outer radius and depth of 11 cm, 35 cm and 17 cm respectively. This means that the volume of the intercooling heat exchanger is approximately 10 times larger than the bleed heat exchanger.

- The sixth sub-question is: "*What is the effect of adding a heat exchanger on the mass?*" The bleed heat exchanger has a mass of 2.2 kg, while the intercooling heat exchanger has a mass of 22.0 kg. As calculated by van Schie [63] the core mass of the APPU is estimated to be around 502 kg (which differs for different designs). This means that adding the bleed heat exchanger increases the APPU mass with 0.44 %, while adding an intercooling heat exchanger increases the APPU mass with 4.4 %.

10

Recommendations

Cooling the bleed flow leads to a higher core flow which decreases the PSFC and increases the thermal efficiency. However, the designer can also opt to decrease the mass flow, the thermal efficiency and the PSFC would stay more or less constant, but the intake area of the APPU could decrease, decreasing mass, thus saving fuel. If the core flow is decreased by the amount that is saved by needed less bleed air due to cooling, ($\Delta \dot{m}_{bleed}$), the area can be decreased by approximately 1.174 %, meaning that the diameter if the core can decrease with 1.08 %. The amount of mass that is reduced by this reduction in diameter, and the effect of drag could be further analysed using computational fluid dynamics.

Another improvement that could be made is to introduce the pressure losses coming from the HEX and the diffuser into the bleed air. The current model only takes the pressure losses into account when an intercooler is used, and not for the bleed flow. The reason being that because the bleed that flows through the diffuser and subsequently the HEX, is connected to the HPT, which is currently not adapted for pressure changes in the bleed air. Furthermore, one should keep in mind that if the pressure losses of the diffuser and HEX are higher than the pressure losses that the core flow encounters in the combustion chamber, there will be a presence of reserved flow, which the model should be appropriately adapted for.

Furthermore, if hydrogen is used as means of bleed cooling its temperature increases from 20 K to approximately 84 K, which means that the hydrogen still has a lot of potential. The auto-ignition temperature of hydrogen at 1 atmosphere lies around 858 K, which means that the fuel temperature can be increased to a much greater extend. Moreover, the specific heat capacity of hydrogen at 13.3 bar (which is the pressure at which the combustion chamber combusts the fuel at cruise) lies between 11.5 $\frac{kJ}{kg \cdot K}$ and 15 $\frac{kJ}{kg \cdot K}$. This means that the hydrogen can still absorb a lot of heat. Considering the massive effect that heating the fuel temperature has on the system performance, the effect of adding a recuperation system at the nozzle should be investigated, as a lot of heat is wasted that could be added to back into the system using hydrogen as a carrier.

Another case that should be investigated is the inclusion of an extra turbine to include a bottoming cycle, such as an Organic Rankine cycle. If high pressure, high temperature hydrogen is used, this extra turbine would then expand the hydrogen (through which its temperature decreases) through which power can be generated. This extra turbine could be connected to a generator which provides the aircraft with electrical energy, alleviating the power off-take from the HPT, which means the total power output would be more. The fuel is to be stored at a pressure higher than the pressure in the combustion chamber (which is approximately 13.3 bar at cruise) to prevent reserved flow. However, since the critical pressure and temperature of hydrogen are 12.9 bar and 33 K respectively, the fuel will be in supercritical state. This means that either:

- The overall pressure ratio has to be decreased, which subsequently lowers the system performance.
- The added bottoming cycle should be a *supercritical* ORC, in which the turbine model utilises maps that represent supercritical hydrogen accurately.

Adding a bottoming cycle comes with an increased complexity and increased weight, which means that additional calculations should be conducted on the effect of the increased weight on the aircraft performance, to find out whether the additional ORC is worth the addition of weight.

A

GasTurb input data

Property	*Unit*	*Value*	*Comment*
Inlet Corr. Flow W2Rstd	kg/s	9,00203	
Intake Pressure Ratio		0,98	
Booster Press. Ratio		5,92	
Compr. Interduct Press. Ratio		0,985	
HP Compressor Pressure Ratio		5,92	
Burner Exit Temperature	K	1700	
Burner Design Efficiency		0,99	
Burner Partload Constant		1,6	used for off design only
Fuel Heating Value	MJ/kg	119,961	
Overboard Bleed	kg/s	0	
HP Spool Power Offtake	kW	200	
HP Spool Mechanical Efficiency		0,99	
IP Spool Mechanical Efficiency		0,99	
LP Spool Mechanical Efficiency		0,99	
Nominal PT Spool Speed	RPM	5000	used for off design only
Burner Pressure Ratio		0,95	
IPT Interd. Ref. Press. Ratio		0,99	
PT Interd. Ref. Press. Ratio		0,99	
Turbine Exit Duct Press Ratio		0,98	
Exhaust Pressure Ratio P8/Pamb		1,2	

(a) Basic data

Property	*Unit*	*Value*	*Comment*
Rel. Handling Bleed		0	
Rel. Overboard Bleed W_Bld/W25		0	
Rel. Enthalpy of Overb. Bleed		0	
Recirculating Bleed W_reci/W25		0	Off Design Input Only
Rel. Enthalpy of Recirc Bleed		1	
Number of HP Turbine Stages		1	
HPT NGV 1 Cooling Air / W25		0,0221	
HPT Rotor 1 Cooling Air / W25		0,0184	
HPT Cooling Air Pumping Dia	m	0	
Number of IP Turbine Stages		1	
IPT NGV 1 Cooling Air / W25		0	
IPT Rotor 1 Cooling Air / W25		0	
Rel. Enth. of IPT Cooling Air		0,7	
Number of PT Stages		3	
PT Rotor Cool Air W_Cl_PT/W25		0	
Rel. Enth. of PT Cooling Air		0	
Rel. HP Leakage to PT exit		0	

(b) Secondary air system

Figure A.1: Input parameters GasTurb at cruise (hydrogen)

B

Map data

Table B.1: HPC map, not normalised (β_{design} = 9.5)

	N																				
	Mass Flow	0																			
β	0	0	1	2	3	4	5	6	7	8	9	10	11	12	13	14	15	16	17	18	19
	0.5	10.38683	10.23236	10.0563	9.87849	9.69593	9.50797	9.30393	9.10332	8.89518	8.67522	8.44689	8.21855	7.98237	7.75325	7.50371	7.25881	7.01299	6.76902	6.53247	6.2987
	0.6	13.46753	13.36364	13.24861	13.08534	12.90724	12.7013	12.48052	12.23791	12.00186	11.74954	11.48237	11.21521	10.93321	10.64564	10.33952	10.02783	9.71614	9.40445	9.07792	8.75139
	0.7	17.77922	17.74583	17.63451	17.50093	17.3525	17.15955	16.93692	16.6846	16.4026	16.09091	15.76438	15.42975	15.06679	14.68089	14.28942	13.89357	13.46237	13.03117	12.60297	12.20223
	0.75	20.46382	20.41373	20.35442	20.24675	20.11317	19.95663	19.76252	19.52876	19.2616	18.96104	18.62709	18.27644	17.89239	17.46928	17.00742	16.52657	16.02937	15.53803	15.03711	14.55288
	0.8	23.5974	23.54731	23.44243	23.33024	23.19666	23.02968	22.84601	22.63741	22.41187	22.16141	21.89425	21.57699	21.24304	20.8423	20.37477	19.85714	19.3067	18.67161	18.00371	17.3859
	0.85	26.38548	26.3161	26.24671	26.17733	26.10019	25.99224	25.89239	25.77365	25.62523	25.46197	25.26902	25.06122	24.79406	24.51206	24.15584	23.76994	23.30983	22.68646	21.94434	21.12801
	0.9	28.92022	28.88683	28.8423	28.79777	28.75325	28.69605	28.65373	28.5897	28.51632	28.44293	28.37477	28.27458	28.16327	28.01855	27.78479	27.48423	27.05799	26.50464	25.89239	25.14286
	0.95	31.44805	31.42208	31.3961	31.36364	31.33117	31.29221	31.25284	31.19943	31.14935	31.09091	31.02597	30.95455	30.86364	30.75974	30.62987	30.47403	30.23377	29.94156	29.62385	29.24026
	1	33.6475	33.64007	33.62894	33.6141	33.59926	33.58071	33.56215	33.5436	33.52134	33.49907	33.46939	33.43599	33.39147	33.33581	33.25788	33.1577	33.00318	32.80519	32.60482	32.38367
	1.05	35.19239	35.18033	35.16456	35.14972	35.13488	35.12096	35.10612	35.09221	35.07847	35.06289	35.04675	35.03117	35.01336	34.9961	34.97857	34.95962	34.93933	34.91929	34.8974	34.87421
	Efficiency																				
β	0	0	1	2	3	4	5	6	7	8	9	10	11	12	13	14	15	16	17	18	19
	0.5	0.65395	0.6715	0.68233	0.6897	0.69511	0.69917	0.70158	0.70308	0.70398	0.70418	0.70349	0.70173	0.69833	0.69391	0.68749	0.68097	0.6739	0.66699	0.66038	0.65406
	0.6	0.67053	0.69108	0.71063	0.72541	0.73719	0.74421	0.74822	0.74997	0.74972	0.74872	0.74596	0.7417	0.73694	0.73068	0.72341	0.71514	0.70637	0.69734	0.68695	0.67757
	0.7	0.72354	0.7475	0.76561	0.77965	0.7911	0.79865	0.80195	0.80385	0.80346	0.80075	0.79714	0.79185	0.78541	0.77741	0.76876	0.75979	0.74881	0.73706	0.72536	0.71564
	0.75	0.75886	0.77734	0.79288	0.80416	0.81368	0.8202	0.82396	0.82596	0.82647	0.82546	0.82346	0.82045	0.81594	0.80942	0.80115	0.79138	0.7801	0.76882	0.75629	0.74376
	0.8	0.79561	0.8097	0.82107	0.82935	0.83541	0.84043	0.84419	0.84662	0.84823	0.84857	0.84799	0.84639	0.84316	0.83737	0.82875	0.81865	0.80687	0.79358	0.78005	0.76727
	0.85	0.81807	0.82579	0.83211	0.83807	0.84386	0.84834	0.85276	0.85649	0.85895	0.86	0.86013	0.85947	0.85737	0.85456	0.85035	0.84534	0.83825	0.82804	0.81474	0.80012
	0.9	0.81977	0.82985	0.83872	0.84517	0.8503	0.85494	0.85902	0.86218	0.86444	0.86613	0.86669	0.86609	0.86489	0.86308	0.85997	0.85657	0.85145	0.84454	0.83702	0.82738
	0.95	0.81677	0.82714	0.83556	0.84308	0.84912	0.85466	0.85902	0.86233	0.86504	0.86639	0.86684	0.86654	0.86534	0.86338	0.86098	0.85797	0.85436	0.85075	0.84564	0.84173
	1	0.79965	0.81298	0.82417	0.83368	0.84124	0.84812	0.85299	0.85611	0.85865	0.85975	0.86045	0.86045	0.86015	0.85912	0.85772	0.85544	0.85333	0.85035	0.84667	0.84164
	1.05	0.77587	0.78316	0.79123	0.79789	0.80526	0.81158	0.81712	0.82255	0.82707	0.83095	0.8347	0.83797	0.84087	0.84314	0.84506	0.84662	0.84692	0.84586	0.84271	0.83517
	Pressure ratio																				
β	0	0	1	2	3	4	5	6	7	8	9	10	11	12	13	14	15	16	17	18	19
	0.5	1.38577	1.44768	1.50467	1.55906	1.6104	1.65851	1.70165	1.74268	1.77985	1.81229	1.84044	1.8657	1.88659	1.9059	1.91828	1.92855	1.93561	1.94007	1.94321	1.94409
	0.6	1.77778	1.86684	1.95273	2.0294	2.10136	2.16614	2.22552	2.27796	2.32841	2.3726	2.41055	2.44505	2.47301	2.49621	2.51172	2.5222	2.52887	2.53175	2.52732	2.51901
	0.7	2.42348	2.55507	2.67226	2.78366	2.89022	2.98576	3.07243	3.14967	3.21697	3.27381	3.32309	3.36617	3.39812	3.41986	3.43538	3.44494	3.44056	3.43105	3.41726	3.40587
	0.75	2.88271	3.03211	3.17892	3.31501	3.44399	3.56595	3.67716	3.77636	3.86428	3.94031	4.00387	4.05866	4.10011	4.12624	4.1366	4.13611	4.1253	4.11025	4.08671	4.0622
	0.8	3.47425	3.64853	3.81024	3.96865	4.12035	4.26204	4.39706	4.52301	4.64142	4.74986	4.85008	4.93254	5.00578	5.05514	5.07958	5.08315	5.07047	5.02546	4.96328	4.90942
	0.85	4.05085	4.24362	4.43523	4.62568	4.81304	4.99123	5.16979	5.34157	5.50313	5.65805	5.80164	5.93775	6.05237	6.15831	6.23631	6.29957	6.33293	6.30556	6.23073	6.1227
	0.9	4.61613	4.83851	5.05754	5.2758	5.49329	5.70655	5.92301	6.13244	6.33797	6.54226	6.74694	6.9401	7.12789	7.3025	7.4439	7.55806	7.6226	7.63497	7.61851	7.54363
	0.95	5.21884	5.46513	5.71096	5.95455	6.19756	6.43811	6.67785	6.91256	7.14739	7.37861	7.60665	7.83132	8.04792	8.25829	8.45736	8.64449	8.79678	8.92504	9.03867	9.12101
	1	5.77492	6.04588	6.31568	6.58421	6.85247	7.11932	7.38584	7.65202	7.91662	8.18082	8.44201	8.70133	8.95594	9.20556	9.44559	9.67546	9.88171	10.0675	10.24897	10.41827
	1.05	6.18312	6.46704	6.74967	7.03229	7.31463	7.59698	7.87878	8.16061	8.44224	8.72297	9.00321	9.28336	9.56237	9.84127	10.11973	10.3973	10.67396	10.95035	11.22557	11.4998

Table B.2: IPC map, not normalised (β_{design} = 7.6)

	N																				
Mass flow																					
β	0	0	1	2	3	4	5	6	7	8	9	10	11	12	13	14	15	16	17	18	19
	0.359	124.658	121.756	118.854	115.952	113.05	110.07	106.94243	103.6	100.04	96.238	92.2288	88.1306	84.0563	80.0069	76.0416	72.1434	68.2807	64.4179	60.5552	56.6924
	0.528	159.947	158.078	156.14	153.984	151.634	149.147	146.27401	143.165	139.789	136.096	132.292	128.411	124.454	120.427	116.375	112.293	108.211	104.13	100.048	95.9664
	0.661	191.179	190.106	189.025	187.586	186.124	184.237	182.22597	179.768	177.022	174.041	170.751	167.352	163.754	159.983	156.119	152.056	147.975	143.894	139.813	135.731
	0.791	223.802	223.781	223.557	223.333	222.918	222.27	221.56322	220.314	219.013	217.076	215.01	212.5	209.786	206.707	203.373	199.746	195.844	191.704	187.563	183.423
	0.88	251.99	251.99	251.99	251.951	251.89	251.81	251.39489	250.98	250.164	249.219	247.785	246.211	244.097	241.878	239.188	236.311	233.061	229.549	225.757	221.965
	0.952	274.921	274.921	274.921	274.921	274.921	274.921	274.90015	274.832	274.674	274.309	273.742	272.966	271.768	270.342	268.674	266.593	264.282	261.742	258.762	255.78
	1	289.956	289.956	289.956	289.956	289.956	289.956	289.956	289.956	289.956	289.902	289.791	289.434	288.877	288.063	286.964	285.601	283.96	281.996	279.749	277.45
	1.028	295.367	295.367	295.367	295.367	295.367	295.367	295.367	295.367	295.367	295.367	295.327	295.158	294.823	294.27	293.457	292.383	291.057	289.472	287.627	285.728
	1.144	313.93	313.93	313.93	313.93	313.93	313.93	313.9295	313.93	313.93	313.93	313.93	313.93	313.885	313.796	313.662	313.386	312.886	312.295	311.553	310.803
Efficiency																					
β	0	0	1	2	3	4	5	6	7	8	9	10	11	12	13	14	15	16	17	18	19
	0.359	-2.2016	-1.2246	-0.5727	-0.143	0.15738	0.37411	0.53422	0.6505	0.72569	0.76754	0.78904	0.79595	0.79617	0.79078	0.78185	0.76968	0.75349	0.73236	0.70691	0.67762
	0.528	0.14171	0.31251	0.45157	0.56155	0.64785	0.71562	0.76491	0.79737	0.81328	0.82081	0.82336	0.8219	0.81707	0.80978	0.80034	0.78918	0.77599	0.75589	0.73584	0.71078
	0.661	0.45429	0.54588	0.62478	0.68708	0.74015	0.78035	0.81018	0.82807	0.83789	0.8407	0.84048	0.83776	0.83241	0.82495	0.81593	0.80517	0.79298	0.77719	0.76053	0.74035
	0.791	0.55133	0.61502	0.66861	0.71648	0.75647	0.78861	0.81608	0.83368	0.84504	0.84962	0.85053	0.84842	0.84481	0.83789	0.82887	0.81758	0.80566	0.79386	0.7807	0.76754
	0.88	0.58742	0.63419	0.677	0.71477	0.7484	0.77879	0.80391	0.82436	0.8388	0.84842	0.85263	0.85415	0.85285	0.85042	0.84566	0.83965	0.83188	0.82286	0.81208	0.80027
	0.952	0.59161	0.62825	0.6634	0.69501	0.72398	0.7507	0.77486	0.79583	0.81411	0.82856	0.83948	0.84701	0.85021	0.85156	0.85132	0.84887	0.84518	0.84033	0.8337	0.82689
	1	0.59311	0.62569	0.65576	0.6834	0.70822	0.73146	0.75342	0.77392	0.79233	0.80857	0.82269	0.83319	0.84071	0.84526	0.84741	0.84799	0.84701	0.8446	0.84092	0.83683
	1.028	0.59132	0.62153	0.64956	0.67561	0.69841	0.72092	0.74044	0.75923	0.77712	0.79379	0.80808	0.8201	0.82966	0.83636	0.8402	0.84216	0.84285	0.84216	0.84027	0.83794
	1.144	0.55993	0.58794	0.61411	0.63863	0.66179	0.68241	0.70227	0.7196	0.73587	0.74994	0.76316	0.775	0.78531	0.79484	0.80361	0.81088	0.81703	0.82076	0.82265	0.82341
Pressure ratio																					
β	0	0	1	2	3	4	5	6	7	8	9	10	11	12	13	14	15	16	17	18	19
	0.359	0.92409	0.94734	0.96963	0.99096	1.01134	1.03053	1.04829	1.06435	1.07862	1.09093	1.10134	1.11018	1.11784	1.12432	1.12985	1.13438	1.13781	1.13998	1.14089	1.14053
	0.528	1.02208	1.05309	1.08321	1.11185	1.13901	1.16485	1.18827	1.20977	1.22913	1.24602	1.26129	1.27504	1.28725	1.29792	1.30725	1.31519	1.32188	1.32732	1.33149	1.3344
	0.661	1.13784	1.17678	1.21531	1.25178	1.28764	1.32089	1.35288	1.38187	1.40852	1.43302	1.45487	1.47509	1.49313	1.50907	1.52333	1.53523	1.54583	1.55521	1.56338	1.57032
	0.791	1.28787	1.3376	1.38622	1.43475	1.4821	1.52789	1.5731	1.61464	1.65541	1.69154	1.72617	1.75708	1.78578	1.81105	1.83355	1.85292	1.86922	1.8826	1.89482	1.90586
	0.88	1.44146	1.49658	1.55171	1.60658	1.6613	1.71585	1.76806	1.82012	1.86911	1.91685	1.96055	2.00269	2.04006	2.07593	2.10726	2.13624	2.16125	2.1831	2.20155	2.21894
	0.952	1.58279	1.64213	1.70147	1.7608	1.82014	1.87947	1.93865	1.99745	2.05553	2.11185	2.16638	2.21895	2.26762	2.3139	2.35757	2.39698	2.43365	2.46747	2.49641	2.52445
	1	1.68344	1.74549	1.80755	1.86961	1.93167	1.99373	2.05579	2.11784	2.1799	2.2415	2.30258	2.36145	2.41837	2.47274	2.52417	2.57273	2.61817	2.65993	2.69827	2.73541
	1.028	1.7212	1.78423	1.84726	1.91029	1.97332	2.03635	2.09938	2.16241	2.22544	2.28847	2.35115	2.41265	2.47255	2.53032	2.58541	2.6377	2.68715	2.7336	2.77692	2.81912
	1.144	1.85698	1.92331	1.98964	2.05598	2.12231	2.18864	2.25497	2.3213	2.38763	2.45396	2.52029	2.58663	2.65253	2.71797	2.78294	2.8464	2.90744	2.96736	3.02546	3.08323

Table B.3: HPT map, not normalised ($\beta_{design} = 9.5$)

	N																			
	Mass flow																			
β	0	0	1	2	3	4	5	6	7	8	9	10	11	12	13	14	15	16	17	18	19
	0.8	2.865311	2.947129	3.014593	3.066268	3.100718	3.120096	3.132091	3.138038	3.140909	3.141627	3.141627	3.141627	3.141627	3.141627	3.141627	3.141627	3.141627	3.141627	3.141627	3.141627
	0.9	2.863688	2.94067	3.00735	3.059091	3.091746	3.111483	3.124376	3.130861	3.133014	3.133732	3.133732	3.133732	3.133732	3.133732	3.133732	3.133732	3.133732	3.133732	3.133732	3.133732
	1	2.868182	2.942793	3.004785	3.048325	3.077751	3.099282	3.110765	3.117538	3.120096	3.120813	3.120813	3.120813	3.120813	3.120813	3.120813	3.120813	3.120813	3.120889	3.120813	3.120813
	1.05	2.87892	2.948119	3.005324	3.045695	3.073645	3.093223	3.104187	3.110687	3.113354	3.114357	3.114523	3.114534	3.114682	3.114713	3.114713	3.114713	3.114723	3.114741	3.114713	3.114713
	1.1	2.889118	2.953748	3.006699	3.0437	3.069856	3.087799	3.097927	3.104306	3.106858	3.108085	3.10826	3.108254	3.108613	3.108613	3.108613	3.108613	3.108613	3.108613	3.108613	3.108613
	Efficiency																				
β																					
	0	0	1	2	3	4	5	6	7	8	9	10	11	12	13	14	15	16	17	18	19
	0.8	0.862687	0.864444	0.866149	0.866418	0.865771	0.86479	0.862687	0.860199	0.856484	0.851741	0.846667	0.840299	0.832836	0.823582	0.813765	0.801824	0.787496	0.772518	0.756915	0.741972
	0.9	0.874129	0.87728	0.880597	0.883085	0.885406	0.887065	0.887562	0.887562	0.886397	0.883723	0.880066	0.875059	0.867662	0.859204	0.848955	0.837114	0.824192	0.809166	0.794163	0.77872
	1	0.875415	0.883389	0.890298	0.896617	0.902126	0.906343	0.909302	0.910897	0.911096	0.910448	0.908106	0.90398	0.89814	0.890672	0.880597	0.869289	0.855505	0.841045	0.825184	0.809702
	1.05	0.880042	0.887722	0.894605	0.900888	0.906177	0.910082	0.912786	0.914507	0.914834	0.91408	0.911949	0.908657	0.903284	0.896418	0.887761	0.877313	0.866269	0.853433	0.839104	0.824776
	1.1	0.880864	0.889169	0.895721	0.901857	0.906833	0.910315	0.912757	0.914751	0.915124	0.914419	0.912757	0.909435	0.904842	0.898043	0.890498	0.88063	0.869353	0.858076	0.844435	0.829995
	Pressure ratio																				
β	0	0	19																		
	0.9	1.54645	3.894654																		
	1	1.56539	3.99108																		
	1.05	1.576022	4.027623																		
	1.1	1.587428	4.056386																		

Table B.4: IPT map, not normalised (β_{design} = 9.5)

	N																			
	Mass flow																			
β	0	0	1	2	3	4	5	6	7	8	9	10	11	12	13	14	15	16	17	18	19
	0.5	28.36761	33.04518	37.45501	41.4653	44.93573	47.89203	50.5527	52.86632	55.02571	56.88946	58.56041	59.97429	61.13111	62.15424	63.08997	63.80977	64.45758	64.99743	65.42931	65.7892
	0.6	29.58869	34.70671	39.57584	43.8946	47.37789	50.64267	53.3419	55.77121	57.78278	59.46015	60.91902	62.2108	63.18252	63.96421	64.58612	65.15811	65.58962	65.90201	66.21441	66.427
	0.7	32.98639	38.22622	42.63496	46.6838	49.92288	52.98201	55.29563	57.44861	59.13239	60.57198	61.74165	62.69923	63.52185	64.21594	64.7108	65.06427	65.37275	65.61954	65.80463	65.89717
	0.8	36.7428	42.13368	46.14396	49.53728	52.51928	55.08997	57.14653	58.99743	60.43702	61.52297	62.49357	63.35219	63.96915	64.4372	64.8072	65.03856	65.21832	65.34079	65.44987	65.50129
	0.9	41.74807	45.79692	49.34447	52.18509	54.66581	56.59383	58.36761	59.8329	61.06427	62.02057	62.80206	63.43188	63.93316	64.29049	64.55013	64.74293	64.86632	64.96915	65.01028	65.03085
	1	45.22975	48.40617	51.37532	53.80463	55.96401	57.67352	59.11311	60.34447	61.36247	62.17224	62.77863	63.3419	63.7635	64.04627	64.25193	64.41902	64.52699	64.58098	64.61697	64.63496
	1.1	47.07584	50.31491	52.90488	54.94216	56.6838	58.21337	59.46572	60.5527	61.45244	62.14139	62.71208	63.16195	63.49871	63.7455	63.91517	64.05398	64.13165	64.16395	64.19624	64.217
											124.9509	62.475435									
	Efficiency																				
β	0	0	1	2	3	4	5	6	7	8	9	10	11	12	13	14	15	16	17	18	19
	0.5	0.83882	0.89152	0.91272	0.9153	0.91337	0.90887	0.9018	0.8928	0.8838	0.87674	0.86967	0.86195	0.85488	0.84846	0.84203	0.83625	0.83111	0.82653	0.82147	0.81618
	0.6	0.77262	0.86756	0.90244	0.91722	0.91979	0.91851	0.91272	0.90823	0.9018	0.89602	0.88959	0.88316	0.87738	0.87209	0.8671	0.86055	0.85585	0.85158	0.84717	0.84203
	0.7	0.76491	0.86388	0.9063	0.91722	0.92067	0.92108	0.92026	0.91658	0.91326	0.90915	0.90504	0.89906	0.89537	0.89063	0.88626	0.88159	0.87738	0.87172	0.8671	0.86347
	0.8	0.79769	0.87057	0.90161	0.91594	0.92172	0.92545	0.92558	0.9241	0.92108	0.91793	0.9153	0.91165	0.90835	0.90437	0.90026	0.89621	0.89081	0.88638	0.88252	0.87738
	0.9	0.82596	0.87416	0.90051	0.91465	0.92108	0.92558	0.92751	0.92751	0.92622	0.92494	0.92044	0.91787	0.91401	0.91015	0.9063	0.90242	0.89859	0.89409	0.8902	0.88638
	1	0.82186	0.86645	0.89473	0.90884	0.91841	0.92303	0.92612	0.92735	0.92766	0.92674	0.92437	0.92087	0.91717	0.91319	0.90946	0.90514	0.90113	0.8966	0.89249	0.88838
	1.1	0.81183	0.85553	0.88316	0.89987	0.9108	0.9182	0.92301	0.92558	0.92643	0.92519	0.92314	0.92026	0.91697	0.91285	0.90833	0.90422	0.89969	0.89558	0.89105	0.88732
	PR																				
β	0	0	19																		
	0.5	1.05729	1.67197																		
	0.6	1.05949	1.84878																		
	0.7	1.07821	2.00437																		
	0.8	1.11344	2.13874																		
	0.9	1.1628	2.25211																		
	1	1.2038	2.3465																		
	1.1	1.23092	2.4224																		

Table B.5: LPT map, not normalised (β_{design} = 9.8)

	N															
	Mass flow															
		0	0.07143	0.14286	0.21429	0.28571	0.35714	0.42857	0.5	0.57143	0.64286	0.71429	0.78571	0.85714	0.92857	1
β	0	0	1	2	3	4	5	6	7	8	9	10	11	12	13	14
	0.6	70.37594	79.89975	86.61654	91.63452	95.31143	98.83739	101.3778	103.4498	105.1887	106.6541	107.8847	108.7594	109.4887	110.0652	110.5163
	0.7	77.5188	88.17043	95.30702	100.5764	104.08521	106.33	107.9699	109.0977	109.9561	110.6579	111.1404	111.5351	111.886	112.1369	112.3046
	0.8	82.61905	94.04762	100.3002	104.6742	106.93042	108.6725	109.7318	110.4887	111.0902	111.5764	111.9373	112.1378	112.2983	112.3845	112.4559
	0.9	87.44039	97.18222	102.5439	106.0526	108.28575	109.7368	110.5433	111.1053	111.4737	111.7544	111.9649	112.0877	112.1579	112.2018	112.2105
	1	91.96417	99.43609	103.7218	106.6617	108.60902	109.6617	110.3384	110.9211	111.2895	111.5451	111.7481	111.8534	111.891	111.9173	111.9173
	1.1	95.18498	100.5639	103.8722	106.3534	108.04045	109.0602	109.7986	110.4642	110.9232	111.2287	111.391	111.5263	111.6015	111.6316	111.6316
	1.2	97.85714	101.7669	104.2954	106.0536	107.38247	108.3466	109.1479	109.8399	110.3541	110.7293	110.985	111.1805	111.2857	111.3459	111.3609
	Efficiency															
β	0	0	1	2	3	4	5	6	7	8	9	10	11	12	13	14
	0.6	0.82112	0.8933	0.9114	0.91096	0.89902	0.88622	0.87285	0.86033	0.8483	0.83627	0.82423	0.8144	0.8037	0.79301	0.78231
	0.7	0.83766	0.90583	0.91585	0.91184	0.90094	0.88534	0.87301	0.86082	0.84909	0.83824	0.82874	0.81992	0.81153	0.80315	0.79477
	0.8	0.82964	0.90683	0.92123	0.92187	0.91474	0.90301	0.8923	0.88227	0.87325	0.86372	0.85567	0.84841	0.84095	0.83524	0.82953
	0.9	0.80558	0.8953	0.92086	0.92788	0.92888	0.92487	0.91886	0.91134	0.90432	0.89731	0.89013	0.88216	0.87416	0.86616	0.85816
	1	0.7814	0.87285	0.90952	0.92637	0.93338	0.93439	0.93278	0.92997	0.92637	0.92192	0.91726	0.91236	0.90633	0.9003	0.89388
	1.1	0.75263	0.84211	0.89023	0.91429	0.92623	0.93383	0.93825	0.93982	0.94	0.9386	0.93614	0.93298	0.9294	0.92526	0.92105
	1.2	0.73083	0.81203	0.85414	0.88195	0.90301	0.91579	0.92448	0.93135	0.93643	0.93951	0.94102	0.94124	0.94094	0.94027	0.93917
	PR															
β	0	0	14													
	0.6	1.17461	2.11055													
	0.7	1.23847	2.80304													
	0.8	1.31249	3.31182													
	0.9	1.39667	3.63689													
	1	1.491	3.77825													
	1.1	1.59549	3.73589													
	1.2	1.71013	3.50983													

C

Dymola models icons

(a) Environment

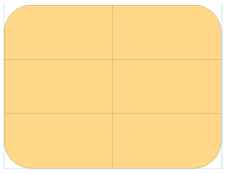

(b) Map

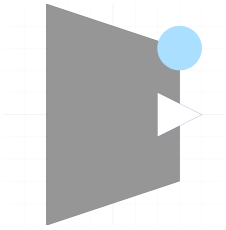

(c) Air intake

(d) Pressure drop (air)

(e) Source flow (overboard bleed)

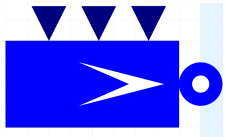

(f) Source flow (fuel)

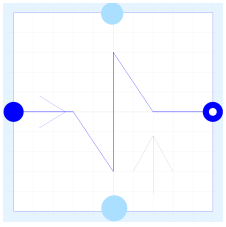

(g) Heat exchanger

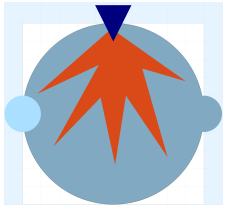

(h) Combustor

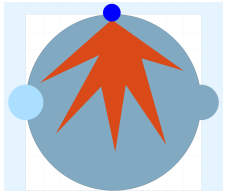

(i) Combustor altered

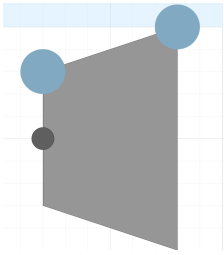

(j) Turbine

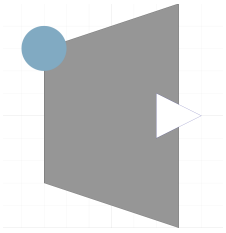

(k) Nozzle

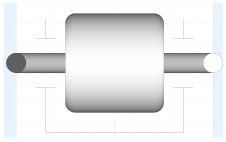

(l) Shaft inertia

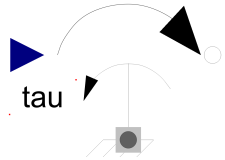

(m) Torque source

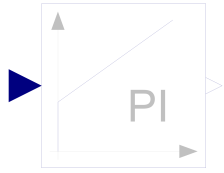

(n) PI controller

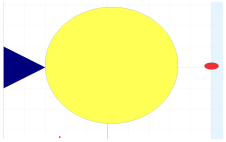

(o) Power off-take

(p) Pressure drop (exhaust)

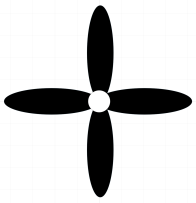

(q) Propeller

Figure C.1: Icons of sub-models

D

Heat Exchanger Surface Geometry

Surface designation	Tube arrangement	Fin type	Tube length (parallel to flow)		Tube width (normal to flow)		Fins/in	Hydraulic diameter $4r_h$		Fin thickness δ		Free flow/ frontal area σ	Heat transfer area/ total volume α		Fin area/ total area
			in	10^{-3}m	in	10^{-3}m		ft	10^{-3}m	in	10^{-3}m		ft^2/ft^3	m^2/m^3	
9.68–0.87	In-line	Plain	0.870	22.1	0.120	3.0	9.68	0.01180	3.60	0.004	0.102	0.697	229	751	0.795
9.1–0.737S	Staggered	Plain	0.737	18.7	0.100	2.5	9.1	0.01380	4.21	0.004	0.102	0.788	224	735	0.813
9.68–0.87R	In-line	Ruffled	0.870	22.1	0.120	3.0	9.68	0.01180	3.60	0.004	0.102	0.697	229	751	0.795
9.21–0.737SR	Staggered	Ruffled	0.737	18.7	0.100	2.5	9.29	0.01352	4.12	0.004	0.102	0.788	228	748	0.814
11.32–0.737SR	Staggered	Ruffled	0.737	18.7	0.100	2.5	11.32	0.01152	3.51	0.004	0.102	0.780	270	886	0.845

Figure D.1: Geometries of flat tubes with continuous fins

Bibliography

[1] Çengel Yunus A and Michael A. Boles. *THERMODYNAMICS: AN ENGINEERING APPROACH*. McGraw Hill Education, 2013.

[2] Tiedo Tinga Savad Shakariyants Francesco Montella Jos P. van Buijtenen, Wilfried P.J. Visser. *Aero Engine Technology, AE4–238*. Faculty of Aerospace Engineering, TU Delft, 2018.

[3] T. K. Ibrahim, M. M. Rahman, and A. N. Abd Alla. Study on the effective parameter of gas turbine model with intercooled compression process. 2010.

[4] S. L. Dixon and C. A. Hall. *Fluid Mechanics and Thermodynamics of Turbomachinery*. Elsevier Inc., 7th edition, 2014.

[5] Cody Allen, Purushotham Balaji, and Maurício Oliveira. Axial compressor fouling and its effect on gas turbine fuel consumption and emissions. 09 2020.

[6] *The Potential of GT Combined Cycles for Ultra High Efficiency*, volume Volume 3: Cycle Innovations; Education; Electric Power; Fans and Blowers; Industrial and Cogeneration of *Turbo Expo: Power for Land, Sea, and Air*, 06 2012.

[7] D.G. Wilson and N.R. Dunteman. The inverted brayton cycle for waste-heat utilization. *ASME*, 1973.

[8] Costante Mario Invernizzi. *Closed Power Cycles Thermodynamic Fundamentals and Applications*. 2013.

[9] Ahmed Laouir. Performance analysis of open-loop cycles for lh2 regasification. *international journal of hydrogen energy*, 44(22425 - 22436), 2018.

[10] R. K. Shah and D.P. Sekulic. *Fundamentals of Heat Exchanger Design*. 2003.

[11] Alfa Laval. How gasketed plate heat exchangers work. https://www.alfalaval.se/microsites/packningsforsedda-plattvarmevaxlare/verktyg/hur-packningsforsedda-plattvarmevaxlare-fungerar/, 2016. Online; accessed on (30-05-2022).

[12] W. M. Kays and A. L. London. *Compact Heat Exchangers*. Medtech, 2018.

[13] Marco Tridente. Cfd study on the effect of a transonic fan downstream of an s-shape duct. mathesis, UNIVERSITÍ A DEGLI STUDI DI PADOVA, 2019.

[14] I.E. Idelchik. *Handbook of Hydraulic Resistance*. New York: Begell House, 1996.

[15] GasTurb team. *GasTurb 14*. GasTurb GmbH, 2024.

[16] Nicholas C . Kailos. Increased helicopter capability through advancedpowerplant technology. *Journal of the American Helicopter Society*, 1967.

[17] Carozza A. *Heat Exchangers in the Aviation Engineering. Heat Exchangers - Advanced Features and Applications*. intechOpen, 2017.

[18] R.K. Pachauri Core Writing Team and L.A. Meyer (eds.). Ipcc, 2014: Climate change 2014: Synthesis report. contribution of working groups i, ii and iii to the fifth assessment report of the intergovernmental panel on climate change. Technical report, IPCC, 2014.

[19] M Klöwer, M R Allen, D S Lee, S R Proud, L Gallagher, and A Skowron. Quantifying aviation's contribution to global warming. *Environmental Research Letters*, 16(10):104027, nov 2021.

[20] IATA. Global outlook for air transport, deep change. Technical report, International Air Transport Association, 2024.

[21] Regulation (eu) 2021/1119 of the european parliament and of the council of 30 june 2021 establishing the framework for achieving climate neutrality and amending regulations (ec) no 401/2009 and (eu) 2018/1999 ('european climate law'). *OJ*, L 243/1:7, 2021.

[22] J. Benad. The flying v a new aircraft configuration for commercial passenger transport. In *Deutsche Gesellschaft für Luft- und Raumfahrt - Lilienthal-Oberth e.V., Bonn, 2015*, 2015.

[23] Appu>porject>objectives. https://www.tudelft.nl/lr/appu/project/objectives. Accessed: 01-09-2024.

[24] B. Mattson, T. Hoette, and M. S. Applebee. Incomplete combustion of hydrogen: Trapping a reaction intermediate. *Journal of Chemical Education*, 84(1668), 2007.

[25] D. Verstraete. On the energy efficiency of hydrogen-fuelled transport aircraft. *International Journal of Hydrogen Energy*, 40(23):7388–7394, 2015.

[26] Ozgur Balli, Yasin Sohret, and Hikmet T. Karakoc. The effects of hydrogen fuel usage on the exergetic performance of a turbojet engine. *International Journal of Hydrogen Energy*, 43(23):10848–10858, 2018. The 2nd International Hydrogen Technologies Congress (IHTEC-2017).

[27] Brayton George B. Improvement in gas engines, 1872.

[28] D. Di Battista, F. Fatigati, R. Carapellucci, and R. Cipollone. Inverted brayton cycle for waste heat recovery in reciprocating internal combustion engines. *Applied Energy*, 253(113565), 2019.

[29] Noémie Chagnon-Lessard, Colin Copeland, François Mathieu-Potvin, and Louis Gosselin. Maximizing specific

work output extracted from engine exhaust with novel inverted brayton cycles over a large range of operating conditions. *Energy*, 191:116350, 2020.
[30] M. Bianchi and A. De Pascale. Bottoming cycles for electric energy generation: Parametric investigation of available and innovative solutions for the exploitation of low and medium temperature heat sources. *Applied Energy*, 88(5):1500–1509, 2011.
[31] Rui F. Costa and Brendan D. MacDonald. Comparison of the net work output between stirling and ericsson cycles. *Energies*, 11(670), 2018.
[32] T. S. Kyung and C. Kim. *LNG Cold Energy Utilization Technology*. 2016.
[33] Kuppan Thulukkanam. *Heat Exchanger Design Handbook*. CRC Press, second edition, 2013.
[34] David Reay. *Learning from experiences with compact heat exchangers*. Centre for the Analysis and Dissemination of Demonstrated Energy Technologies CADDET, Sittard (Netherlands), 1999.
[35] Jr. Malcolm W. Chase. Nist-janaf thermochemical tables, 1998.
[36] T.L. Bergman and A. Lavine. *Fundamentals of Heat and Mass Transfer*. Wiley, 2011.
[37] Volker Gnielinski. New equations for heat and mass transfer in turbulent pipe and channel flow. *Int. Chem. Eng. 16*, 1976.
[38] Petukhov. *Advances in Heat Transfer*. Academic Press, New York, 1970.
[39] Roger Legg. *Air Conditioning System Design*. Elsevier Ltd., 2017.
[40] Saeed Farokhi. *Aircraft Propulsion*. Wiley, 2014.
[41] Alexandre Capitao Patrao, Isak Jonsson, Carlos Xisto, Anders Lundbladh, and Tomas Grönstedt. Compact heat exchangers for hydrogen-fueled aero engine intercooling and recuperation. *Applied Thermal Engineering*, 243:122538, 2024.
[42] Material properties database. https://www.makeitfrom.com/, 2009-2021. Online database; accessed on (04-02-2022).
[43] Joshua D. Brooks and Dimitri N. Mavris. Compact heat exchanger sizing and mass estimation. In *AIAA Propulsion and Energy Forum*, Atlanta, GA, 30332, United States, 2021. Georgia Institute of Technology.
[44] Dassault Systèmes. *Dymola User Manual*.
[45] Joachim Kurzke. *GasTurb 12*, 2012.
[46] Linda Petzold. A description of dassl: A differential/algebraic system solver. page 5, 01 1982.
[47] David Mayers Endre Süli. *An Introduction to Numerical Analysis*. Cambridge University Press, 2003.
[48] Francesco Casella. External media package. https://github.com/modelica-3rdparty/ExternalMedia, 2006-2024.
[49] Alexander Heidebrecht, Martijn van Sluis, Daamanjyot Barara, Sarah Link, Gioele Ferrante, Kaushal Dave, Tomas Sinnige, Francesca De Domenico, Ivan Langella, Georg Eitelberg, and Arvind Gangoli Rao. Auxiliary power and propulsion unit outcomes of the appu research project. Technical report, Delft University of Technology, 2024.
[50] Daniel P. Raymer. *Aircraft Design: A Conceptual Approach*. AIAA, 1992.
[51] David F. Rogers. *Technical Flying*. NAR associates, 1994.
[52] Ronald D. Flack. *Fundamentals of Jet Propulsion with Applications*. CAMBRIDGE UNIVERSITY PRESS, 40 West 20th Street, New York, NY 100 114211, USA, 2005.
[53] TAKEHIRO OKURA. Materials for aircraft engines, 2015.
[54] Giridhar Gudivada and Ajoy Kumar Pandey. Recent developments in nickel-based superalloys for gas turbine applications: Review. *Journal of Alloys and Compounds*, 963:171128, 2023.
[55] Maria Jonsson, Olav Bolland, Dominikus Bücker, and Mike Rost. Gas turbine cooling model for evaluation of novel cycles. 01 2005.
[56] Feijia Yin, Floris S. Tiemstra, and Arvind Gangoli Rao. Development of a flexible turbine cooling prediction tool for preliminary design of gas turbines. *Journal of Engineering for Gas Turbines and Power*, 140(9):091201–1 – 091201–12, 2018.
[57] Ian H. Bell, Jorrit Wronski, Sylvain Quoilin, and Vincent Lemort. Pure and pseudo-pure fluid thermophysical property evaluation and the open-source thermophysical property library coolprop. *Industrial & Engineering Chemistry Research*, 53(6):2498–2508, 2014.
[58] Fakhre Ali, Ioannis Goulos, Vassilios Pachidis, Mahmood Tashfeen, and Pericles Pilidis. Helicopter mission analysis for a regenerated turboshaft. School of Engineering, Department of Power and Propulsion, Cranfield University, June 2013.
[59] Mohtasim Syed, Fakhre Ali, Ioannis Goulos, and Vassilios Pachidis. A preliminary parametric study for an advanced propulsion technology helicopter. 2014.
[60] Arvind Gangoli Rao and Feija Yin. The appu engine preliminary design july 2021. Presentation.
[61] Yasin Şöhret, Önder Turan, and T. Karakoc. Analysis of combustion efficiency for turbofan engine combustor using matlab. *International Journal of Engineering and Technology*, 7:86–90, 05 2015.
[62] Echemi. https://www.echemi.com/pip/kerosene-pid_Rock27024.html. Accessed: 01-12-2024.
[63] Martin van Schie. Steam injection and recovery in the appu. Master's thesis, Delft University of Technology, 2024.